SEISMIC BEHAVIOR OF STEEL I-BEAMS REINFORCED WITH GLASS FIBER REINFORCED POLYMER: AN EXPERIMENTAL STUDY

A Thesis Submitted to
The Graduate School of Engineering and Sciences of
Izmir Institute of Technology
in Partial Fulfillment of the Requirements for the Degree of

MASTER OF SCIENCE

in Civil Engineering

by
Doruk YORMAZ

July 2010

İZMİR

We approve the thesis of **Doruk YORMAZ**

Assist. Prof. Dr. O. Özgür EĞİLMEZ
Supervisor

Assist. Prof. Dr. Cemalettin DÖNMEZ
Committee Member

Prof. Dr. Metin TANOĞLU
Committee Member

13 July 2010

Prof. Dr. Gökmen TAYFUR
Head of the Department of Civil Engineering

Assoc. Prof. Dr. Talat YALÇIN
Dean of the Graduate School of
Engineering and Sciences

ACKNOWLEDGEMENTS

This research study was conducted at the Structural Mechanics Laboratory in the Izmir Institute of Technology and was funded by The Scientific and Research Council of Turkey (TÜBİTAK) and European Union. I would like to thank these organizations for their supports.

I would like to express the deepest appreciation to my advisor, Assist. Prof. Dr. O. Özgür EĞİLMEZ for all of his guidance, advice, understanding and support. Special thanks to him for giving me the opportunity working in this research project.

I wish to thank my advisory committee; Assist. Prof. Dr. Cemalettin DÖNMEZ and Prof. Dr. Metin TANOĞLU for sharing their technical knowledge and contributions to my thesis.

I also wish to thank my colleagues; Başak DOĞAN, Can Ali Güven, Cemal KILIÇ, Hakan GÖKDAĞ, Mehmet Alper ÇANKAYA and Timur ÖZDEMİR for their good friendship and supports during the experimental stage.

Lastly, I would like to express my great gratitude to my family for all of their love, support and encouragement over the years.

ABSTRACT

SEISMIC BEHAVIOR OF STEEL I-BEAMS REINFORCED WITH GLASS FIBER REINFORCED POLYMER: AN EXPERIMENTAL STUDY

Design guidelines, which are put into effect in the aftermath of the 1994 Northridge earthquake, require intermediate and special moment frames (IMF and SMF) be capable of maintaining 0.02 and 0.04 radians interstory drift, respectively without significant strength degradation and development of instability. However, local buckles in the plastic hinge region are major hindrances for the ductility capability and stability of the structural system. Thus, the research program aims to mitigate such inelastic instabilities by using glass fiber reinforced polymer (GFRP), which possesses elastic modulus roughly one order of magnitude less than that of steel. On the other hand, this elastic modulus discrepancy between GFRP and steel can be useful for stabilizing local buckles by means of the bracing effect of GFRP during plastic hinge formations. This thesis describes large-scale experimental study of the research program that investigates the seismic behavior of steel I-beams reinforced with GFRP. In this experimental study, four HE400AA beams with welded haunch (WH) modification and three HE500AA beams with no modification were tested under cyclic loading. The results of experimental study indicate that it does not seem possible to rely on GFRP reinforcement to increase the flexural resistance of connections at a rotation of 0.04 radians because the adhesive layer between steel and GFRP fails in rotations much lower than 0.04 radians. However, the seismic performance of the structure can be moderately improved with the bottom flange WH and GFRP reinforcement in order to maintain rotations without local buckles in accordance with the rotation demand of IMFs, which is 0.02 radians.

ÖZET

POLİMERLE GÜÇLENDİRİLMİŞ CAM ELYAF İLE DESTEKLENMİŞ ÇELİK I-KİRİŞLERİNİN SİSMİK DAVRANIŞI: DENEYSEL ÇALIŞMA

1994 Northridge depremi sonrası tasarım yönetmelikleri dayanım kaybı ve stabilite azalması olmaksızın süneklik düzeyi normal ve yüksek çerçeveler için sırasıyla 0.02 ve 0.04 radyan göreli kat ötelemesi sağlayabilme şartını koşmaktadır. Ancak, plastik mafsal bölgesinde oluşan yerel burkulmalar yapısal sistemin süneklik ve stabilitesi açısından sorun teşkil etmektedir. Bu nedenle araştırma programında, çeliğe kıyasla onda biri kadar elastisite modülüne sahip polimerle güçlendirilmiş cam elyaf (PGCE) malzemeler kullanarak bu plastik kararsızlıkların azaltılması amaçlanmıştır. Öte yandan, PGCE ile çelik arasında olan bu elastisite modülü farklılığı plastik mafsal oluşumundaki yerel burkulmaların önlenmesi uygulamalarında önemli bir değer oluşturmaktadır. Bu tez, PGCE ile desteklenmiş çelik I-kirişlerinin sismik davranışı araştırmasının deneysel kısmını oluşturmaktadır. Bu deneysel çalışmada, dört adet kaynaklı kemer takviyeli HE400AA kirişi ve üç adet de takviyesiz HE500AA kirişi test edilmiştir. Deneysel çalışmanın sonuçlarına göre, çelik ve PGCE arasındaki yapışma, 0.04 radyanlık dönmeden çok daha az olan dönmelerde çözülmüş olacağından 0.04 radyanlık dönmede birleşimlerin eğilme direncini arttırmak için PGCE güçlendirmesine güvenmek mümkün değildir. Ancak, eğer alt başlığa kaynaklanmış kemerli takviye iyileştirmesi yapının sismik performansını orta derecede arttırmak amacıyla uygulanmışsa, PGCE takviyesi birleşimlerin süneklik düzeyi normal çerçeveler için gerekli olan 0.02 radyanlık dönme değerlerine herhangi bir yerel burkulma gerçekleşmeden ulaşabilmelerine yardımcı olabilmektedir.

TABLE OF CONTENTS

LIST OF FIGURES ix

LIST OF TABLES xii

CHAPTER 1. INTRODUCTION 1
1.1. General 1
1.2. Objectives 3
1.3. Overall Research Program 4
1.4. Thesis Organization 5

CHAPTER 2. LITERATURE REVIEW 6
2.1. Introduction 6
2.2. Rehabilitation Techniques of Steel Moment Resisting Frames 6
2.2.1. Welded Haunch (WH) Literature 8
2.3. Fiber Reinforced Polymer (FRP) Literature 9
2.3.1. FRP Materials 9
2.3.2. FRP-Steel Applications 11
2.3.2.1. Flexural Strengthening Applications 11
2.3.2.2. Fatigue Repair Applications 14
2.3.2.3. Enhancing Stability Applications 14

CHAPTER 3. EXPERIMENTAL STUDY 18
3.1. Introduction 18
3.2. Loading System 18
3.3. Test Beams 19
3.3.1. Tensile Coupon Standard Tests 19
3.3.2. Properties of the Sections 20
3.4. Test Setup 23
3.5. Loading Protocol 27
3.5.1. Relationship between Test Setup and Loading Protocol 28

3.6. Instrumentation 28
3.6.1. Linear Variable Differential Transducers (LVDT) 29
3.6.2. Strain Gages 29
3.6.3. Data Acquisition 33
3.7. GFRP Applications 34
3.7.1. Glass Fiber Reinforced Polymer 34
3.7.2. Surface Preparation 37
3.7.3. GFRP Application Process 37
3.7.4. GFRP Applications for the HE400AA Beams 39
3.7.5. GFRP Applications for the HE500AA Beams 43

CHAPTER 4. EXPERIMENTAL RESULTS 46
4.1. Test Observations 46
4.1.1. HE400AA Bare Beam 46
4.1.2. HE400AA GFRP1 Beam 49
4.1.3. HE400AA GFRP2 Beam 52
4.1.4. HE400AA GFRP3 Beam 56
4.1.5. HE500AA Bare Beam 59
4.1.6. HE500AA GFRP1 Beam 63
4.1.7. HE500AA GFRP2 Beam 67
4.2. Cyclic Behavior of Test Beams 71
4.2.1. Total Beam Rotations 71
4.2.1.1. HE400AA Beams 72
4.2.1.2. HE500AA Beams 75
4.2.2. Beam Strain Gage Data 78
4.2.2.1. HE400AA Beams 78
4.2.2.2. HE500AA Beams 83

CHAPTER 5. PERFORMANCE COMPARISONS 88
5.1. Comparisons of HE400AA Beams 88
5.1.1. HE400AA Bare Beam versus HE400AA GFRP1 Beam 88
5.1.2. HE400AA Bare Beam versus HE400AA GFRP2 Beam 89
5.1.3. HE400AA Bare Beam versus HE400AA GFRP3 Beam 90

5.1.4. HE400AA GFRP1 Beam versus HE400AA GFRP2 Beam 91
5.1.5. HE400AA GFRP1 Beam versus HE400AA GFRP3 Beam 92
5.1.6. HE400AA GFRP2 Beam versus HE400AA GFRP3 Beam 93
5.1.7. Local Flange Buckling Comparison of HE400AA Beams 94
5.2. Comparison of HE500AA Beams 96
5.2.1. HE500AA Bare Beam versus HE500AA GFRP1 Beam 96
5.2.2. HE500AA Bare Beam versus HE500AA GFRP2 Beam 97
5.2.3. HE500AA GFRP1 Beam versus HE500AA GFRP2 Beam 98
5.2.4. Local Flange Buckling Comparison of HE500AA Beams 99

CHAPTER 6. CONCLUSIONS 102
6.1. Introduction 102
6.2. Experimental Study 102
6.3. Conclusions 103
6.4. Recommendations 105

REFERENCES 107

APPENDICES
APPENDIX A. BEAM-COLUMN CONNECTION DESIGN 112
APPENDIX B. WELDED HAUNCH DESIGN 131

LIST OF FIGURES

Figure **Page**

Figure 1.1. Typical Failure on Pre-Northridge Beam-Column Connection 2
Figure 1.2. The Hybrid System of Beam-Composite Material 4
Figure 2.1. Modification Methods 7
Figure 2.2. Details of Welded Haunch Connection 9
Figure 2.3. Tensile Stress and Strain Diagram of Fibers 10
Figure 3.1. Interstory Drift Angle 22
Figure 3.2. Plan View of Reaction Wall 24
Figure 3.3. Section A-A of Reaction Wall 25
Figure 3.4. Section B-B of Reaction Wall 25
Figure 3.5. Test Beam and Test Setup 26
Figure 3.6. Photograph of Test Setup 27
Figure 3.7. Loading Protocol (AISC 2005b) 28
Figure 3.8. Locations of LVDTs 29
Figure 3.9. HE400AA Beam Steel Strain Gauges Layout 31
Figure 3.10. HE400AA Beams Composite Strain Gauges Layout 32
Figure 3.11. HE500AA Beam Steel Strain Gauges Layout 32
Figure 3.12. HE500AA Beams Composite Strain Gauges Layout 33
Figure 3.13. Data Acquisition Instruments 34
Figure 3.14. Direct Wet Lay-up Application 38
Figure 3.15. Clapping GFRP with Wood Plates 38
Figure 3.16. GFRP Layout of HE400AA GFRP1 Beam 40
Figure 3.17. HE400AA GFRP1 Beam 40
Figure 3.18. GFRP Layout of HE400AA GFRP2 Beam 41
Figure 3.19. HE400AA GFRP2 Beam 41
Figure 3.20. GFRP Layout of HE400AA GFRP3 Beam 42
Figure 3.21. HE400AA GFRP3 Beam 42
Figure 3.22. GFRP Layout of HE500AA GFRP1 Beam 43
Figure 3.23. HE500AA GFRP1 Beam 44
Figure 3.24. GFRP Layout of HE500AA GFRP2 Beam 44

Figure 3.25. HE500AA GFRP2 Beam..... 45
Figure 4.1. HE400AA Bare Beam Loading Protocol 47
Figure 4.2. HE400AA Bare Beam Load versus Beam Rotation at WH Tip 47
Figure 4.3. HE400AA Bare Beam Top Flange at 0.034 rad of Rotation..... 48
Figure 4.4. HE400AA Bare Beam Bottom Flange at 0.034 rad of Rotation 48
Figure 4.5. HE400AA GFRP1 Beam Loading Protocol..... 50
Figure 4.6. HE400AA GFRP1 Beam Load versus Beam Rotation at WH Tip 50
Figure 4.7. HE400AA GFRP1 Beam Top Flange at 0.033 rad of Rotation 51
Figure 4.8. HE400AA GFRP1 Beam Bottom Flange at 0.028 rad of Rotation..... 51
Figure 4.9. HE400AA GFRP1 Beam Top Flange at 0.044 rad of Rotation 52
Figure 4.10. HE400AA GFRP2 Beam Loading Protocol..... 53
Figure 4.11. HE400AA GFRP2 Beam Load versus Beam Rotation at WH Tip 54
Figure 4.12. HE400AA GFRP2 Beam Top Flange at 0.034 rad of Rotation 54
Figure 4.13. HE400AA GFRP2 Beam Bottom Flange at 0.034 rad of Rotation..... 55
Figure 4.14. HE400AA GFRP2 Beam Top Flange Fracture at 0.046 rad of Rotation55
Figure 4.15. HE400AA GFRP3 Beam Loading Protocol..... 57
Figure 4.16. HE400AA GFRP3 Beam Load versus Beam Rotation at WH Tip 57
Figure 4.17. HE400AA GFRP3 Beam Top Flange at 0.033 rad of Rotation 58
Figure 4.18. HE400AA GFRP3 Beam Top Flange at 0.043 rad of Rotation 58
Figure 4.19. HE400AA GFRP3 Beam Bottom Flange at 0.043 rad of Rotation..... 59
Figure 4.20. HE500AA Bare Beam Loading Protocol 60
Figure 4.21. HE500AA Bare Beam Load versus Beam Fixed-End Rotation..... 61
Figure 4.22. HE500AA Bare Beam Bottom Flange at 0.017 rad of Rotation 61
Figure 4.23. HE500AA Bare Beam Top Flange at 0.033 rad of Rotation..... 62
Figure 4.24. HE500AA Bare Beam Top Flange at 0.042 rad of Rotation..... 62
Figure 4.25. HE500AA Bare Beam Bottom Flange at 0.042 rad of Rotation 63
Figure 4.26. HE500AA GFRP1 Beam Loading Protocol..... 64
Figure 4.27. HE500AA GFRP1 Beam Load versus Beam Fixed-End Rotation 65
Figure 4.28. HE500AA GFRP1 Beam Top Flange at 0.033 rad of Rotation 65
Figure 4.29. HE500AA GFRP1 Beam GFRP Debonding at 0.036 rad of Rotation... 66
Figure 4.30. HE500AA GFRP1 Beam Top Flange at 0.043 rad of Rotation 66
Figure 4.31. HE500AA GFRP1 Beam Bottom Flange at 0.045 rad of Rotation..... 67
Figure 4.32. HE500AA GFRP2 Beam Loading Protocol..... 68

Figure 4.33. HE500AA GFRP2 Beam Load versus Beam Fixed-End Rotation 69
Figure 4.34. HE500AA GFRP2 Beam Bottom Flange at 0.023 rad of Rotation..... 69
Figure 4.35. HE500AA GFRP2 Beam Top Flange at 0.034 rad of Rotation 70
Figure 4.36. HE500AA GFRP2 Beam Top Flange at 0.044 rad of Rotation 70
Figure 4.37. HE500AA GFRP2 Beam Bottom Flange at 0.044 rad of Rotation..... 71
Figure 4.38. HE400AA Bare Beam Rotation at WH Tip vs. M/M_p 72
Figure 4.39. HE400AA GFRP1 Beam Rotation at WH Tip vs. M/M_p..... 73
Figure 4.40. HE400AA GFRP2 Beam Rotation at WH Tip vs. M/M_p..... 74
Figure 4.41. HE400AA GFRP3 Beam Rotation at WH Tip vs. M/M_p..... 75
Figure 4.42. HE500AA Bare Beam Fixed-End Rotation vs. M/M_p 76
Figure 4.43. HE500AA GFRP1 Beam Fixed-End Rotation vs. M/M_p..... 77
Figure 4.44. HE500AA GFRP2 Beam Fixed-End Rotation vs. M/M_p..... 78
Figure 4.45. HE400AA Bare Beam Top Flange Width Strain Distribution..... 80
Figure 4.46. HE400AA Bare Beam Top Flange Longitudinal Strain Distribution 81
Figure 4.47. HE400AA Bare Beam Bottom Flange Longitudinal Strain Distribution82
Figure 4.48. HE400AA GFRP3 Beam SG-C403 Reading 83
Figure 4.49. HE500AA Bare Beam Top Flange Width Strain Distribution..... 85
Figure 4.50. HE500AA Bare Beam Bottom Flange Width Strain Distribution 86
Figure 4.51. HE500AA GFRP3 Beam SG-C402 Reading 87
Figure 5.1. HE400AA Bare Beam vs. HE400AA GFRP1 Beam 89
Figure 5.2. HE400AA Bare Beam vs. HE400AA GFRP2 Beam 90
Figure 5.3. HE400AA Bare Beam vs. HE400AA GFRP3 Beam 91
Figure 5.4. HE400AA GFRP1 Beam vs. HE400AA GFRP2 Beam..... 92
Figure 5.5. HE400AA GFRP1 Beam vs. HE400AA GFRP3 Beam..... 93
Figure 5.6. HE400AA GFRP2 Beam vs. HE400AA GFRP3 Beam..... 94
Figure 5.7. HE400AA Beams Top Flange Local Buckling Comparison 95
Figure 5.8. HE400AA Beams Bottom Flange Local Buckling Comparison..... 95
Figure 5.9. HE500AA Bare Beam vs. HE500AA GFRP1 Beam 97
Figure 5.10. HE500AA Bare Beam vs. HE500AA GFRP2 Beam 98
Figure 5.11. HE400AA GFRP1 Beam vs. HE400AA GFRP3 Beam..... 99
Figure 5.12. HE500AA Beams Top Flange Local Buckling Comparison 100
Figure 5.13. HE500AA Beams Bottom Flange Local Buckling Comparison..... 100

LIST OF TABLES

Table **Page**

Table 2.1. Typical Properties of Steel-FRP Systems 11
Table 3.1. Standard Tensile Coupon Test Results 19
Table 3.2. Nominal Dimensions and Properties of Sections 20
Table 3.3. Actual Dimensions and Properties of Sections 20
Table 3.4. Physical Properties of Duratek Epoxy 35
Table 3.5. Mechanical Properties of Duratek Epoxy 36
Table 3.6. Mechanical Properties of GFRP used in Experiments 36
Table 6.1. HE400AA and HE500AA Beams GFRP Applications 105

CHAPTER 1

INTRODUCTION

1.1. General

Steel moment resisting frames (SMRF) are designed to resist lateral forces such as earthquake and wind with sufficient ductility capability in order to dissipate energy by means of inelastic deformations, which are expected particularly in the beams as plastic hinges. However, in the aftermath of the 1994 Northridge and 1995 Kobe earthquakes, the damages (primarily bottom flange brittle fractures) revealed the deficiencies on this typical connection design (see Figure 1.1) and a large variety of research were conducted in order to overcome brittle weld fractures and enhance plastic rotation capacity of welded connections. As a result of these investigations, the seismic design of steel moment frame connections has been significantly changed. Pre-Northridge SMRFs details have been removed from the Uniform Building Code (UBC 1994) and new design guidelines (AISC 2003a, FEMA 2000a, FEMA 2000b) have been proposed for new construction and modifications in existing structures, including welded haunch (WH) and reduced beam sections (RBS) connections that require intermediate and special moment frames (IMF and SMF) be capable of maintaining 0.02 and 0.04 radians inter-story drift, respectively without significant strength degradation and development of instability. On the other hand, flange local buckling (FLB) and web local buckling (WLB) are still major hindrances for the ductility and stability of the structural system, in the course of the plastic rotations, which are in the order of 0.03 to 0.035 radians while lateral torsional buckling (LTB) is generally eliminated by limiting the unbraced length of the beams. Thus, mitigation of such inelastic instabilities in steel members is an important task in order to provide dependable ductility and energy dissipation capacity in the structures subjected to large plastic rotations under major earthquakes and rehabilitation is a must particularly for existing steel moment frames to achieve plastic moment capacity without significant strength degradation and development of instability. Furthermore,

the repair works of local buckles are relatively costly and time-consuming, which emphasize the significance of ductility and stability of steel members in nature.

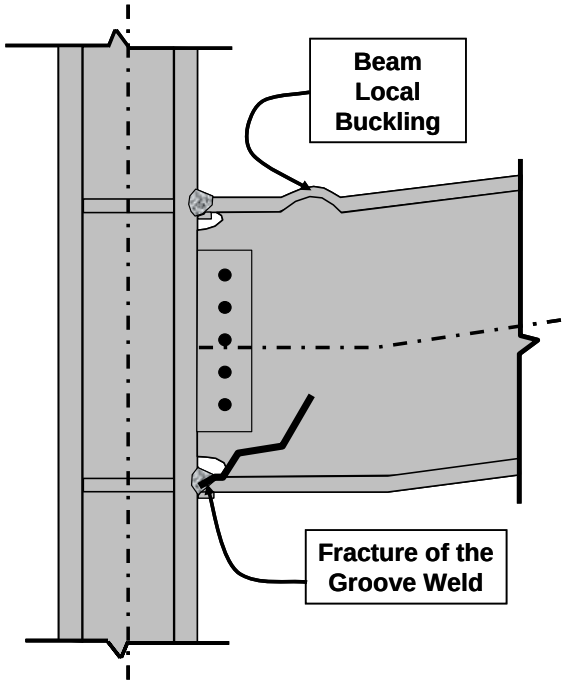

Figure 1.1. Typical Failure on Pre-Northridge Beam-Column Connection
(Source: FEMA 2000b)

The use of fiber reinforced polymers (FRP) has gained significant importance in strengthening and repair applications of steel members and a great deal of research has been conducted. These investigations particularly focused on the strengthening flexural resistance of the members, repairing fractures and enhancing fatigue performance (Sen, et al. 2001, Tavakkolizadeh and Saadatmanesh 2003a, Jones and Civjan 2003, El Damatty, et al. 2005, Lenwari 2005, Photiou, et al. 2006). Stabilizing local instabilities through use of FRP materials has also attracted attention in recent years (Ekiz, et al. 2004, Accord and Earls 2006, Harries, et al. 2009). FRP materials were commonly used in the abovementioned applications in lieu of traditional rehabilitation procedures due to their many of advantages including application ease, lower costs and lighter dead weight, reduced stress concentrations, high fatigue strength, resistance to corrosion and aesthetic concerns. Carbon fiber reinforced polymer (CFRP) materials are generally utilized in repair and strengthening

applications of steel structural systems. They meet the rehabilitation requirements with their high strength, high modulus and ultra-high modulus alternatives. On the contrary of CFRP, glass fiber reinforced polymer (GFRP) materials have much lower elastic modulus than that of steel and therefore they are not preferred in rehabilitation applications even though they are much more cost-effective.

1.2. Objectives

GFRP materials possess elastic modulus that is roughly one order of magnitude less than that of steel. However, this elastic modulus discrepancy between GFRP and steel can be useful for stabilizing local flange and web buckles by means of the bracing effect of GFRP during plastic hinge formations with the least possible strength increase in the section. A strength increase in the beam section is not desired in the SMRF beam-column connections because higher forces in the beam-column welds can occur and may result in weld fractures. On the other hand, GFRP materials have less stress levels than steel due to their low modulus under loading and this difference enable GFRP strips to maintain their flexural strength to provide bracing effect for the underlying steel section, which has plastic deformations.

The objective of this research program is to investigate the behavior of steel-GFRP systems under cyclic loading. Through this study, it is aimed to obtain ductility enhancement on the present steel moment resisting frames (SMRF) with the application of GFRP on the beam plastic hinge regions by means of preventing or postponing flange and web local buckles. Figure 1.2 demonstrates steel beam composite material hybrid system configuration in which GFRP is placed on both top and bottom flanges in the plastic hinge region.

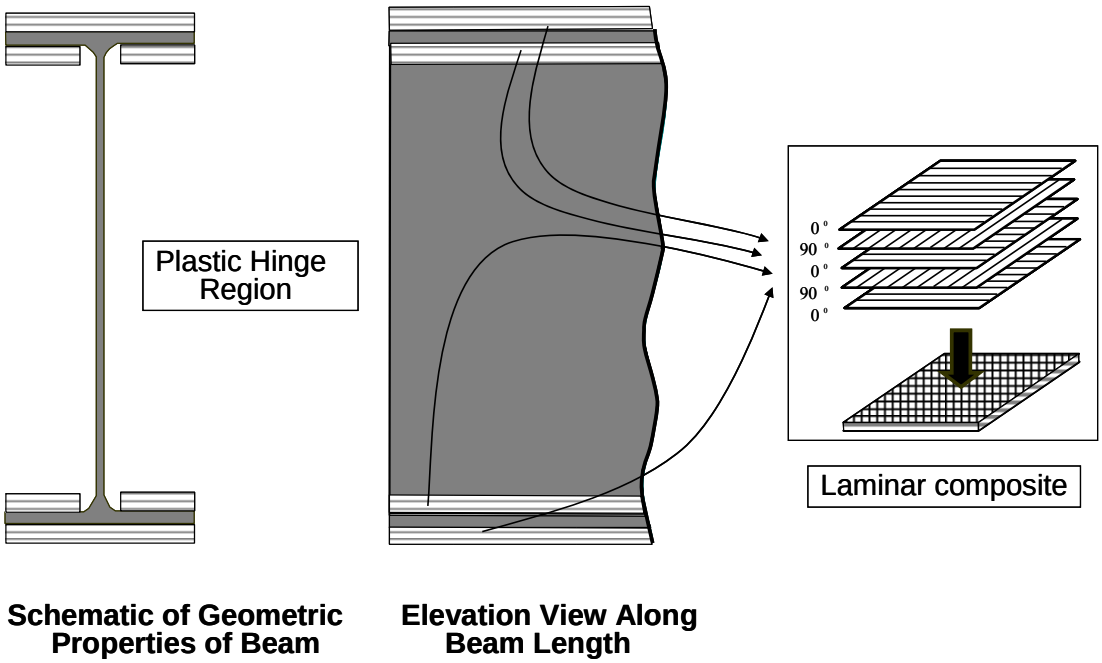

Figure 1.2. The Hybrid System of Beam-Composite Material

1.3. Overall Research Program

The research program was conducted in Izmir Institute of Technology in three phases, which consisted of finite element analytical (FEA) studies, small-scale standard tests and large-scale steel beam experiments. In the first phase, FEA studies were conducted on steel I-sections with welded triangular haunch and reduced beam section modification. Beams with and without GFRP reinforcement were analyzed in order to get comparisons between each other. The effect of GFRP thickness, width and length was studied on preventing or postponing local buckles under cyclic loading and interfacial and interlaminar shear stresses were examined depending upon flexural resistance of the beams at column face. Finite element studies were conducted by Alkan (2008) and Ozdemir (2009). Parallel to FEA studies small-scale standard tests were also conducted in order to determine the mechanical properties of GFRP and other substrates as the second phase of the research program. The interfacial shear strength between steel and GFRP and the interlaminar shear strength between GFRP layers were determined according to the various epoxy and surface primer configurations and the most suitable application in the large-scale steel

experiments was decided upon these mechanical test results. The detailed information about the mechanical tests can be found in Guven's (2009) M.Sc. thesis. As for the last phase, the large-scale steel tests were conducted under cyclic loading in two parts: HE400AA beams and HE500AA beams. HE400AA beam sections were tested with triangular WH modification with and without GFRP while HE500AA beam sections were tested with no modification with and without GFRP. RBS improvement had been planned for the HE500AA beams experiments; however, it was decided to test HE500AA beams with no modification after the FEA results, which demonstrated that RBS improvement was not successful for GFRP reinforced sections. This thesis includes results from the large-scale HE beam shallow sections.

1.4. Thesis Organization

The literature review on welded haunch experiments in the aftermath of the Northridge earthquake, fiber reinforced polymer (FRP) materials and FRP-steel applications are presented in Chapter 2. Literature on FRP-steel applications is divided into three parts: flexural strengthening, fatigue repair and enhancing stability, respectively, and is also discussed in Chapter 2.

Chapter 3 presents a brief description of the experimental study including test specimens, test setup, properties of the sections and instrumentation procedures. GFRP applications with surface preparation and application process are described in the detailed way in this chapter as well.

Cantilever beam experiment results are presented in Chapter 4. This chapter begins with the test observations and presents detailed descriptions about specimen behaviors under cyclic loading.

Chapter 5 presents performance comparisons of test specimens and evaluations about cyclic behavior of the sections.

Finally, the conclusions and recommendations for future studies take place in Chapter 6.

CHAPTER 2

LITERATURE REVIEW

2.1. Introduction

On the contrary of heavy steel plates in conventional repairing methods, fiber reinforced polymers (FRP) are lightweight and non-corrosive materials. They also have high strength-to-weight ratios as well as cost effective performances in long-term repairing applications. For these reasons, FRP composites have gained considerable amount of importance on strengthening and repair applications for steel structures in the past decade (Schnerch, et al. 2006, Photiou, et al. 2006, Tavakkolizadeh and Saadatmanesh 2003a). Many researchers have conducted analytical and experimental investigations especially using carbon fiber reinforced polymers (CFRP) for strengthening applications of steel structures on the account of the fact that CFRP materials have similar even greater elastic modulus than that of steel.

In recent years, in addition of strengthening applications, many research have been conducted aiming at enhancing the plastic rotation capacity of steel members utilizing glass fiber reinforced polymers (GFRP) with elastic modulus one order of magnitude less than steel. However, the use of GFRP composites in developing seismic performance of beam-column connections has not yet been studied as retrofitting method for existing steel moment resisting frames (SMRF). This chapter will first present information on rehabilitation techniques of SMRFs and literature reviews about steel-FRP materials applications.

2.2. Rehabilitation Techniques of Steel Moment Resisting Frames

The 1994 Northridge and 1995 Kobe earthquakes has become a milestone for the beam-column connections in the steel moment resisting frames (SMRF). In the aftermath of these events, widespread occurrences of the connection failures in

SMRFs have demonstrated that these typical Pre-Northridge beam-column connections have significant strength and ductility deficiencies. Through the comprehensive research projects by National Institute of Standards and Technology (NIST), the American Institute of Steel Construction (AISC), the Federal Emergency Management Agency (FEMA), the University of California at San Diego, the University of Texas at Austin, and Lehigh University (SAC 1996) experimental, analytical and numerical studies have been performed to provide adequate seismic performance of the Pre-Northridge beam-column connections in SMRFs. As a consequence of these investigations, new design guidelines have been proposed for new constructions and modification methods have been developed for existing steel moment frames aiming at improvements on overall seismic performance including strength, stiffness, ductility and plastic rotation capacities of the connections (FEMA 2000a, FEMA 2000b, AISC 2005a).

New design guidelines consist of a wide variety of new beam-column connections for SMRFs so that inelastic deformations are expected in the beams through the formation of plastic hinges away from the face of the column. Thus, possible brittle weld fractures near the edge of the beam flange to column groove weld have been desired to be eliminated forcing the plastic hinges outside this region. A lot of variety of reinforced connections including strengthening and weakening the beams have been proposed for the design strategies: Welded Haunch (WH), Reduced Beam Section (RBS), and Bolted Bracket (BB) modifications (AISC 2003a).

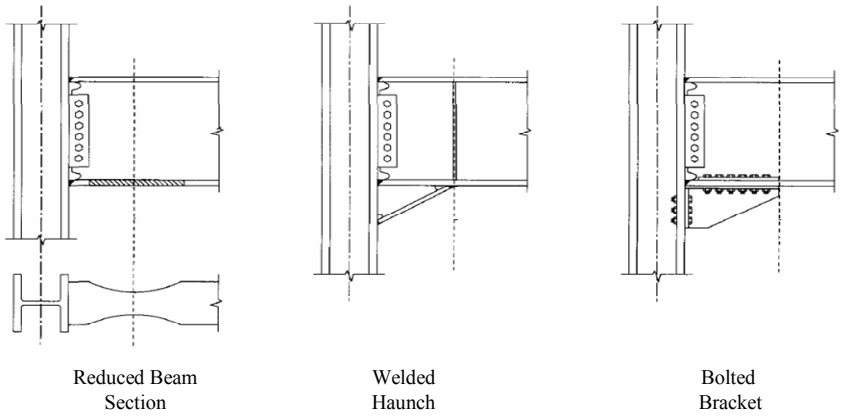

Figure 2.1. Modification Methods
(Source: AISC 2003a)

2.2.1. Welded Haunch (WH) Literature

Welded haunch (WH) modification method aims to strengthen the steel beam near the welded connection by welding a triangular haunch that can be cut from W section or welded from plate. In Figure 2.2 a triangular haunch was welded beneath the beam bottom flange in order to limit stress values in beam-column connection groove welds. Although the welded haunch modifications that have haunches both bottom and top beam flanges showed better seismic performances than one-sided welded haunch types (SAC 1996), only bottom side WH type was preferred in this study because the purpose of this experimental study was particularly for the rehabilitation of the existing steel moment frame structures. For the existing structures, removing the concrete slab around the column creates problems in terms of economical considerations. On the other hand, the presence of the concrete slab makes the application of top flange haunch type difficult for the new constructions.

The tapered haunch could be constituted in two ways. It could be constituted with a flange and web plate or could be cut from a structural tee or wide flange section (AISC 2003a). In addition, a pair of beam web stiffeners should be provided at the end of the haunch in order to contribute the vertical load distribution in the beam web.

Chi, et al. (2006) experimented six large-scale steel moment connections including two Pre-Northridge and four rehabilitated specimens. In seismic rehabilitations both welded haunch and rib plates were used aiming at limiting strain demands at the beam flange groove welds. According to the conclusions based on the experimental study, the proposed rehabilitation method was effective at preventing brittle weld fracture and all rehabilitated specimens managed to exceed 4% interstory drift angle. In addition, this study has proved the inclination angle of the haunch could be up to 50 degrees on the contrary of the AISC design procedure that limited haunch angle to 30 ±5 degrees.

Yu and Uang conducted both theoretical and experimental study at University of California San Diego (UCSD) (Uang, et al. 2000, Yu, et al. 2000). They found that welded haunch (WH) changed the beam shear force transfer mechanism and behaved as a “diagonal strut” that transferred the majority of shear forces within the haunch flange to the column. Two large-scale two-sided steel moment connections with WH

tests showed great seismic performances. Especially, the specimen having a composite slab did not experience any brittle fractures. This study also demonstrated that no modifications in existing beam flange groove welds were needed when a welded haunch was welded to the bottom flange.

In the experimental program at the University of Texas, Austin, Civjan and Engelhardt have tested four steel moment frame (SMF) connections retrofitted with welded bottom flange haunch. Specimens with welded haunch especially having composite slabs on them showed outstanding seismic performances, even though they had no modifications in their existing beam flange groove welds (Civjan, et al. 2001).

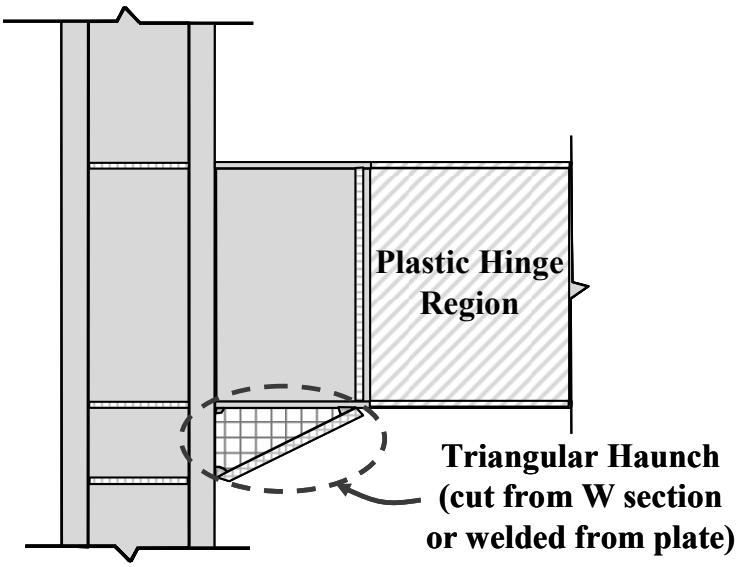

Figure 2.2. Details of Welded Haunch Connection
(Source: AISC 2003a)

2.3. Fiber Reinforced Polymer (FRP) Literature

2.3.1. FRP Materials

Fibers are very popular in strengthening and repair applications in structural engineering industry due to their properties, high elastic modulus and high strength. Fiber reinforced polymer (FRP) composite materials bring together these

characteristics with a low modulus binding matrix that ensures load transfer between the fibers. Especially, glass, carbon, aramid fibers and hybrid usage of these materials have been utilized in civil engineering applications. The stress-strain behaviors of these fibers are presented in Figure 2.3.

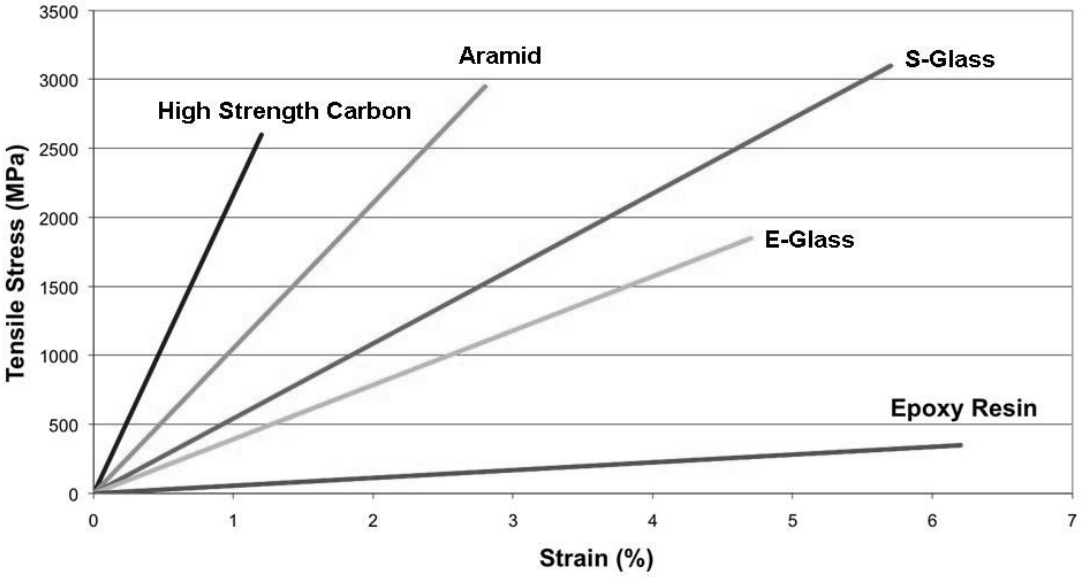

Figure 2.3. Tensile Stress and Strain Diagram of Fibers
(Source: Gutowski 1997)

Glass fiber reinforced polymer (GFRP), carbon fiber reinforced polymer (CFRP) materials have been utilized in rehabilitation applications mostly. CFRP has three types known as high strength (hsCFRP), high modulus (hmCFRP) and ultra-high modulus (uhmCFRP) and it has been used more than GFRP in structural retrofitting practices. However, GFRP is more cost-effective than CFRP (Cadei, et al. 2004). The orientation of the fibers plays an important role for FRP composite materials at having different strength and stiffness characteristics as well as fiber type. Typical properties of steel-FRP systems are shown in Table 2.1.

Table 2.1. Typical Properties of Steel-FRP Systems
(Source: Harries and El-Tawil 2006)

	Mild Steel	hsCFRP	hmCFRP	uhmCFRP	GFRP
tensile modulus, GPa	200	166	207	304	42
tensile strength, MPa	276-483	3048	2896	1448	896
ultimate strain, %	18-25	1.8	1.4	0.5	2.2

2.3.2. FRP-Steel Applications

2.3.2.1. Flexural Strengthening Applications

Buyukozturk, et al. (2004) investigated the efficiency of FRP retrofitting method for steel and reinforced concrete structures in terms of debonding problems and stated that debonding is very critical phenomenon creating problems in these applications.

Schnerch, et al. (2005) investigated the bond behavior of high modulus CFRP strengthened steel bridges and structures. Surface preparation techniques and means preventing galvanic corrosion were discussed and conducted an experimental study consisted of wide flange steel beams having bonded CFRP strips in the tension flange with different development lengths and adhesives. Different failure types observed in the experimental program showed the importance of the selection of adhesive type through determination of development length.

Photiou, et al. (2006) studied the effectiveness of high modulus and ultra-high modulus CFRP/GFRP hybrid prepregs at increasing flexural capacity of steel members in strengthening applications. In experimental study, four degraded steel beam of rectangular cross section were tested under four-point loading. Two of the beams were strengthened by U-shaped prepregs, which continued to the mid-point of the rectangular beams in the vertical axis while the remaining two beams were strengthened by a flat prepreg. The authors reported that the failure load for all

specimens exceed the plastic collapse load of the undamaged beam and U-shaped prepregs had better performance even at failure levels while debonding was observed for the specimens, which have fiber layers only on the soffit.

Tavakkolizadeh and Saadatmanesh (2003a) tested three undamaged steel-concrete composite girders, which have one, three and five layers of CFRP sheets only at their tension flanges, respectively. Ultimate load-carrying capacities increased up to 76% through CFRP retrofit. However, insignificant increase at elastic stiffness was observed due to the flexibility of adhesive. The authors stated that balanced design should be necessary for CFRP utilization on the account of the fact that the efficiency of CFRP decreases as the number of layers increases. Significant strain reduction in the tension flange was observed in the post-elastic region while little amount of inelastic region.

Tavakkolizadeh and Saadatmanesh (2003b) also tested three damaged composite steel girders, which have 25, 50 and 100% loss of cross-sectional area at their flanges, respectively. Similar to the previous study, the girders were strengthened with one, three and five layers of CFRP sheets according to damage severity. Tavakkolizadeh and Saadatmanesh mentioned that CFRP retrofitting increased the ultimate load-carrying capacities and elastic stiffness of the girders significantly and they also stated that the improvements on the post-elastic stiffness were much more pronounced.

Al-Saidy, et al. (2004) studied the behavior of steel composite beams that have a portion of the flange removal simulating corrosion damage. Specimens were repaired with CFRP plates at their tension flanges and were experimented to failure. Test results showed that elastic stiffness recoveries were observed up to 50% through CFRP plate repair.

El Damatty, et al. (2005) conducted a finite element based study in order to enhance flexural capacity of steel girders using GFRP. The authors stated that using GFRP instead of CFRP in this rehabilitation study was due to three facts:

1- Due to the superior properties of the CFRP sheets, failure of the retrofitted steel member generally occurs in the adhesive and thus the capacity of the CFRP sheets is not fully utilized,

2- Galvanization can occur when steel and carbon surfaces are in direct contact,

3- CFRP cost is much higher than that of GFRP.

In this analytical study, three different length values were used for the bottom girder flange retrofit with heavy-duty adhesive system the values of which obtained from the study having various adhesives (El Damatty and Abushagur 2003). According to the analysis based on the critical load configuration, 25% increase in the load carrying capacity was achieved with this rehabilitation method.

Sen, et al. (2001) studied the feasibility of using CFRP laminates for steel bridge girders repairing applications. The main objectives of this study were to develop a procedure for strengthening composite steel girders with CFRP laminates, evaluate retrofitting benefits, and assess finite element predictions with experimental results. Six 6.1 m long W8x24 steel beams were first loaded until they past the yield strength of the tension flange. Then they were strengthened using 3.65 m lengths of 2 or 5 mm thick CFRP laminates bonded to the tension flange. Specimens were tested until they failed. The authors stated that CFRP strengthening application for composite steel girders were feasible due to the ultimate strength gains with a relatively modest improvement in elastic response.

Dawood (2005) conducted three-phased experimental program related to the strengthening of composite steel bridge girders with high modulus CFRP (HM CFRP), which has larger elastic modulus than that of steel. In the first phase, researchers investigated the feasibility of strengthening application such as selection of appropriate resin and adhesives. Various strengthening configurations and the behavior of strengthened beams under overloading and fatigue loading conditions were studied in the succeeding phases. The research program showed that the presence of HM CFRP materials increased the elastic stiffness, yield load and ultimate capacity as well as it reduced residual deflection related to over-loading condition. After the investigations, HM CFRP strengthening application was found effective for the steel-concrete composite bridge girders.

Lenwari, et al. (2005) tested seven W100x17.2 steel beams with three different CFRP length configurations and evaluated the flexural behavior of strengthened specimens. Two different failure modes were observed related to CFRP length in consequence of the experiments. Specimens that have long CFRP plates experienced plate rupture failure while specimens that have short plates debonding.

Nozaka, et al. (2005) studied the use of CFRP strips for the rehabilitation applications of fatigue-damaged steel bridge I-girders. They tested many repair

alternatives having variables including CFRP type and bond length, adhesive type, adhesive thickness and bonding configurations in order to find effective bond length. Experimental and analytical investigations showed that ductile adhesives were more effective for redistributing the stresses successfully as loading increased and decreasing bond length requirement.

2.3.2.2. Fatigue Repair Applications

The effectiveness of CFRP overlays for repair of fatigue cracks and increasing fatigue life were investigated by Jones and Civjan (2003). Twenty one edge notched and eight with center hole specimens were tested in order to determine the effect of many variables including development length, bond area, application regions, CFRP application timing according to crack propagation. Experimental results demonstrated that the fatigue life increased by means of the contribution of CFRP materials. In addition, variables that were tested were effective in determining of the overall performance.

Tavakkolizadeh and Saadatmanesh (2003c) studied fatigue life behavior of steel girders having CFRP plate strengthening application at their tension flanges. Twenty-one S127x4.5 A36 specimens were tested under four point loading with the applied stress ranged from 69 to 379 MPa. Unretrofitted specimens were tested as control specimens. On the other hand, retrofitted specimens have same CFRP patch length and thicknesses. The authors came into conclusion that CFRP patches extended the fatigue life of the notched detail more than three times and decreased crack growth rate in a pronounced manner.

2.3.2.3. Enhancing Stability Applications

Ekiz, et al. (2004) investigated using CFRP wraps in double-channel truss members to enhance the plastic hinge behavior. The experimental study consisted of two cases in the plastic hinge region, one where the entire gross cross section is wrapped, the second where only the extending flanges are wrapped. According to this experimental study, authors reported that the presence of the CFRP wrap increased

the size of the yielded plastic hinge region, inhibited the occurrence of local buckling and delayed the lateral torsional buckling resulted in reduced strain demands, increased rotational capacity, and improved energy dissipation capacity in the plastic hinge region.

Ekiz and El-Tawil (2006) performed an analytical and experimental research program in order to investigate the effect of CFRP wrapping on the buckling behavior of compressive steel members. The researchers implemented mortar or PVC blocks on the steel member aiming at improvements on CFRP wrapping and conducted twenty- two small-scale tests. The authors developed a simulation model, which was consistent with the experimental results including load deflection response and mode of failure. Experimental and analytical results showed that significant improvements observed to be a function of CFRP layers and core material thickness can be obtained in the buckling behavior of steel members using CFRP wrapping. The authors also stated that using mortar as core material was more successful than using PVC blocks.

A follow-up study by Ekiz and El-Tawil (2008) was performed for inhibiting the buckling response of steel braces using entire system CFRP wrapping with the mortar blocks. Seven large-scale specimens were subjected to reverse axial loading. Experiments made demonstrated that buckling restrained response was obtained up to 2% interstory drift and strengthening concept performance were related to the fiber layers, mortar size, presence of bond between steel plate and mortar and extra stitch plates. In addition, double angle members performed better in the strengthening application than single members. The authors stated that CFRP wrapping was effective for strengthening steel braces in the applications where inelastic member behavior was not expected.

A non-linear finite element analysis was conducted by Shaat and Fam (2007) for axially loaded slender hollow structural section columns (HSS) that have high modulus CFRP strengthening application and results were verified by means of analytical and experimental studies. In the parametrical study, geometric and material nonlinearities, column's initial imperfection, steel plasticity and residual stresses were taken into consideration and five 89x89x3.2 mm HSS sections that have slenderness ratio of 68 were tested. A single high modulus CFRP layer that has 0.54 mm thickness, 510 MPa tensile strength and 230 GPa elastic modulus was bonded longitudinally on glass fiber reinforced polymer (GFRP) layer, which was bonded

aiming at preventing galvanic corrosion. The four specimens which have zero, one, three and five CFRP layers, respectively were applied on two opposite sides of sections while the fifth specimen that has three CFRP layers was applied on all sides of section. In consequence of this study, Shaat and Fam (2007) concluded that longitudinally high modulus CFRP strengthening concept was an effective method in order to increase axial strength and stiffness and postpone buckling of columns. They also emphasized that CFRP retrofit was more effective when the slenderness ratio of columns increased and mentioned residual stresses affected CFRP performance to a small extent.

In the continuation study, Shaat and Fam (2009) investigated strengthening HSS columns with longitudinal high modulus CFRP plates and tested eighteen 44x44x3.2 sections in axial compression. They also developed an analytical model to predict the ultimate axial load capacity of strengthened sections. Experimental results demonstrated that CFRP strengthening was more effective for the sections that have high slenderness ratios in terms of axial strength increase. The increase on axial stiffness was also observed; however, it was slightly dependent to the slenderness ratio. The authors came into conclusion that slenderness ratio determined the failure behavior.

Harries, et al. (2009) conducted an experimental study utilizing FRP materials to provide bracing effect in order to have stability enhancements with limitations on local and global buckles. WT 155x10.5 steel sections were strengthened with both ultra high modulus GFRP and high strength CFRP plates with various thickness and width values. Strengthened sections were tested under compressive loading to failure. The authors stated that FRP retrofit had minor effects on elastic buckling behavior while it provided improvements at local buckling behavior and increased the load carrying capacity related to the increase in effective radius of gyration. They also emphasized that the presence of FRP controlled the plastic buckling prior to debonding and caused to delay plastic kinking. In addition, they proposed that FRP retrofitting studies should be performed in a seismic lateral force resisting system in order to meet ductility and energy absorption requirements.

Sayed-Ahmed (2006) proposed the use of CFRP strips applied horizontally to the compression zone of slender-webbed steel sections and investigated the contribution of CFRP strips in delaying local web buckling. The results of this

analytical study showed that the local buckling of beam webs could be delayed due to the increases in critical load and ultimate capacity using CFRP strips.

Accord and Earls (2006) conducted a nonlinear finite element based study in order to investigate ductility enhancement in structural steel beam members utilizing GFRP. GFRP strips were placed in the compression flange of the beam plastic hinge region aiming at providing bracing which prevents the formation of the local buckles in the compression flange of the cross-section. This reinforcing strategy increased the flexural strength of the beams by 25% and significantly improved the ductility of the beams when compared with bare steel members. The location and length of the GFRP strips were also investigated. Using GFRP strips on half the beam length possessed the same effect as using the strips on the full beam length while decreasing GFRP strip length to quarter the beam length reduced ductility and ultimate moment capacity in member. The study also showed that the most effective location to place the strips was adjacent to the flange tips since local buckling is more severe at flange tips rather than closer to the web.

CHAPTER 3

EXPERIMENTAL STUDY

3.1. Introduction

The experimental program consisted of the design and construction of the test setup, design and construction of the cantilever beam-column assembly and testing of the cantilever beams with and without welded haunch modification. In the first phase, for welded haunch modification experiments, one bare HE400AA beam and three HE400AA beams reinforced with glass fiber reinforced polymer (GFRP) were tested. Bare beam was the control specimen and other three beam tests were made with specimens having different GFRP layers and different application procedures. HE500AA beams were tested with no modification as the second phase of the experiments. Like the first phase, one HE500AA beam was tested as bare beam while the two other HE500AA beams were tested with GFRP reinforcement. Initially, reduced beam section (RBS) improvement was planned for the HE500AA beam sections. However, analytical results (Alkan 2008, Ozdemir 2009) carried out in this research project showed that GFRP reinforcement was not effective for the sections having RBS improvements. GFRP application procedures including GFRP length in plastic hinge region and number of GFRP layers in these large-scale experiments were determined in accordance with the analytical studies (Ozdemir 2009) and small scale standard tests (Guven 2009).

3.2. Loading System

Cantilever experiments were conducted by a displacement controlled loading system purchased from MTS, USA. The loading system is capable of controlling displacements at moderate frequencies. The capacity of the actuator was 445 kN in tension and 650 kN in compression.

3.3. Test Beams

In the large-scale steel experiments, two different beams were used. HE400AA beams were tested with WH modification while HE500AA beams were experimented with no modification. As mentioned previously HE500AA beams were not tested with RBS modification due to the obtained analytical results, which demonstrated GFRP reinforcement was not effective for RBS sections. For the cantilever beams, HE400AA shallow sections (flange slenderness ratio = 11.5 and web slenderness ratio = 31.4) and HE500AA shallow sections (flange slenderness ratio = 10.7 and web slenderness ratio = 37.1) were used in the experiments.

3.3.1. Tensile Coupon Standard Tests

Tensile coupon tests were conducted following the ASTM (2003) standard. A total number of 9 specimens were cut from the beam section: 3 pieces from the top flange, 3 pieces from the web, and 3 pieces from the bottom flange. The web coupons were cut from the middle of the web and flange coupons were cut from the edges of the flanges. Results from the standard tensile coupon tests are presented in Table 2.1. Each value shown in the table is the average of test results obtained from three samples.

Table 3.1. Standard Tensile Coupon Test Results

Section	Location	Yield Strength (MPa)	Ultimate Strength (MPa)	% Elongation
HE 400 AA	Top Flange	413.1	487.1	42.0
HE 400 AA	Web	436.1	520.7	33.8
HE 400 AA	Bottom Flange	414.8	488.4	42.6
HE 500 AA	Top Flange	329.4	427.9	43.5
HE 500 AA	Web	379.5	465.9	33.5
HE 500 AA	Bottom Flange	330.6	430.5	42.0

3.3.2. Properties of the Sections

Nominal dimensions and properties of steel beam sections are given in Table 3.2. In Table 3.2, h = height of the section, bf = width of the flange, tw = thickness of the web, tf = thickness of the flange, Z = plastic section modulus of the section, and Mp = plastic bending moment calculated using the nominal yield strength (Fy). The actual dimensions of the sections were measured in several points and the averages of these dimensions are tabulated in Table 3.3. The other parameters that are presented in Table 3.3 are the section modulus of the flange using the measured dimensions (Zf), the section modulus of the web using the measured dimensions (Zw), and the value of plastic moment (Mp) calculated using the measured plastic section modulus and measured yield strengths. Comparing Table 3.2 and Table 3.3 reveals that the plastic moment capacities of both HE400AA and HE500AA sections calculated using the actual dimensions and yield strength values are much higher than the plastic moment capacities of the sections calculated using the nominal dimensions and yield strength values. For HE400AA the increase in Mp is 21.2% while for HE500AA is 22.7%.

Table 3.2. Nominal Dimensions and Properties of Sections

Section	h (mm)	b_f (mm)	t_w (mm)	t_f (mm)	FSR (bf/2tf)	WSR (h/tw)	$Zx10^3$ (mm3)	F_y (MPa)	Mp (kN-m)
HE 400 AA	378	300	9.5	13	11.54	31.4	1824	355	647.5
HE 500 AA	472	300	10.5	14	10.71	37.1	2576	275	708.4

Table 3.3. Actual Dimensions and Properties of Sections

Section	h (mm)	b_f (mm)	t_w (mm)	t_f (mm)	Z_f (mm^3)	Z_w (mm^3)	M_p (kN-m)
HE 400 AA	381.5	302	9.8	13	1574191	308935	785.0
HE 500 AA	474	302	10.8	13.5	2013545	539484	869.2

It is necessary to calculate the expected moment in the plastic hinge region of the cantilever beams in order to design the test setup efficiently. Expected plastic moment during testing will be greater than the plastic moment calculated above. Some of the reasons for this are strain hardening and local restraints at the connections. ANSI/AISC 358-05 (AISC 2005a) specification suggests using the following equation to calculate the maximum plastic moment expected in the plastic hinge region (AISC 2005a Equation 2.4.3-1):

$$M_{pr} = C_{pr} R_y F_y Z_e, \tag{3.1}$$

where:

M_{pr} = maximum moment expected in the plastic hinge region (N-mm)

R_y = ratio of the expected yield stress to the specified minimum yield stress (AISC 2005b Table I-6-1)

Z_e = effective plastic modulus of the section at the location of the plastic hinge (mm^3)

C_{pr} = factor to account for peak connection strength, including strain hardening, local restraint, other connection conditions:

$$C_{pr} = \frac{F_y + F_u}{2F_y} \le 1.2 \, (AISC\ 2005a\ Equation\ 2.4.3-2), \tag{3.2}$$

F_y = specified minimum yield stress of steel (MPa)

F_u = specified minimum tensile strength of steel (MPa)

C_{pr} was taken 1.1 according to Equation 3.2 while R_y was taken 1.0 due to the consideration of standard coupon test results in calculations. However, the maximum expected moment calculated using Equation 3.1 would still be exceeded for beams with GFRP strips. Accord and Earls (2006) have shown that the addition of GFRP strips can increase the plastic moment by 25%. Therefore, the maximum moment (M_{max}) expected in the plastic hinge region of HE400AA with GFRP was taken as 1.3 times the value calculated by Equation 3.1:

$$M_{\max} = 1.30 M_{pr}, \tag{3.3}$$

The maximum moment expected in the experiments have been calculated for HE400AA and HE500AA beams by using Equation 3.3 as follows:

$M_{max} = 1.3 \times 1.1 \times 1.0 \times 785 = 1123$ kN-m (HE400AA)

$M_{max} = 1.3 \times 1.1 \times 1.0 \times 869.2 = 1243$ kN-m (HE500AA)

The length of the test beam was calculated by taking into consideration the above maximum moment value and the expected rotation value of the beams (beam end displacement / beam length). The actuator has a capacity of 445 kN in tension and 650 kN in compression, with a 500 mm stroke. The M_{max} value of the beam was 1243 kN-m for HE500AA test beam. When the beam length is chosen as 3.9 m, it would be possible to apply a 445 kN × 3.9 m = 1735 kN-m moment to the plastic hinge region.

In addition to the maximum moment, the rotation of the test beam also needed to be checked. The drift angle (Figure 3.1) expected from special moment resisting frames is at least 0.04 rad as explained in the previous chapters. In this study, the expected rotation of the cantilever beam was also set to at least 0.04 rad. Since the tip of the stroke of the actuator would be connected to the middle of the beam web, the tip of the beam would be able to move 250 mm upwards and 250 mm downwards. In such a case, the rotation of the HE400AA beam with a length of 2.9 m will be 250 mm / 2900 mm = 0.08 rad while the rotation of the HE500AA beam with a length of 3.9 m will be 250 mm / 3940 mm = 0,064 rad.

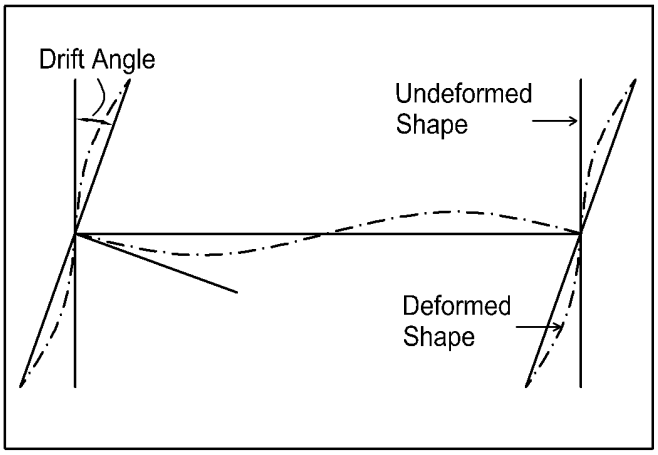

Figure 3.1. Interstory Drift Angle

3.4. Test Setup

In order to conduct the cantilever beam tests, a reaction wall was designed and constructed. The plan view of the reaction wall can be seen in Figure 3.2 and sections of the reaction wall can be seen in Figure 3.3 and Figure 3.4. This system consisted of two steel frames (A-B and C-D frames) with two HD400×237 columns as seen in these figures. In order to split the shear and moments that will be created during the tests evenly between the two frames, the test set up was designed to allow the connection of the test beams right between the two frames through a column bolted to six HE400A beams bolted transversely to one column in each frame (Columns A and C as seen in Figure 3.5 and Figure 3.6).

These six 1400 mm long HE400A beams were bolted to columns A and C with M27 bolts, forming a wall between columns A and C. An HD400×187 column was bolted transversely to the middle of the six HE400A beams (Figure 3.5 and Figure 3.6). HE400A and HD400×237 members were reinforced with stiffeners in necessary locations to prevent local buckling. The test beams were welded to 50 mm thick plates and these endplates were bolted to the HD×400×187 column. By this modification, the HD×400×187 column stayed in place on both of the beam tests.

In order to prevent lateral torsional buckling of the test beams two small frames were constructed as shown in Figure 3.5 and Figure 3.6 and teflon materials were attached to the flanges of the test beams in the intersection regions with these frames. Thus, test beams were able to perform vertical movement in the course of experiment properly.

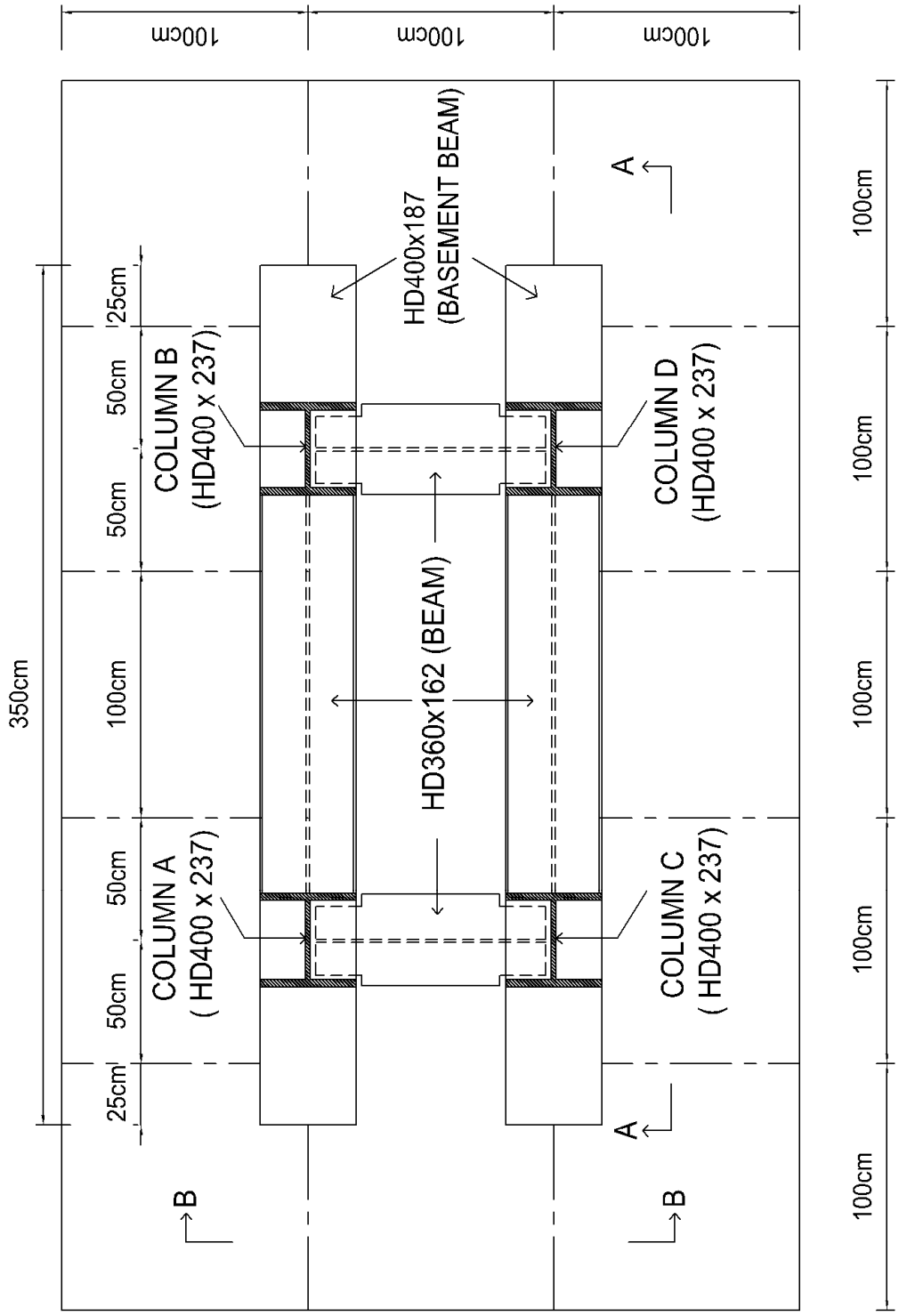

Figure 3.2. Plan View of Reaction Wall

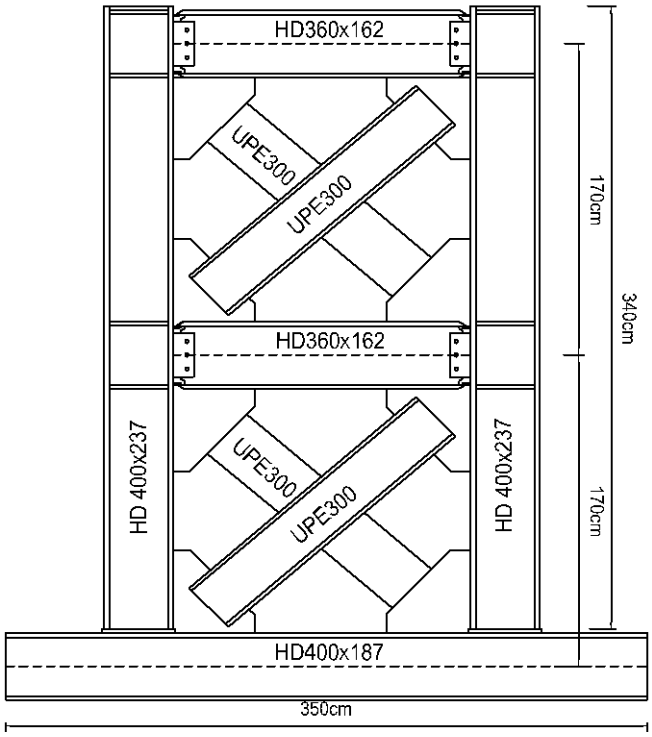

Figure 3.3. Section A-A of Reaction Wall

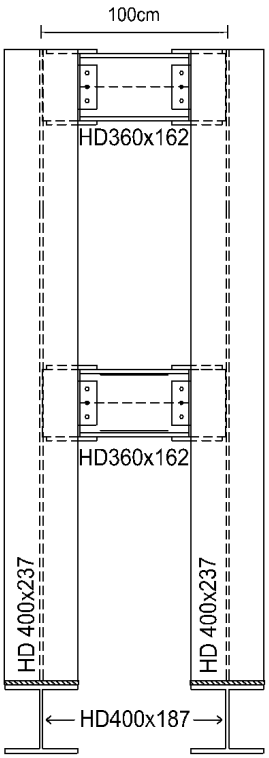

Figure 3.4. Section B-B of Reaction Wall

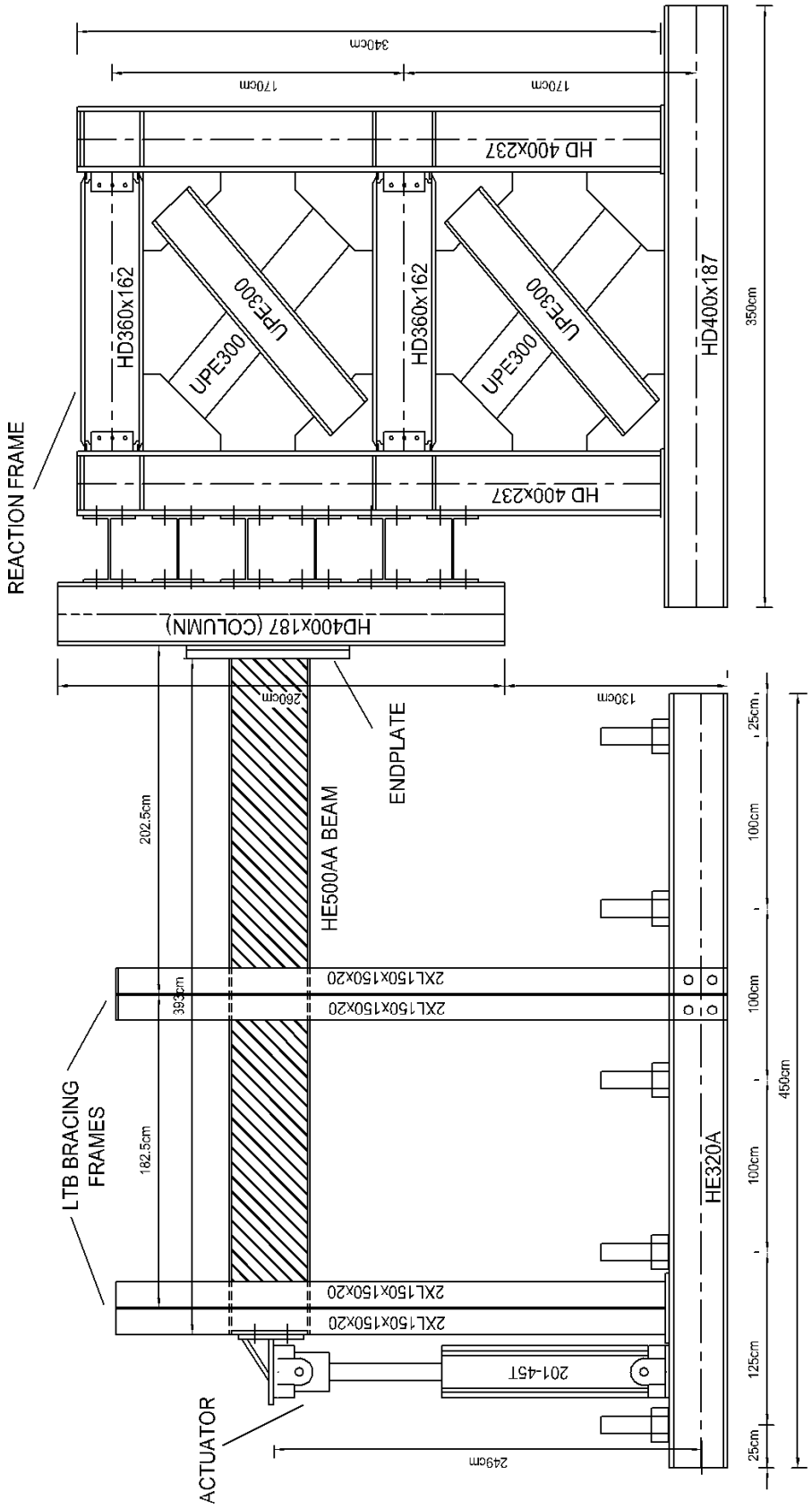

Figure 3.5. Test Beam and Test Setup

Figure 3.6. Photograph of Test Setup

3.5. Loading Protocol

The loading protocol to be followed in the cyclic tests of steel I-sections is shown in Figure 3.7 (AISC 2005b). Both HE400AA and HE500AA beam tests were performed in accordance with this loading protocol, except that beam fixed-end rotation for HE400AA beams and beam rotation at WH tip for HE500AA beams were used instead of inter story drift angle as y-axis in order to provide clear comparison between beam specimens.

3.5.1. Relationship between Test Setup and Loading Protocol

Both HE400AA and HE500AA beams were welded to 50 mm thick plates and these endplates were bolted to the HD×400×187 column in order to recycle the column for the other tests. However, designed connection has inherent flexibility, which reflected the beam as rigid body rotation. This rotation was measured with the linear variable differential transducers (LVDT) and incorporated to the calculations to determine the actual beam fixed-end rotation. Because this rotation could not be predicted prior to the test, slight deviations from AISC (2005b) loading protocol were inevitable during testing. Thus somewhat different load cycles from AISC (2005b) loading protocol were obtained in both HE400AA and HE500AA beam experiments and they are stated in the following chapter.

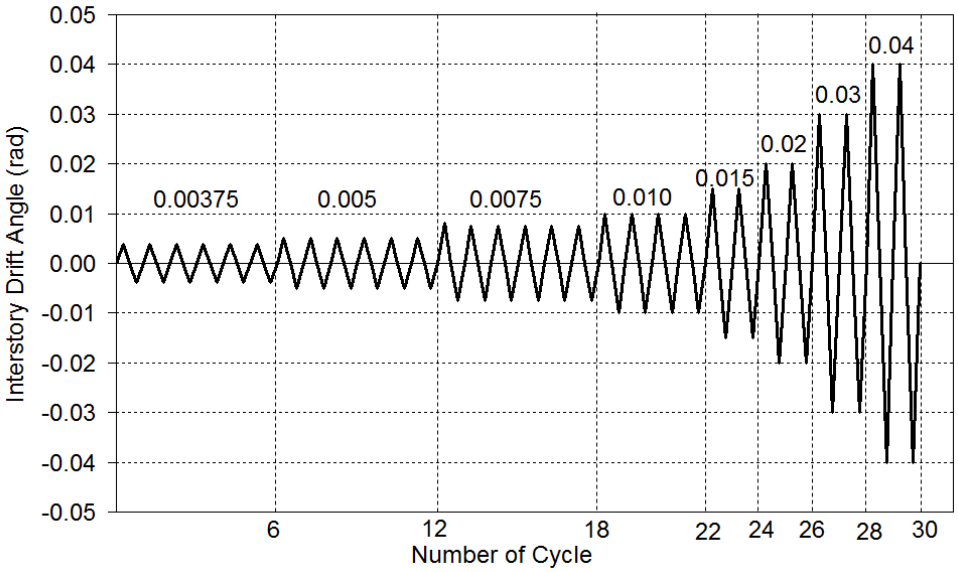

Figure 3.7. Loading Protocol (AISC 2005b)

3.6. Instrumentation

Linear variable differential transformers (LVDT) and strain gauges were installed to measure displacement at the tip of the beam, displacements at the top and

bottom of the 50 mm plate that the beams were welded and strains at the critical regions for the beam flanges and glass fiber reinforced polymers (GFRP).

3.6.1. Linear Variable Differential Transducers (LVDT)

In this experimental study, three Omega LD 600 type LVDTs were used. LVDT1 that measured beam tip displacement has +/- 150 mm displacement range while LVDT2 and LVDT3 have +/- 50 mm displacement range (Figure 3.8). LVDT2 and LVDT3 measurements taken from the 50 mm plate that the beam was welded were used to calculate the rotation of the test frame, which was subtracted from the total rotation of the beam to calculate the actual rotation. All transducers were channel calibrated prior to each test using data acquisition software.

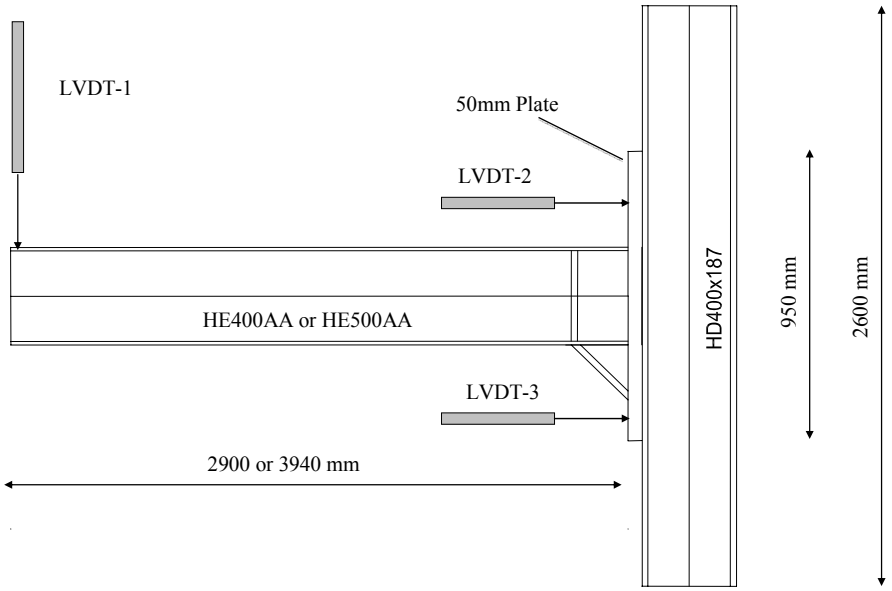

Figure 3.8. Locations of LVDTs

3.6.2. Strain Gages

Three types of strain gauges manufactured by Tokyo Sokki Kenkyujo Co., Ltd. were used at the large-scale steel beam-column experiments. YFLA-5, FLA-3-350-11-1L and BFLA-2-5-1L were used at the beam flanges, at the flanges of welded

haunch and on the GFRP material, respectively. YFLA-5 strain gauges are capable of large strains while FLA-3-350-11-1L strain gauges are suitable to take readings in elastic limit of steel material. Due to the aforementioned strain gauge characteristics, all strain gauges located at the beam flanges were post yield strain gages (YFLA-5). The only two strain gauges located at the flange of left and right side of welded haunch were selected as FLA-3-350-11-1L because no yielding was expected at the side of the welded haunch.

HE400AA beam steel strain gage layout and composite strain gage layout are shown in Figure 3.9 and in Figure 3.10, respectively. SG-L401, SG-L402 and SG-L403, which were located at the side of the beam flanges, were used in only HE400AA GFRP2 experiment. Top flange steel strain gages (SG-401, SG-402 and SG-403) were mounted on the top of the top flange, at 75 mm from the endplate while gages (SG-406, SG-407 and SG-408) were mounted at 75 mm from the center of the stiffener (295 mm from endplate). Bottom flange steel strain gages (SG-404 and SG-405) were mounted on the top of the bottom flange, at 75 mm from the endplate while gages (SG-409 and SG-410) were mounted at 75 mm from the center of the stiffener (295 mm from endplate). Top flange composite strain gages (SG-C401 and SG-C402) were mounted on GFRP on the top of the top flange, at 75 mm from endplate while gages (SG-C403 and SG-C404) were mounted at 75 mm from the center of the stiffener (295 mm from endplate). Bottom flange composite strain gages (SG-C405 and SG-C406) were mounted on GFRP on the top of the bottom flange, at 75 mm from the center of the stiffener (295 mm from endplate). SG-H401 and SG-H402 were located on the south and north side of the haunch flange, respectively.

HE500AA beam steel strain gage layout and composite strain gage layout are shown in Figure 3.11 and in Figure 3.12, respectively. Top flange steel strain gages (SG-501, SG-502 and SG-503) were mounted on the top of the top flange, at 75 mm from the endplate while bottom flange steel strain gages (SG-504, SG-505 and SG-506) were mounted on the bottom of the bottom flange, at 75 mm from endplate. Top flange composite strain gages (SG-C501, SG-C502 and SG-C503) were mounted on GFRP on the top of the top flange, at 75 mm from the endplate while bottom flange steel strain gages (SG-C504, SG-C505 and SG-C506) were mounted on GFRP on the bottom of the bottom flange, at 75 mm from endplate.

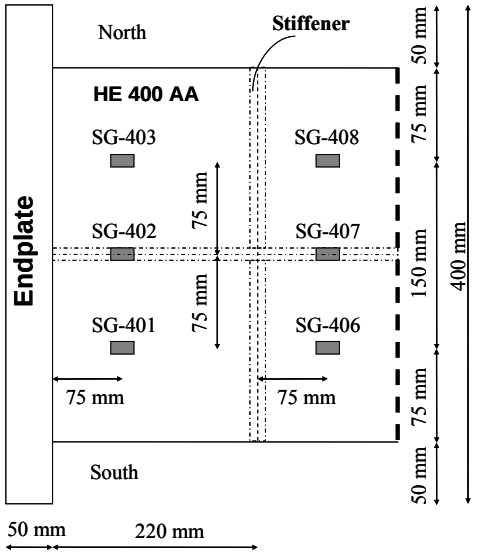

a) Top of the Top Flange

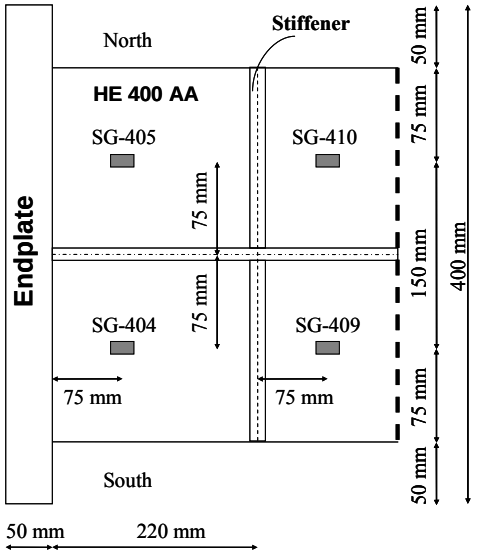

b) Top of the Bottom Flange

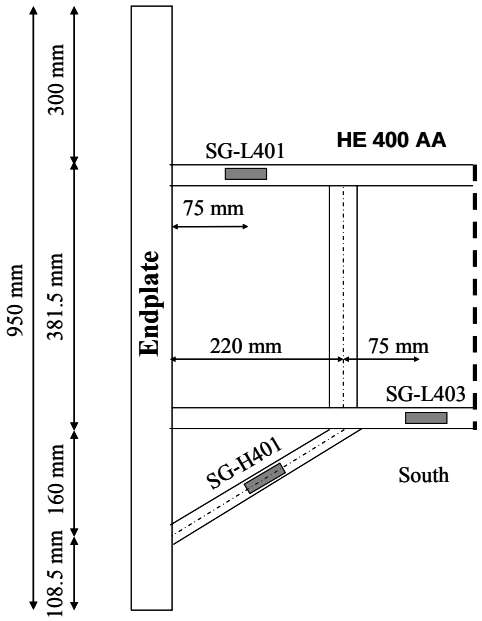

c) South Side of the Connection

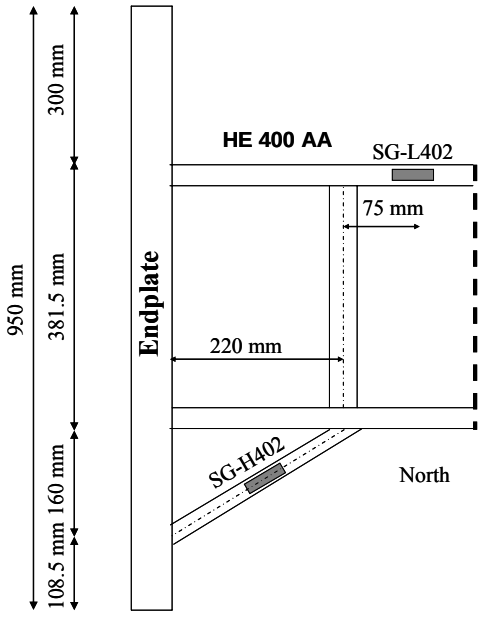

d) North Side of the Connection

Figure 3.9. HE400AA Beam Steel Strain Gauges Layout

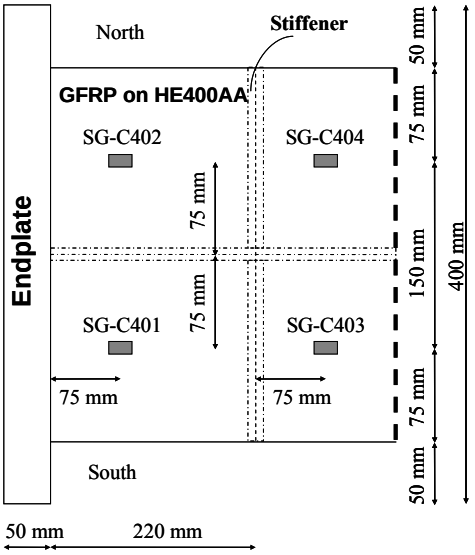

a) Top of the Top Flange

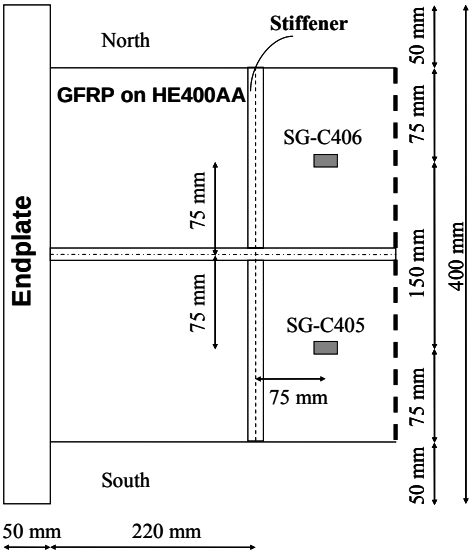

b) Top of the Bottom Flange

Figure 3.10. HE400AA Beams Composite Strain Gauges Layout

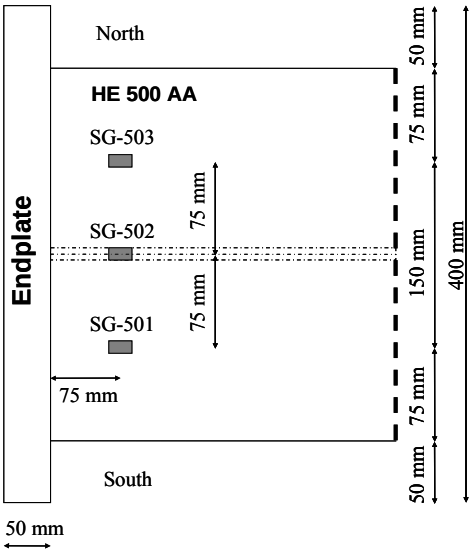

a) Top of the Top Flange

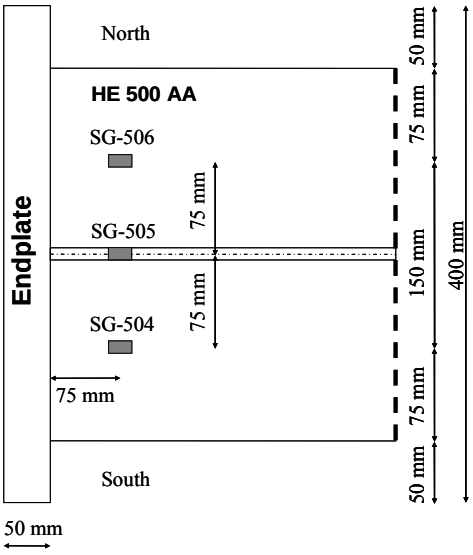

b) Bottom of the Bottom Flange

Figure 3.11. HE500AA Beam Steel Strain Gauges Layout

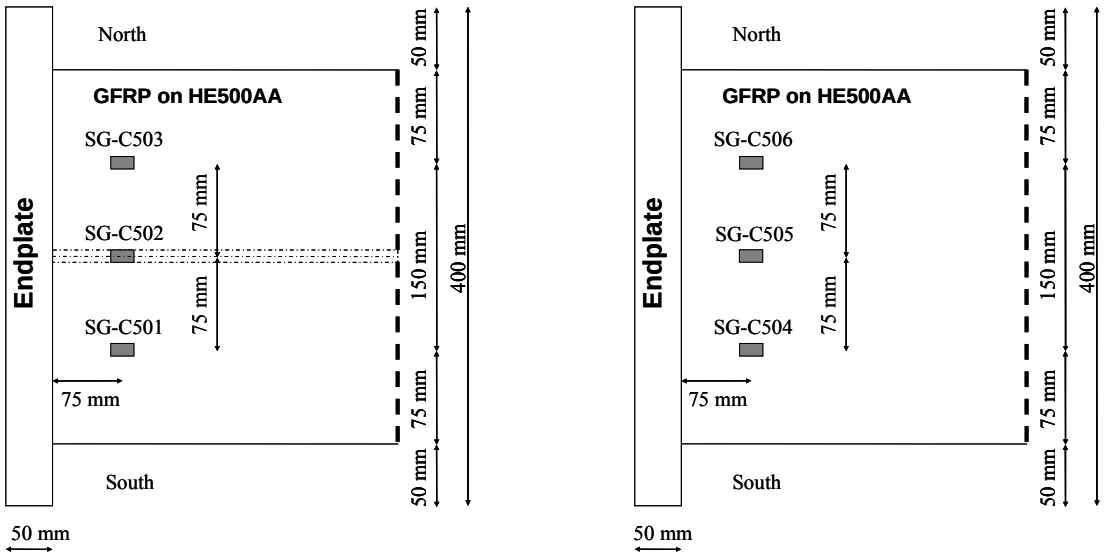

a) Top of the Top Flange b) Bottom of the Bottom Flange

Figure 3.12. HE500AA Beams Composite Strain Gauges Layout

3.6.3. Data Acquisition

National Instruments data acquisition system, which has three modules for strain gauges and LVDTs, were used to gather experimental data. Strain gauge data were collected by means of two modules, each having eight channels while LVDT data were collected through a module with 32-channel capacity. MTS hydraulic actuator has a load cell connected with its assemblies and the load data were collected through MTS dedicated data acquisition system. Obtaining two data per minute was selected for experiment and applied to the two data acquisition (DAQ) systems and the DAQ systems were synchronized by starting at the same time.

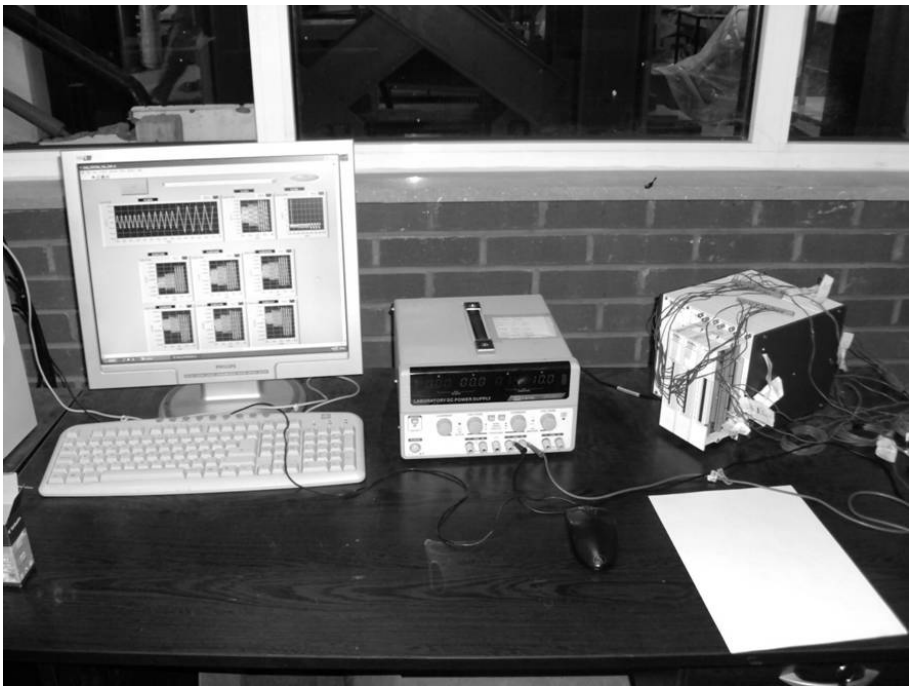

Figure 3.13. Data Acquisition Instruments

3.7. GFRP Applications

3.7.1. Glass Fiber Reinforced Polymer

E-glass fibers with 0°/+45°/90°/-45° fiber orientations provided from Telateks Textile Products Company were used as the reinforcement material for GFRP applications. The tensile strength and specific weight of the fibers given by the manufacturer were 2500 MPa and 1250gr/m^2, respectively.

Epoxy resins are capable of having outstanding bonding characteristics and they are generally preferred for the wet lay-up process GFRP applications (Cadei, et al. 2004). For this reason, epoxy resin that was purchased from Duratek firm was used as binding material in this experimental study in order to apply glass fibers on steel surfaces.

The Duratek DTE 1000+ resin was used with both DTS 1100 and DTS 1105 curing agents in order to create necessary production time of GFRP for the large-scale test beams. Curing compound Duratek DTS 1100 has 30 minutes gel duration

(@23°C, 100ml DIN 1994). Curing compound DTS 1105 has gel duration of 450 minutes (@23°C, 100ml DIN 1994). Physical and mechanical properties of Duratek epoxy given by the manufacturer are presented in Table 3.4 and Table 3.5, respectively. Silane primer prepared in laboratory conditions was used in order to have bond enhancement between the steel surface and GFRP as well.

Mechanical properties of GFRP used in large-scale steel beam-column experiments are shown in Table 3.6. The values were obtained from small-scale standard tests (GFRP tension test, GFRP compression test, lap shear test), which took place in a detailed way in Guven's thesis (2009). On the account of the fact that GFRP materials are used in order to mitigate local buckles under compressive forces, the compressive mechanical properties of GFRP materials have more importance than their tensile mechanical properties and therefore the compressive strength and modulus of GFRP become determining factors in choosing GFRP combination in large-scale experiments (Guven 2009). The most suitable GFRP application in terms of interfacial shear strength obtained from lap-shear test is a configuration, which includes sand papered surface treatment, silan primer type and 80°C primer cure temperature.

Table 3.4. Physical Properties of Duratek Epoxy

Property	**DTE 1000+**	
	DTE 1100	**DTE 1105**
Mixture Ratio by Weight	100+35	100+35
Density (kg/lt) DIN 2001	1.1 ±0.05	1.10 ±0.05
Viscosity (MPa) ASTM 2007	900 ±50	920 ±50
Gel Time(min) @23°C,100ml DIN 1989	30	450

Table 3.5. Mechanical Properties of Duratek Epoxy

Epoxy	**DTE 1000+**	
Curing Component	**DTE 1100**	**DTE 1105**
Tensile Strength (MPa) Cure @ 23°C 7 Days; DIN 1994	70±5	63±5
Tensile Strength (Mpa) Cure @ 23°C 1 Day + @ 50°C 19 hours; DIN1994	80±5	80±5
Modulus of Elasticity (Mpa) Cure @ 23°C 7 Days; DIN 1994	2600±100	2350±100
Modulus of Elasticity (Mpa) Cure @ 23°C 1 Day + @ 50°C 19 hours; DIN 1994	2800±100	2500±100
Elongation (%) Cure @ 23°C 7 Days; DIN 1994	2.15±0.10	2.15±0.10
Elongation (%) Cure @ 23°C 1 Day + @ 50°C 19 hours; DIN 1994	2.00±0.1	2.1±0.1

Table 3.6. Mechanical Properties of GFRP used in Experiments
(Source: Guven 2009)

Fiber Orientation	Tensile Strength (MPa)	Compressive Strength (MPa)	Compressive Elastic Modulus (MPa)	Shear Strength (Duratek Epoxy) (MPa)
0º/45º/90º/-45º	228.8	224.9	10029	10.42

3.7.2. Surface Preparation

Surface preparation is very significant in steel rehabilitation applications with fiber reinforced polymer (FRP) to provide complete and adequate chemical bond formation between steel and FRP. Debonding problem in FRP applications with steel and reinforced concrete can be accomplished with suitable surface preparation (Buyukozturk, et al. 2004).

In this study, surface preparation was conducted to obtain most available bonding surface for GFRP application and prevent unwanted premature bond failure. Initially, steel test beam was cleaned with acetone as a solvent along the GFRP application length to remove dust, grease and other contaminants. After this process, steel surface was sand papered with belt sander machine using number 40, 60, 100 sand papers, respectively until desired surface was obtained. Thus, weak layers such as paint and corrosion products were eliminated. Steel surface was re-cleaned with acetone before surface primer application, which was the last part of surface preparation. As the surface primer, silane was used and this chemical compound was prepared in laboratory conditions before application. In order to combine silane firstly 20% ethanol and 80% deionized water is filled in a container as needed and any acidic substance are added to the mixture until the Ph value reaches 4. Finally, 1% Gglycidoxypropyltrimethoxysilane is added to the mixture. Although not practical for in-situ applications, the silane primer was cured with electrical heaters at about 80°C for about 1 hour.

3.7.3. GFRP Application Process

Direct wet hand lay-up method was preferred for GFRP application in this study as seen in Figure 3.13 because it is a simple manufacturing technique with an opportunity of in-situ application. GFRP materials were produced directly in plastic hinge region of steel beam sections and they cured one week in room temperature to reveal in-situ production quality.

In the aftermath of the wet lay-up application, GFRP materials were clapped between wood plates in order to provide suitable curing condition (see Figure 3.14).

Wood plates were covered with plastic materials aiming at preventing bonding between wood and GFRP. Therefore, there was no problem at separation process of wood from GFRP and suitable mould was obtained.

Figure 3.14. Direct Wet Lay-up Application

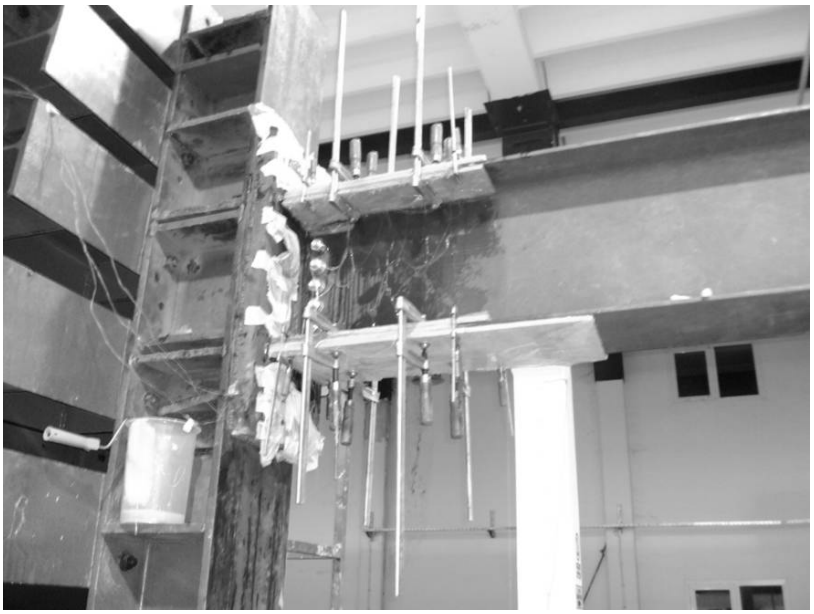

Figure 3.15. Clapping GFRP with Wood Plates

3.7.4. GFRP Applications for the HE400AA Beams

The first HE400AA beam was a control specimen, which did not have GFRP reinforcement. Thus, the contribution of the GFRP materials could be understood comparing the bare beam behavior with that of the GFRP strengthened beams.

The GFRP were wrapped continuously around the plastic hinge region with a length of 400 mm (same as the depth of the beam) for the HE400AA GFRP1 beam and also placed at the top and bottom of the top flange inside the welded haunch (WH) region as seen in Figure 3.16 and Figure 3.17. GFRP materials were placed as three layers, bringing the total thickness of the GFRP to 2.7 mm. At the flanges, the total thickness of GFRP became 5.4 mm as 2.7 mm at the top and 2.7 mm at the bottom of the flange. At the stage of GFRP preparation, fibers were cut without a break along the three fiber layers and so continuity in GFRP was provided. In some portions of the GFRP wrap, perfect bond was not achieved due to workmanship errors. These places were south side of the bottom of top flange, bottom of the top flanges in the WH region, some portions of the south side web at the plastic hinge region.

For the HE400AA GFRP2 test, GFRP materials were applied as five layers and only to the flanges (see Figure 3.18 and Figure 3.19). The length of GFRP was 400 mm, same as beam depth and they applied in the WH region to the top flange while applied in the plastic hinge region both to the top flange and to the bottom flange. In this experiment, GFRP materials were bonded to the top and bottom flanges separately instead of bending to the inner part of the flanges.

In the HE400AA GFRP3 test, GFRP materials were applied as three layers and again only to the flanges (see Figure 3.20 and Figure 3.21). The length of GFRP was 400 mm, same as beam depth and they were applied in the WH region to the top flange while applied in the plastic hinge region both to the top flange and to the bottom flange. However, in this experiment GFRP layers were bonded to the flanges in a bending manner from outer parts of the flanges to the inner parts of them.

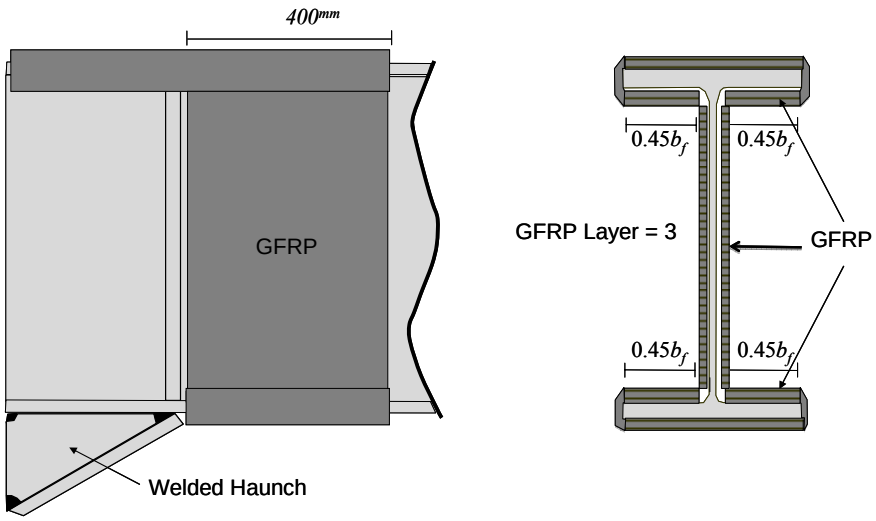

Figure 3.16. GFRP Layout of HE400AA GFRP1 Beam

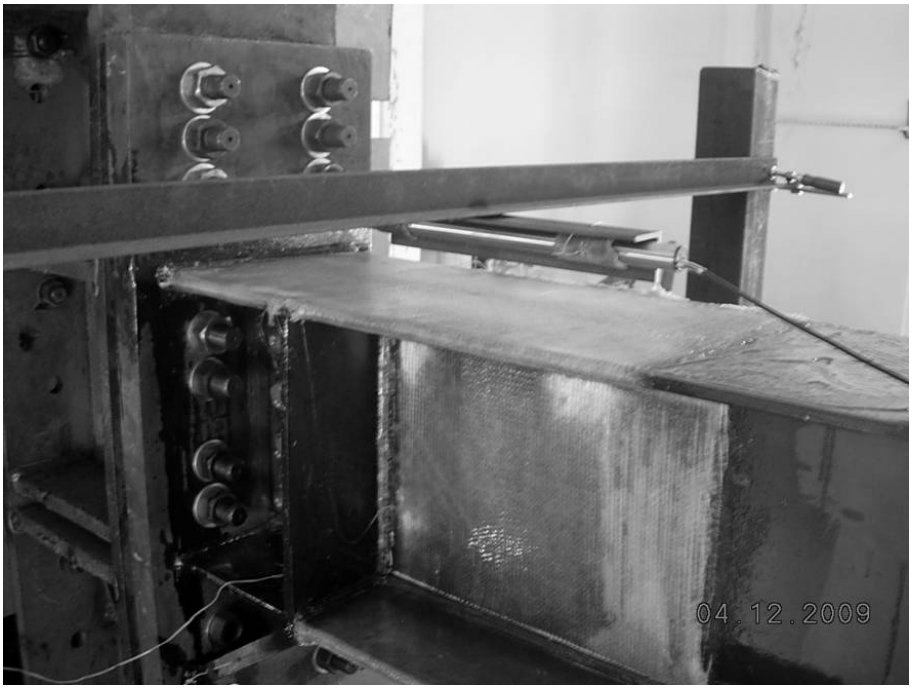

Figure 3.17. HE400AA GFRP1 Beam

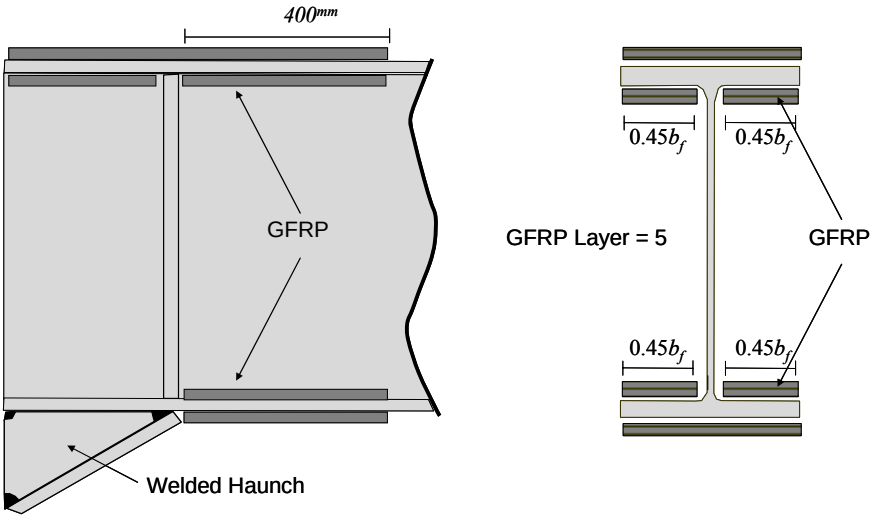

Figure 3.18. GFRP Layout of HE400AA GFRP2 Beam

Figure 3.19. HE400AA GFRP2 Beam

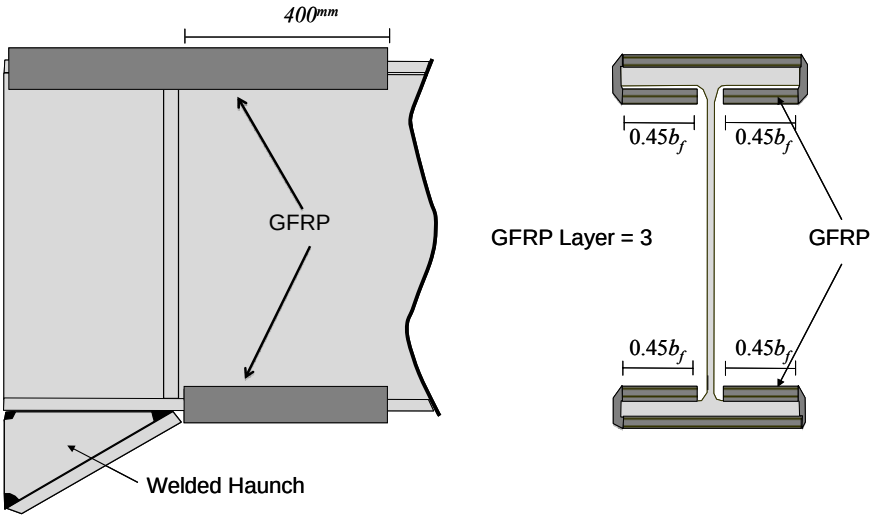

Figure 3.20. GFRP Layout of HE400AA GFRP3 Beam

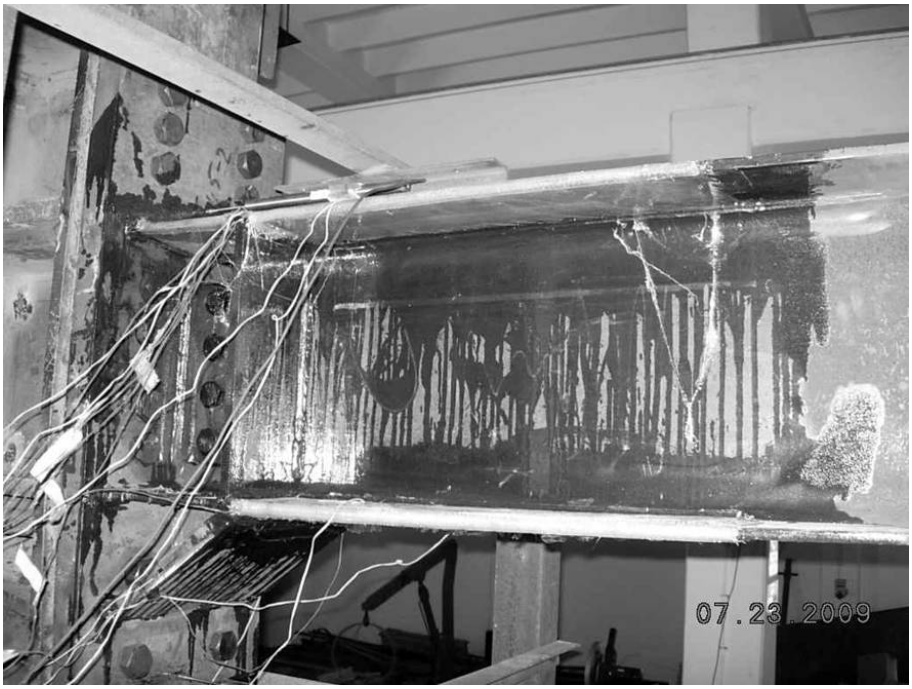

Figure 3.21. HE400AA GFRP3 Beam

3.7.5. GFRP Applications for the HE500AA Beams

The first HE500AA beam was a control specimen, which did not have GFRP reinforcement. Thus, the contribution of the GFRP materials could be understood comparing the bare beam behavior with the GFRP strengthened beams behavior.

In the HE500AA beam with GFRP1 test, GFRP layers were applied as three layers and only to the flanges (see Figure 3.22 and Figure 3.23). The length of GFRP was 500 mm, approximately same as beam depth and they applied in the plastic hinge region both to the top flange and to the bottom flange. GFRP layers were bonded to the flanges in a bending manner from outer parts of the flanges to the inner parts of them.

In the HE500AA beam with GFRP2 test, GFRP materials were applied as three layers again only to the flanges. In addition, anchorage plates were placed on GFRP as three lines for each flange aiming at preventing premature debonding problem. (see Figure 3.24 and Figure 3.25). The length of GFRP was 500 mm, approximately same as beam depth and they applied in the plastic hinge region both to the top flange and to the bottom flange. GFRP layers were bonded to the flanges in a bending manner from outer parts of the flanges to the inner parts of them.

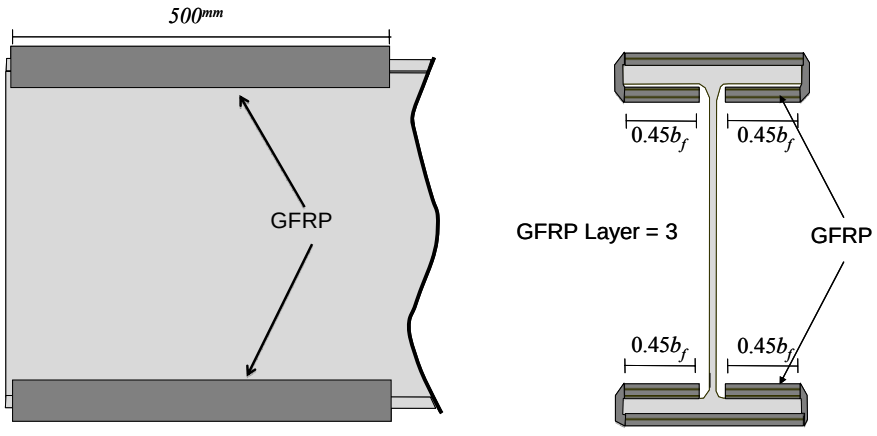

Figure 3.22. GFRP Layout of HE500AA GFRP1 Beam

Figure 3.23. HE500AA GFRP1 Beam

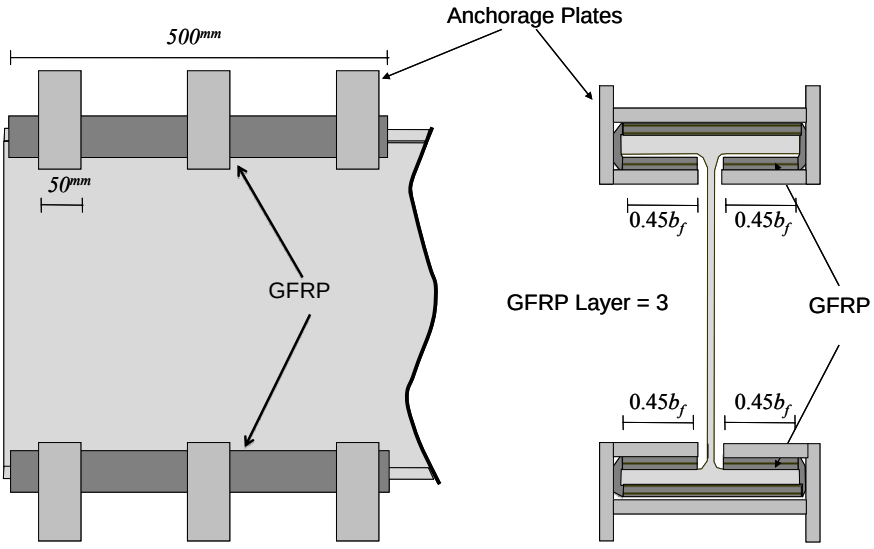

Figure 3.24. GFRP Layout of HE500AA GFRP2 Beam

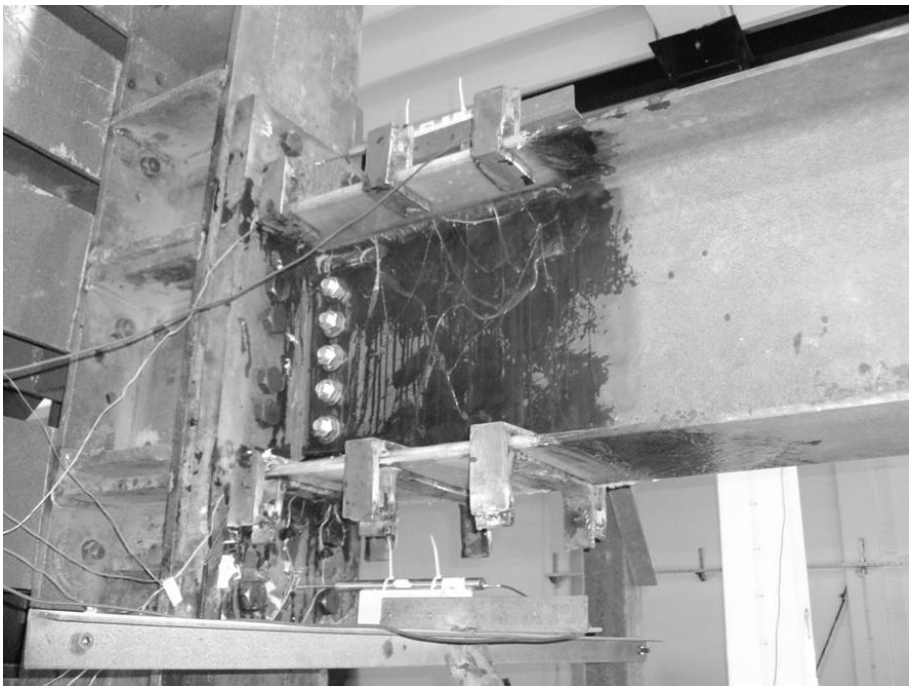

Figure 3.25. HE500AA GFRP2 Beam

CHAPTER 4

EXPERIMENTAL RESULTS

4.1. Test Observations

4.1.1. HE400AA Bare Beam

The loading protocol is shown in Figure 4.1. Due to the rigid body rotation at the beam support frame connection mentioned in the previous chapter, the load cycles applied to the bare beam specimen is not totally compatible with AISC (2005b) loading protocol. In Figure 4.2 load versus beam rotation at welded haunch (WH) tip is shown. Positive rotation implies the top flange is in compression and negative rotation implies bottom flange is in compression.

As can be seen from Figure 4.2 the rotations of 0.00375, 0.005, 0.0075 and 0.011 radians were elastic. Local buckling was not observed in rotations of 0.015 and 0.02 radians. A minor local buckling at the bottom flange was observed in the first cycle of 0.024 rad of rotation. At the second cycle of the 0.024 rad of rotation, top flange at the plastic hinge region buckled slightly as well. At the first cycle of 0.034 rad of rotation the top flange inside the welded haunch region (see Figure 4.3) and bottom flange at the plastic hinge region (see Figure 4.4) severely buckled. In the second cycle of the 0.034 rad of rotation, the load started to drop, and it was decided to stop the test.

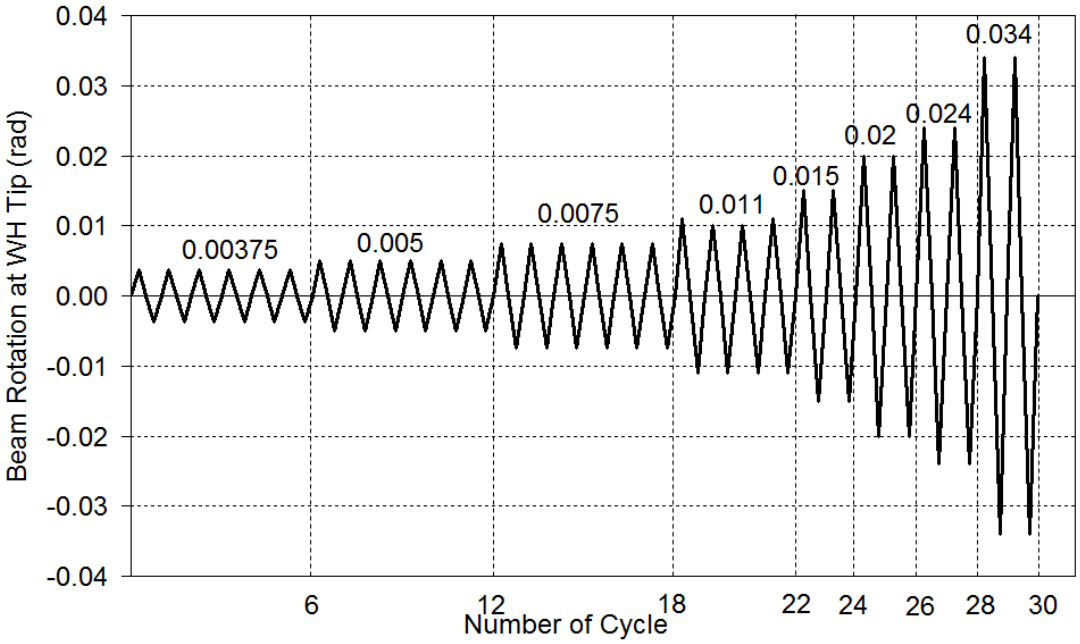

Figure 4.1. HE400AA Bare Beam Loading Protocol

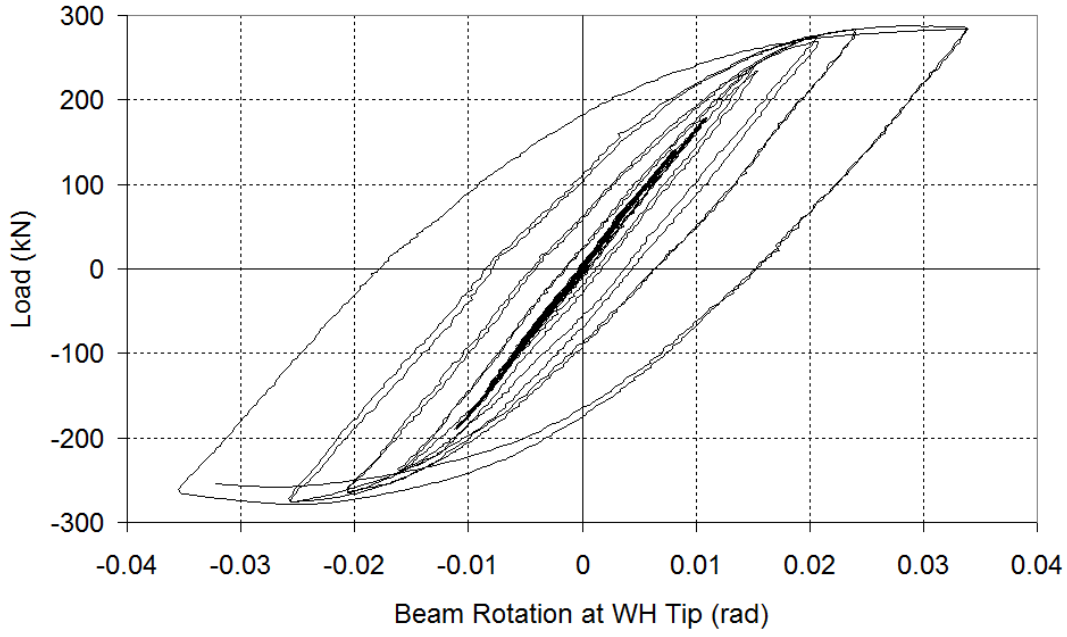

Figure 4.2. HE400AA Bare Beam Load versus Beam Rotation at WH Tip

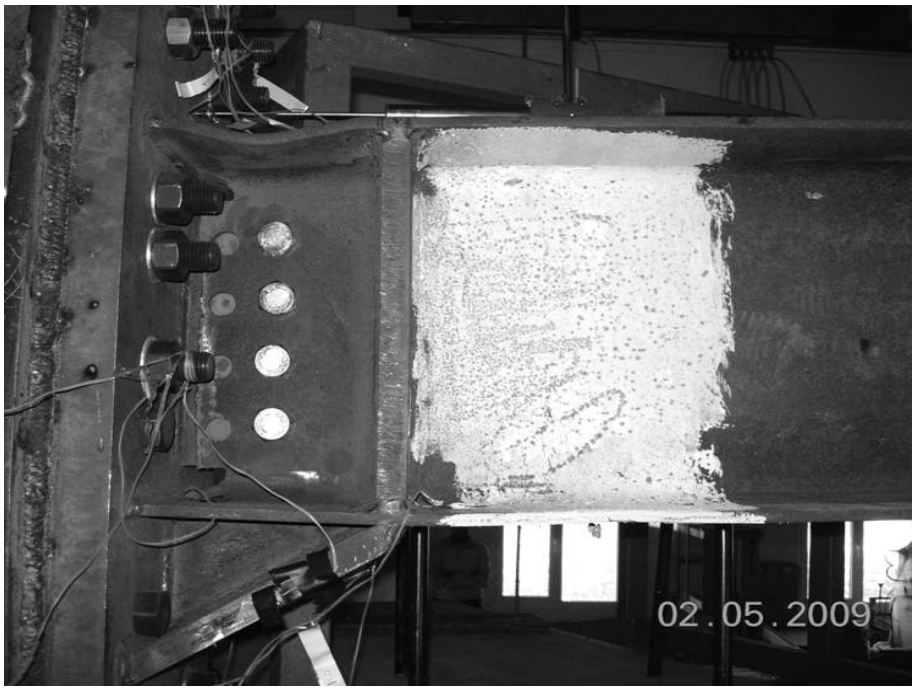

Figure 4.3. HE400AA Bare Beam Top Flange at 0.034 rad of Rotation

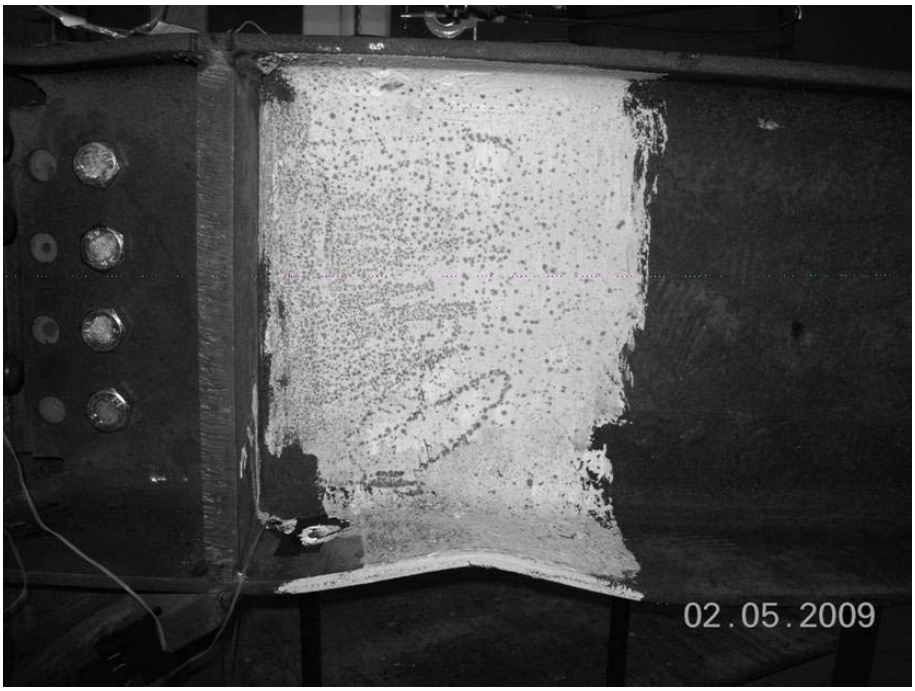

Figure 4.4. HE400AA Bare Beam Bottom Flange at 0.034 rad of Rotation

4.1.2. HE400AA GFRP1 Beam

The HE400AA GFRP1 beam was loaded following the loading protocol in Figure 4.5. Due to the rigid body rotation at the beam support frame connection mentioned in the previous chapter, the load cycles applied to the GFRP1 beam specimen is not totally compatible with AISC (2005b) loading protocol. In addition, some differences between positive and negative load cycles of loading protocol have happened in this experiment because of the same problem. In Figure 4.6 load versus beam rotation at WH tip is shown. Positive rotation implies the top flange is in compression and negative rotation implies bottom flange is in compression.

HE400AA GFRP1 beam exhibited elastic behavior in the 0.00375, 0.005, 0.0075 and 0.011 radians rotations. Sounds coming from the GFRP were observed when the rotations reached 0.0075 radians and higher. These sounds indicate that debonding occurred between GFRP and steel in a gradual manner. Local buckling was not observed in rotations of 0.011 and 0.016 radians. For the 0.021 rad positive rotation and 0.017 rad negative rotation the sounds coming from GFRP continued and no local buckling was observed. Severe local buckling was observed at the top flange inside the welded haunch region at a rotation of 0.033 rad as seen in Figure 4.7. Local buckling at the bottom flange was also noticed in this cycle (0.028 rad negative rotation) at the plastic hinge region as seen in Figure 4.8, however this was not as severe as the one in the top flange. Local buckles continued to be more severe at 0.044 rad of positive rotation in the WH region as seen in Figure 4.9 and the sounds coming from test setup started to become more intensified. On the grounds that the conditions are not available, the test was stopped at towards the end of the first cycle at 0.044 rad of rotation.

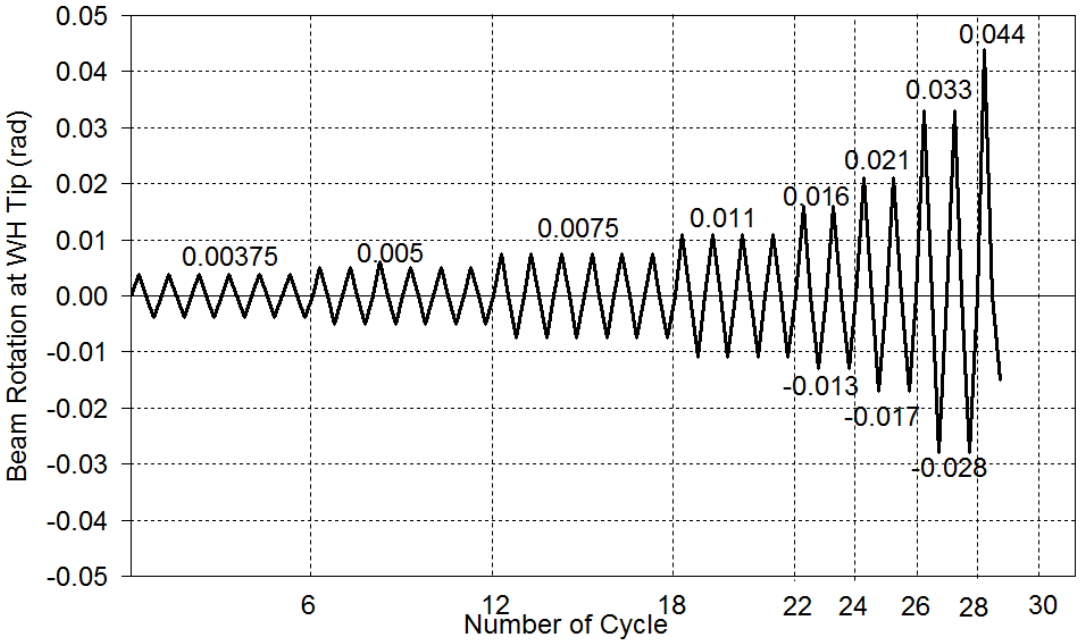

Figure 4.5. HE400AA GFRP1 Beam Loading Protocol

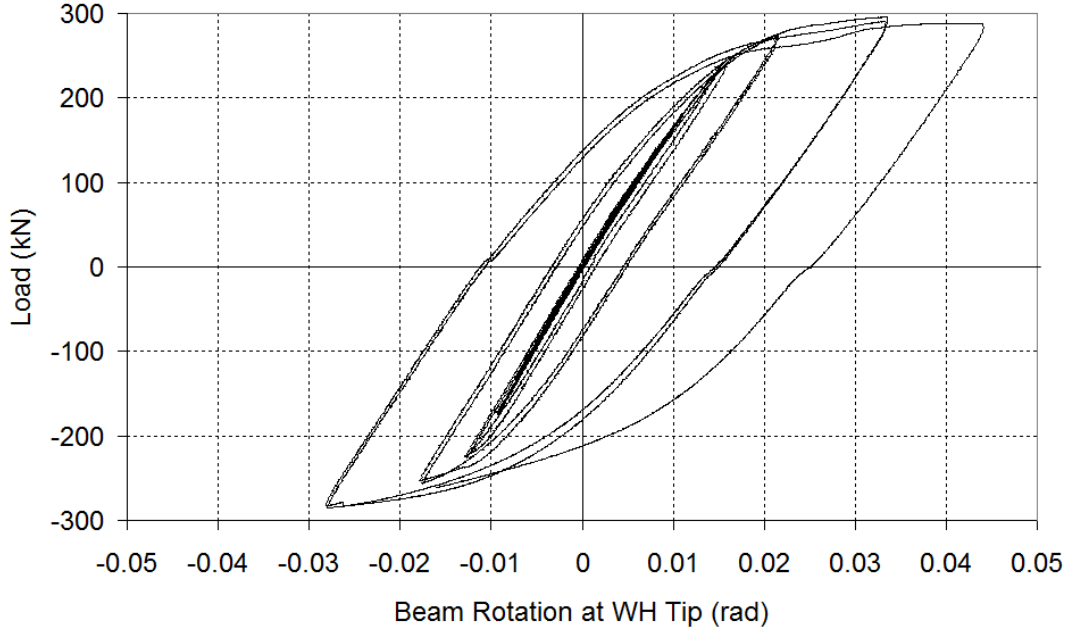

Figure 4.6. HE400AA GFRP1 Beam Load versus Beam Rotation at WH Tip

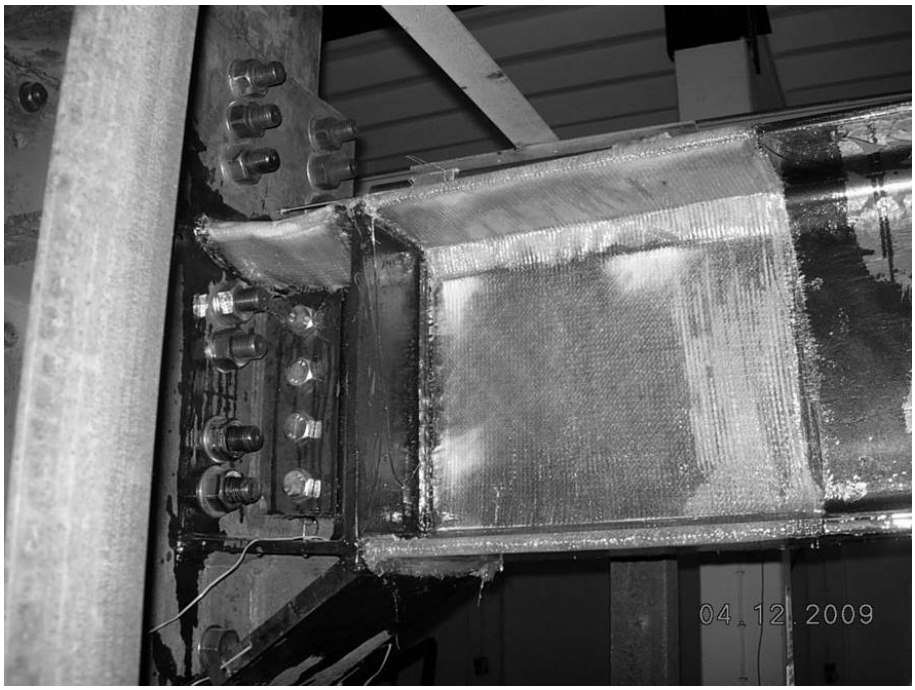

Figure 4.7. HE400AA GFRP1 Beam Top Flange at 0.033 rad of Rotation

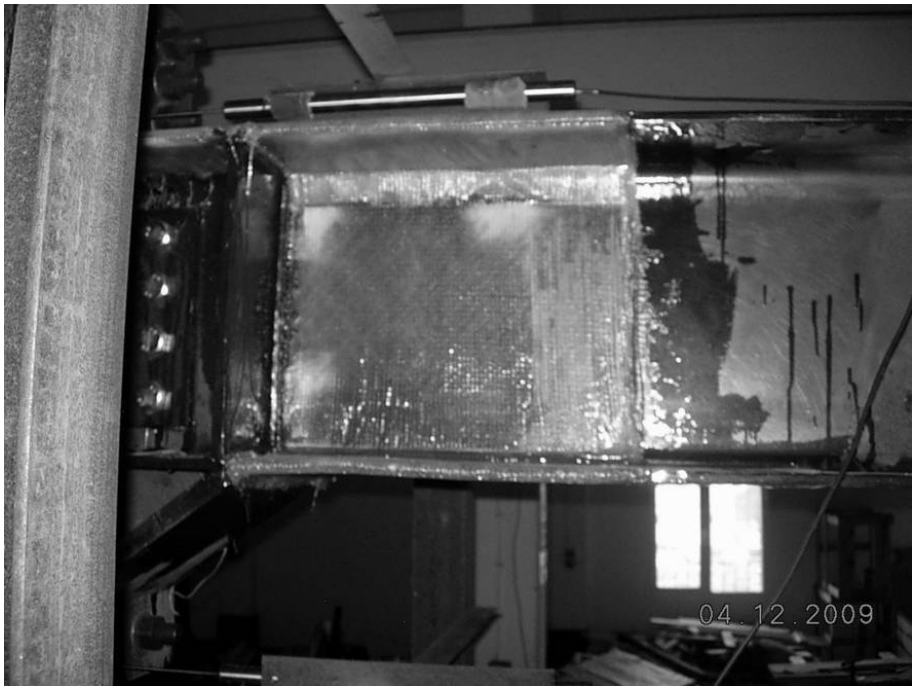

Figure 4.8. HE400AA GFRP1 Beam Bottom Flange at 0.028 rad of Rotation

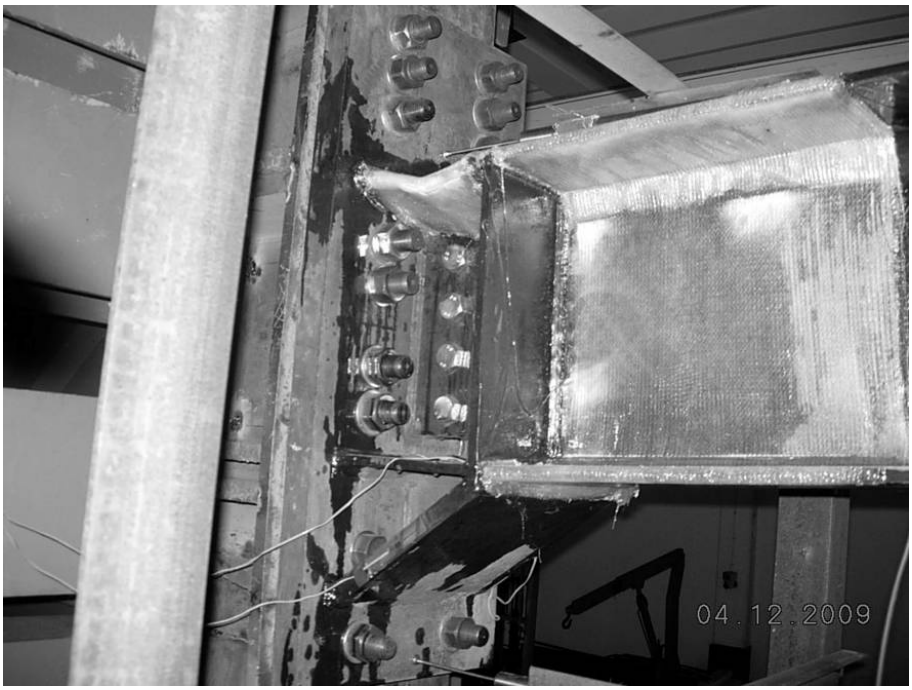

Figure 4.9. HE400AA GFRP1 Beam Top Flange at 0.044 rad of Rotation

4.1.3. HE400AA GFRP2 Beam

The HE400AA GFRP2 beam was loaded following the loading protocol in Figure 4.10. Due to the rigid body rotation at the beam support frame connection mentioned in the previous chapter, the load cycles applied to the GFRP2 beam specimen is not totally compatible with AISC (2005b) loading protocol. Load versus beam rotation at WH tip is shown in Figure 4.11. Positive rotation implies the top flange is in compression and negative rotation implies bottom flange is in compression.

In the HE400AA GFRP2 experiment beam exhibited elastic behavior in the 0.00375, 0.005, 0.008 and 0.012 radians rotation cycles. Sounds coming from the GFRP were observed when the rotations reached 0.0012 radians and beyond. Local buckling was not observed in rotations of 0.012 and 0.017 radians. Even though in the first cycle of 0.023 rad rotation local buckling was not observed, buckling initiated in the second cycle of the same rotation in the top flange WH region when top flange was in compression. However, no buckling was observed in the bottom flange in the second cycle of the 0.023 rad negative rotation. During the first cycle of 0.034 rad

rotation top flange were severely buckled and the severe local buckling of the top flange inside the WH can be seen in Figure 4.12. In this cycle, the bottom flange also buckled when this flange was under compression (see Figure 4.13). In the second cycle of 0.034 rad rotation both the top flange and bottom flange local buckles continued increasingly. In the first cycle of 0.046 rad rotation, the severity of the top flange buckles increased and finally top flange was fractured near the column face in this cycle when the bottom flange was under compression (see Figure 4.14).

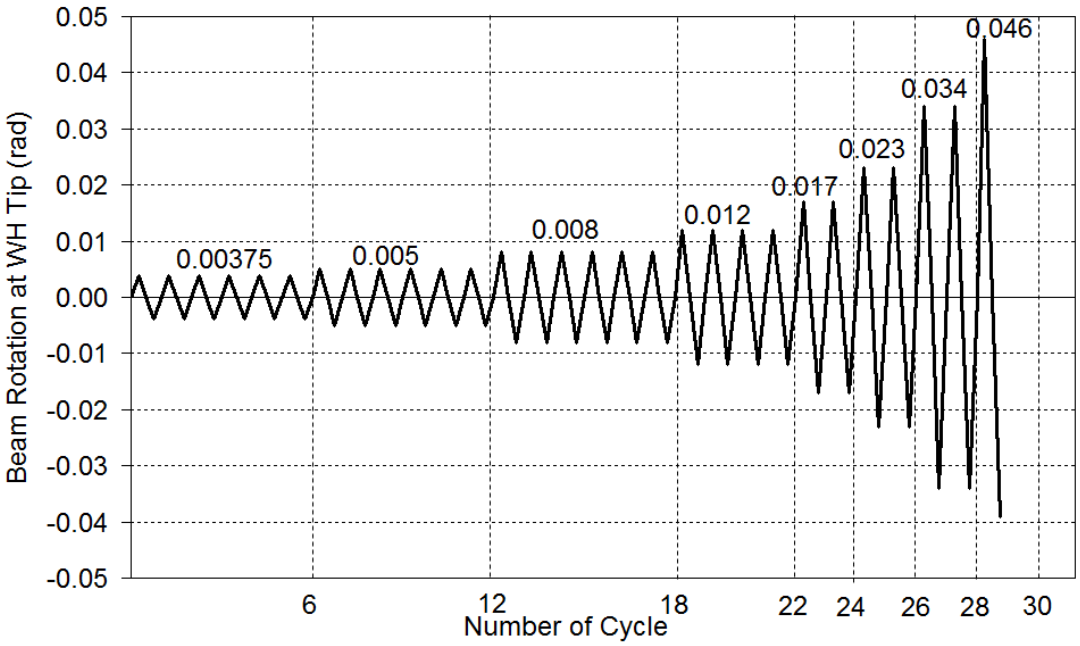

Figure 4.10. HE400AA GFRP2 Beam Loading Protocol

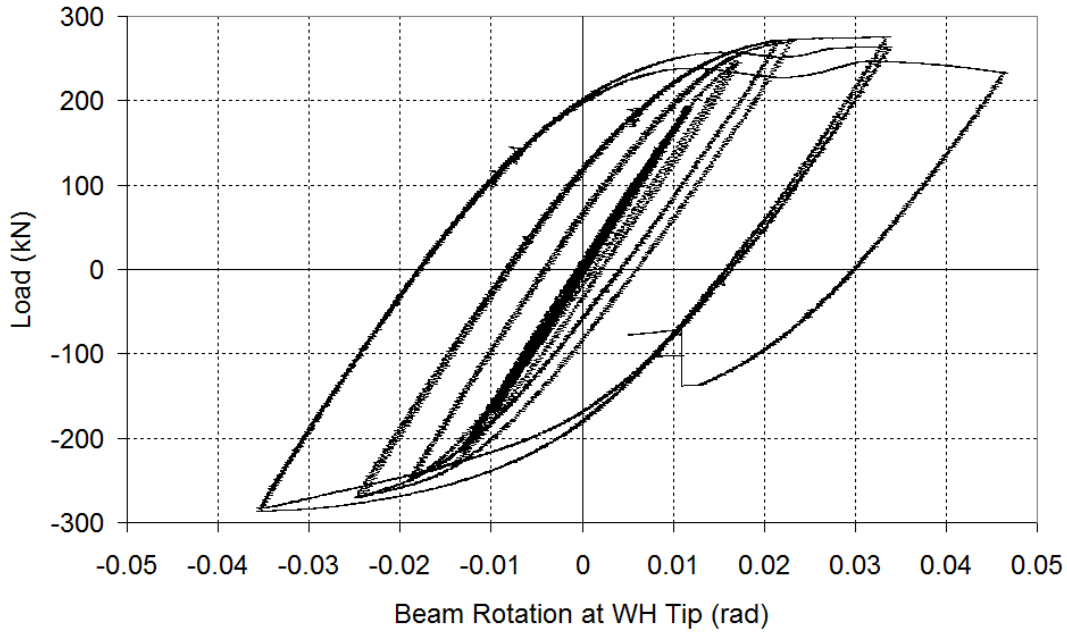

Figure 4.11. HE400AA GFRP2 Beam Load versus Beam Rotation at WH Tip

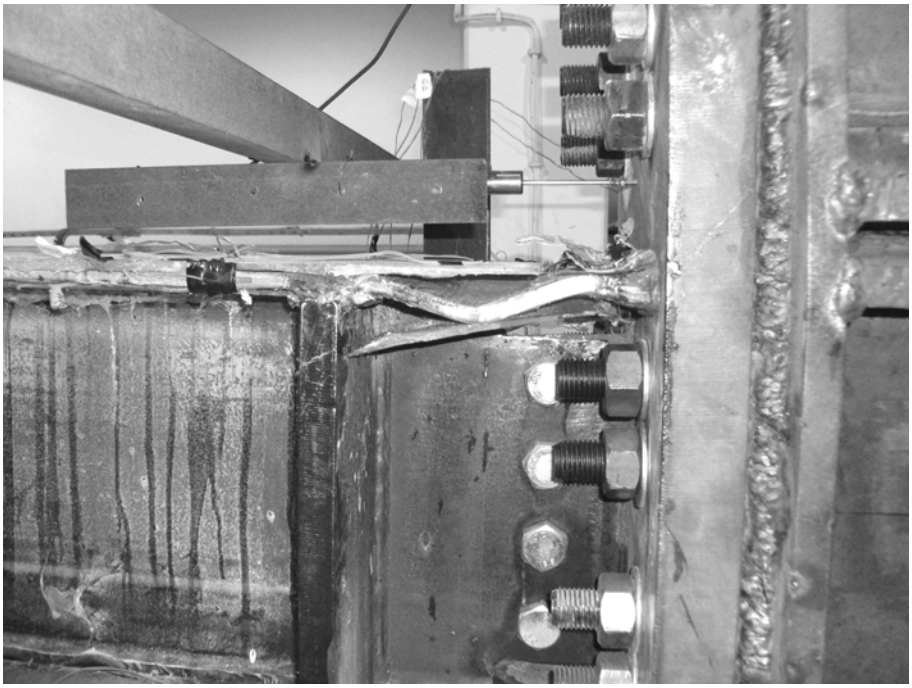

Figure 4.12. HE400AA GFRP2 Beam Top Flange at 0.034 rad of Rotation

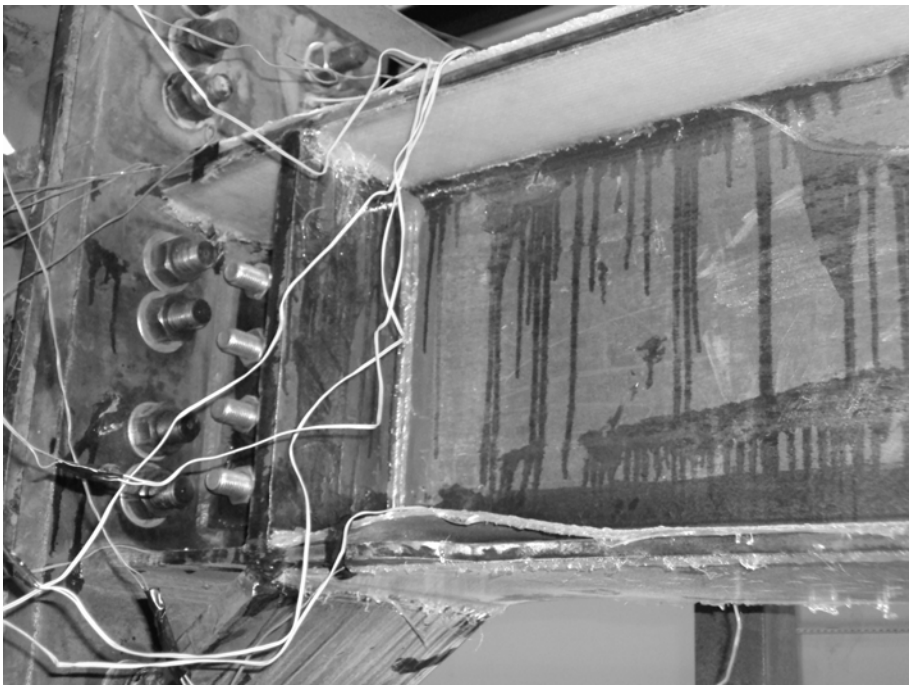

Figure 4.13. HE400AA GFRP2 Beam Bottom Flange at 0.034 rad of Rotation

Figure 4.14. HE400AA GFRP2 Beam Top Flange Fracture at 0.046 rad of Rotation

4.1.4. HE400AA GFRP3 Beam

The HE400AA GFRP3 beam was loaded following the loading protocol in Figure 4.15. Due to the rigid body rotation at the beam support frame connection mentioned in the previous chapter, the load cycles applied to the GFRP3 beam specimen is not totally compatible with AISC (2005b) loading protocol. Load versus beam rotation at WH tip is shown in Figure 4.16. Positive rotation implies the top flange is in compression and negative rotation implies bottom flange is in compression.

HE400AA GFRP3 beam exhibited elastic behavior in the 0.00375, 0.005, 0.008 and 0.011 radians rotations. Sounds coming from the GFRP were observed when the rotations reached 0.011 radians and beyond. Local buckling was not observed in rotations of 0.011 and 0.016 radians. A minor local top flange buckling inside the WH region was observed in the second cycle of 0.022 rad positive rotation while there was no buckling in the bottom flange during this cycle when this flange was under compression. During the first cycle of 0.033 rad rotation, top flange was severely buckled and debonding occurred inside the WH region. The severe local buckling of the top flange inside the WH can be seen in Figure 4.17. In this cycle the bottom flange also buckled during the 0.033 rad negative rotation and the top flange buckling was straighten out. In the second cycle of 0.033 rad positive rotation local buckling in the top flange continued to increase and local buckling in the bottom flange was in a moderate manner while debonding occurred in this flange as well. In the first cycle of 0.043 rad positive rotation top flange buckled inside the WH region in a very severe manner (see Figure 4.18) and also the bottom flange buckling increased in the 0.043 rad negative rotation (see Figure 4.19). Even though the severity of top flange local buckling increased during the second cycle of 0.043 rad rotation, there was no fracture in the flange. In this cycle, the bottom flange buckled severely as well and all cycles were completed.

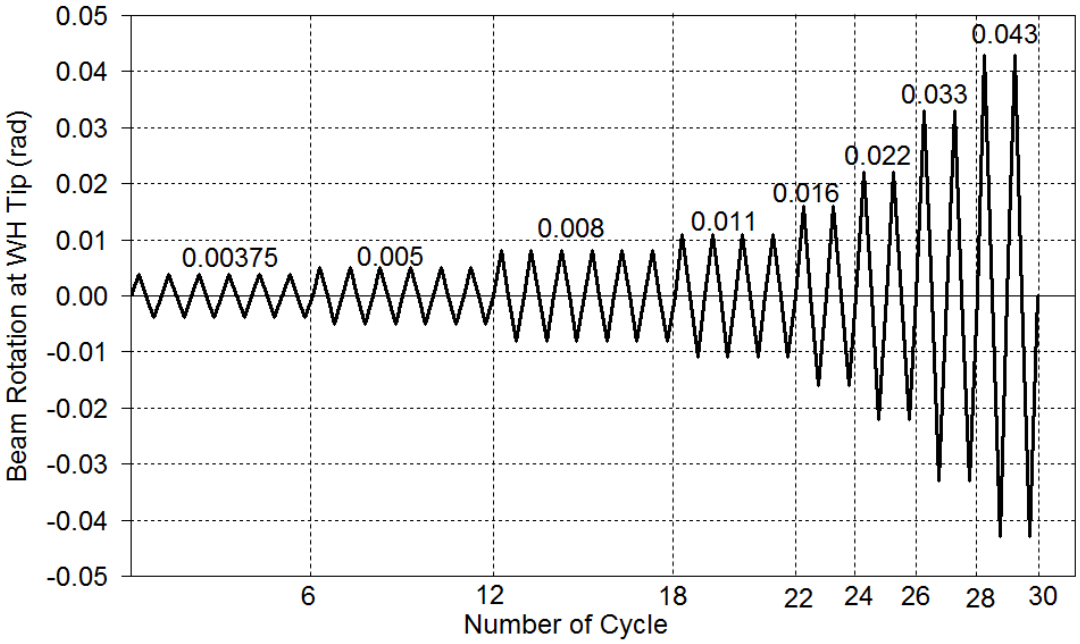

Figure 4.15. HE400AA GFRP3 Beam Loading Protocol

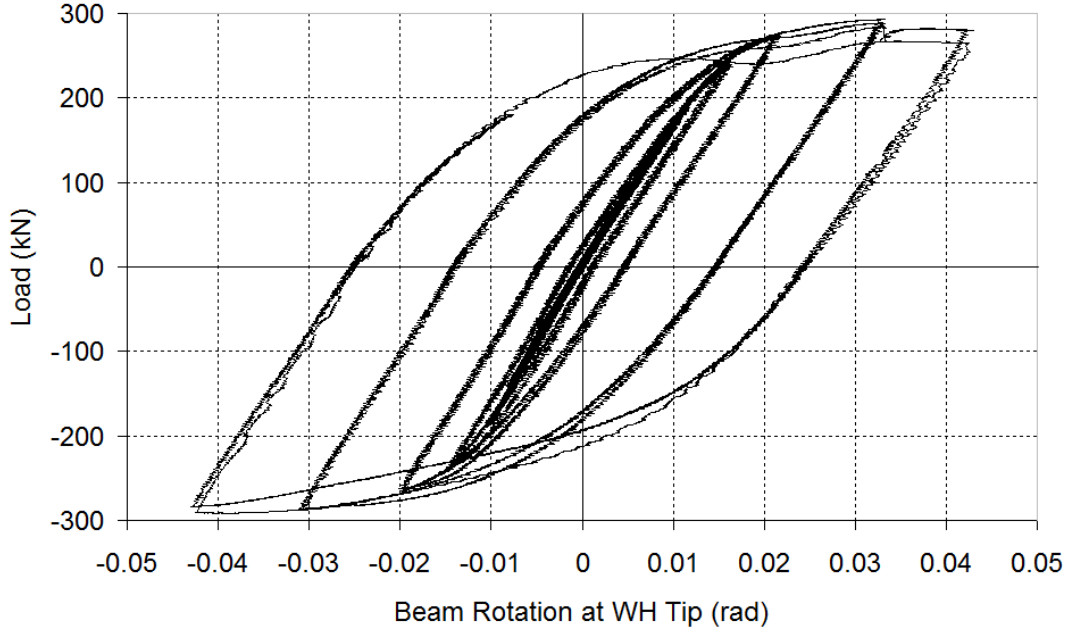

Figure 4.16. HE400AA GFRP3 Beam Load versus Beam Rotation at WH Tip

Figure 4.17. HE400AA GFRP3 Beam Top Flange at 0.033 rad of Rotation

Figure 4.18. HE400AA GFRP3 Beam Top Flange at 0.043 rad of Rotation

Figure 4.19. HE400AA GFRP3 Beam Bottom Flange at 0.043 rad of Rotation

4.1.5. HE500AA Bare Beam

The loading protocol of HE500AA bare beam is shown in Figure 4.20. Due to the rigid body rotation at the beam support frame connection mentioned in the previous chapter, the load cycles applied to the bare beam specimen is not totally compatible with AISC (2005b) loading protocol. In Figure 4.21 load versus beam fixed-end rotation is shown. Positive rotation implies the top flange is in compression and negative rotation implies bottom flange is in compression. The moment is calculated at the face of the column as required by AISC (2005b).

As can be seen from the Figure 4.21 the rotations of 0.00375, 0.006, 0.009 and 0.012 radians were elastic. Local buckling was not observed in the rotation of up to 0.012 rad. A minor local buckling at the bottom flange was observed in the first negative cycle 0.017 rad of rotation (see Figure 4.22). At the second cycle of the 0.017 rad of rotation top flange also buckled at the plastic hinge region slightly. During the first cycle of 0.022 rad rotation, top flange was buckled in a pronounced manner when this flange was under compression as well as the bottom flange buckled in the same way when this flange was under compression. In the beginning of the first

cycle of 0.033 rad rotation the actuator was stopped due to the oil problem in the pump. After a ten-minute pause the test continued. During the first cycle of 0.033 rad positive rotation severe top flange local buckling was observed (see Figure 4.23) while the local buckling in the bottom flange was more pronounced in this cycle of negative rotation. In the second cycle of 0.033 rad rotation both top flange and bottom flange continued to buckle severely. In the first cycle of 0.042 rad rotation top flange buckled in a very severe manner when it was under compression (see Figure 4.24), while bottom flange also buckled very severely in this cycle of negative rotation (see Figure 4.25). During the second cycle of 0.042 rad positive rotation, load started to drop prominently and the experiment was stopped.

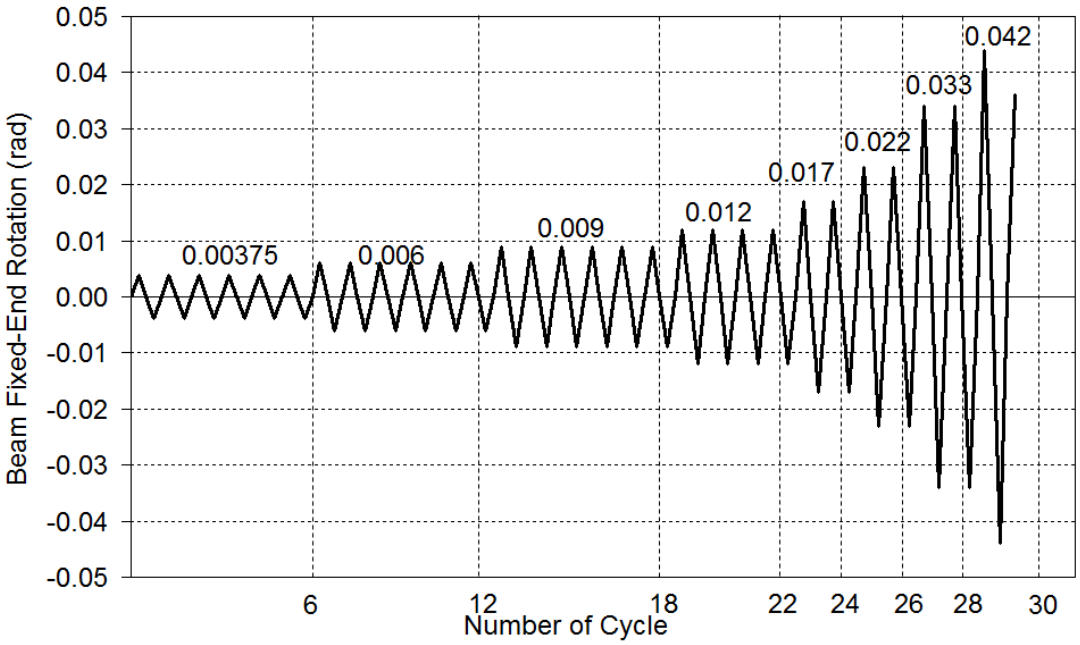

Figure 4.20. HE500AA Bare Beam Loading Protocol

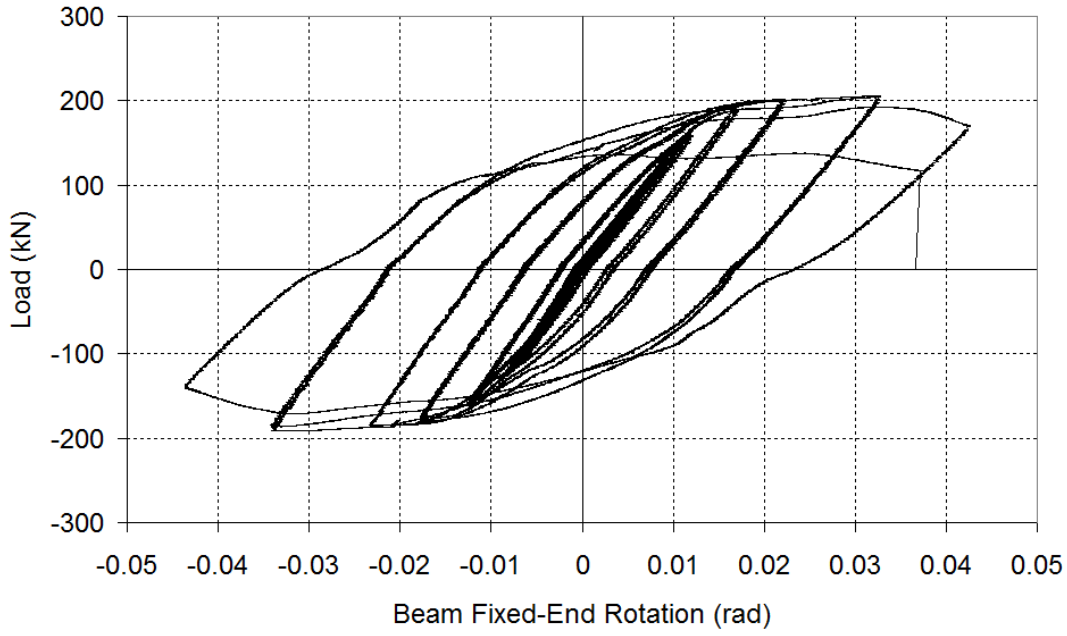

Figure 4.21. HE500AA Bare Beam Load versus Beam Fixed-End Rotation

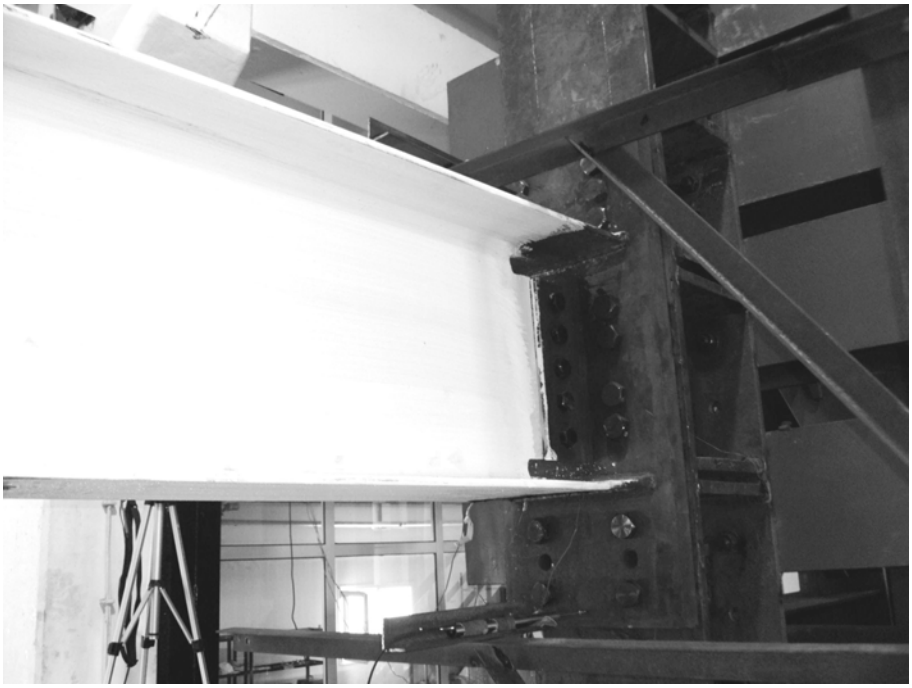

Figure 4.22. HE500AA Bare Beam Bottom Flange at 0.017 rad of Rotation

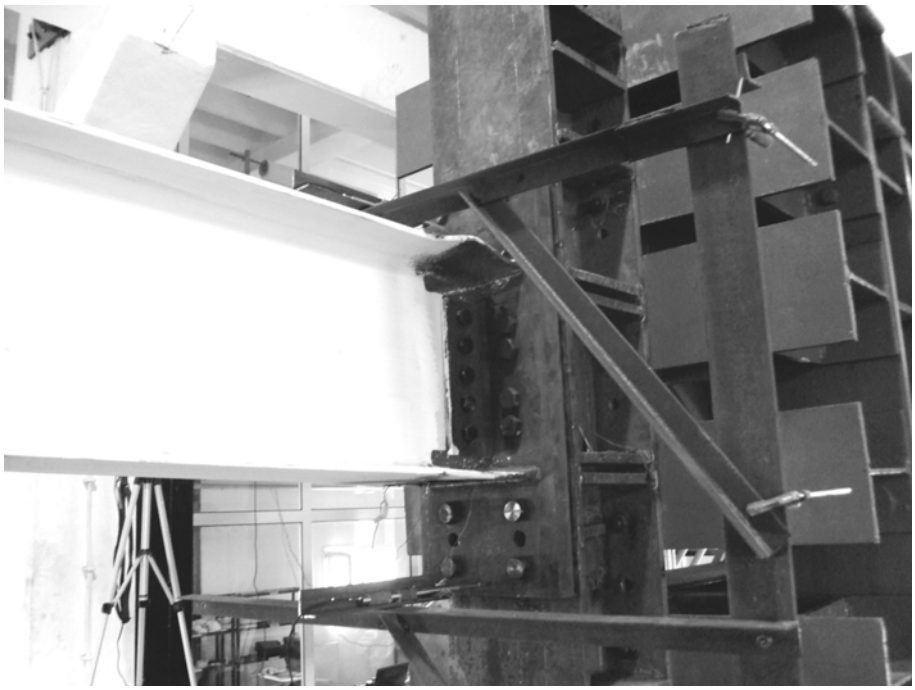

Figure 4.23. HE500AA Bare Beam Top Flange at 0.033 rad of Rotation

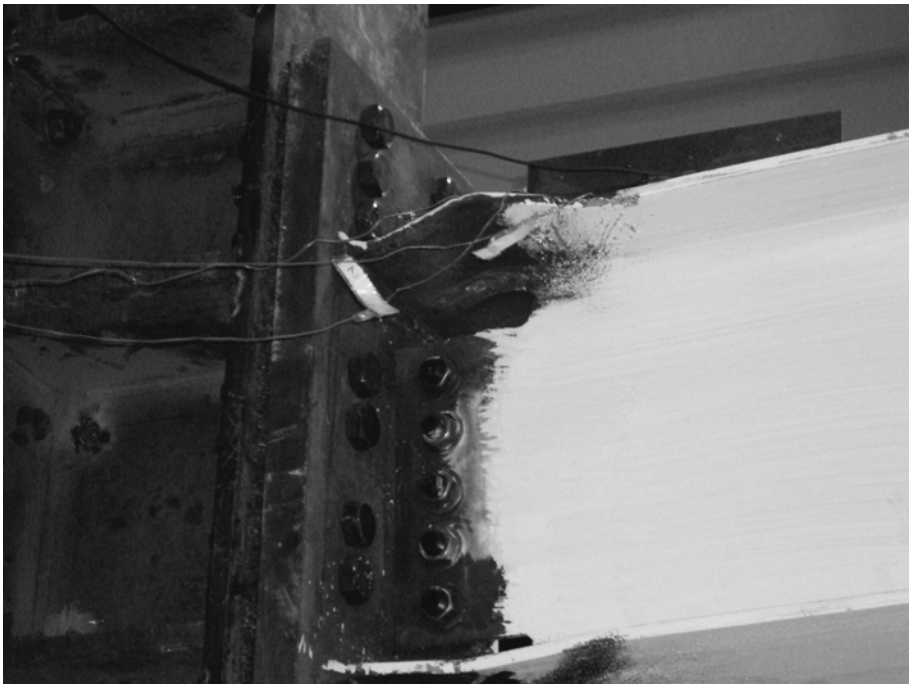

Figure 4.24. HE500AA Bare Beam Top Flange at 0.042 rad of Rotation

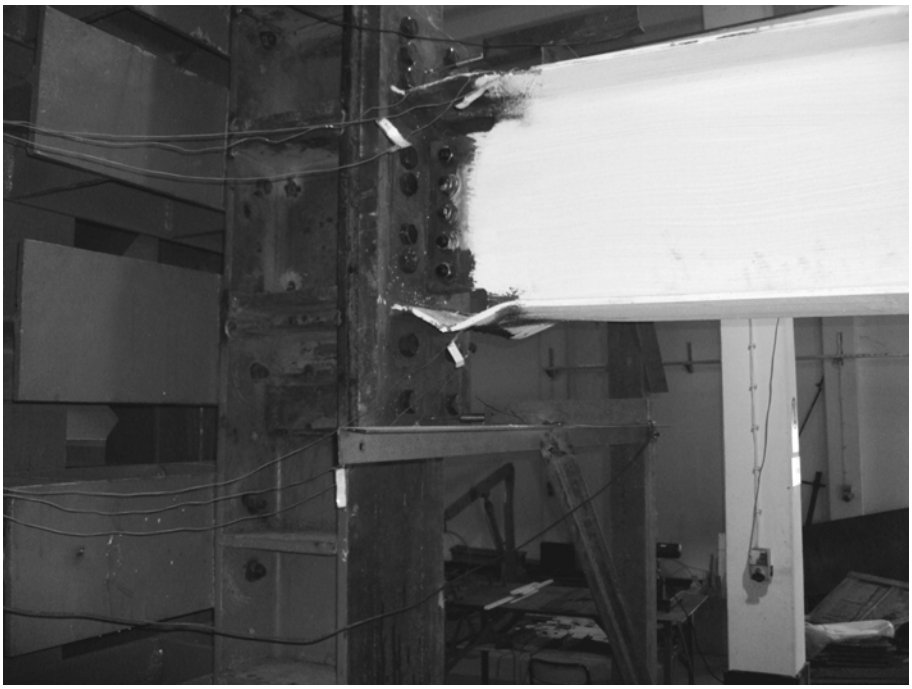

Figure 4.25. HE500AA Bare Beam Bottom Flange at 0.042 rad of Rotation

4.1.6. HE500AA GFRP1 Beam

The HE500AA GFRP1 beam was loaded following the loading protocol in Figure 4.26. Due to the rigid body rotation at the beam support frame connection mentioned in the previous chapter, the load cycles applied to the GFRP1 beam specimen is not totally compatible with AISC (2005b) loading protocol. In addition, some differences between positive and negative load cycles of loading protocol have happened in this experiment because of the same problem. In Figure 4.27 load versus beam fixed-end rotation is shown. Positive rotation implies the top flange is in compression and negative rotation implies bottom flange is in compression. The moment is calculated at the face of the column as required by AISC (2005b).

As can be seen from the figure the rotations of 0.00375, 0.005, 0.0075 and 0.013 radians were elastic. Local buckling was not observed in rotation of 0.013 rad. A minor local buckling at the top flange was observed in the first cycle of 0.017 rad of positive rotation and in this cycle of negative rotation bottom flange had a minor local buckling at the plastic hinge region as well. A slightly more local buckling in top flange was observed in the first cycle 0.022 rad of rotation while it was in the

same way in the bottom flange in this cycle of 0.025 rad negative rotation. In the second cycle, 0.022 rad positive and 0.025 rad negative of rotations the local buckles were pronouncedly both in the top flange and in the bottom flange. During the first cycle of 0.033 rad rotation, top flange local buckling was observed severely (see Figure 4.28) and debonding even fracture cracks in some locations occurred in GFRP materials. In this cycle of 0.036 rad negative rotation, bottom flange local buckling was in a severe manner as well. Debonding and fracture cracks in GFRP continued to occur in this cycle. During the second cycle of 0.033 rad positive and 0.036 rad negative rotations the severe local buckles in both top and bottom flanges continued and GFRP materials were completely independent from the flanges (see Figure 4.29). In the first cycle of 0.043 rad positive rotation top flange buckled in a very severe manner and web local buckling occurred (see Figure 4.30). In this cycle of 0.045 rad rotation bottom flange also buckled very severely and web local buckling continued to occur (see Figure 4.31). In the second cycle of 0.043 rad positive rotation both significantly severe top flange local buckling and web local buckling continued. Finally, top flange was fractured near the column face in this cycle of 0.045 rad negative rotation when bottom flange was under compression.

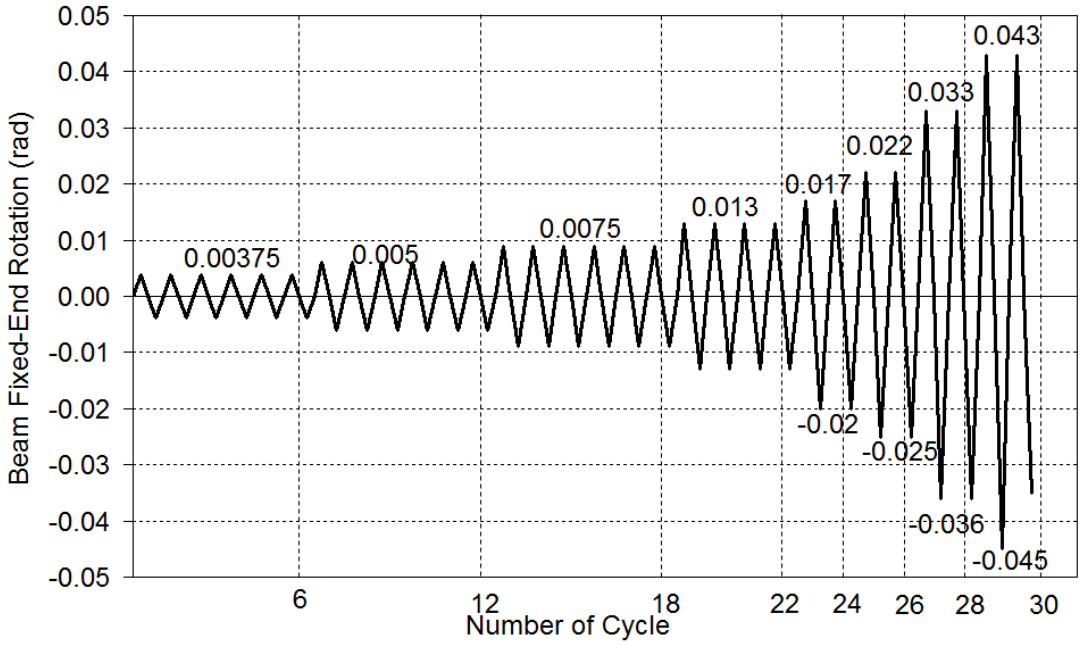

Figure 4.26. HE500AA GFRP1 Beam Loading Protocol

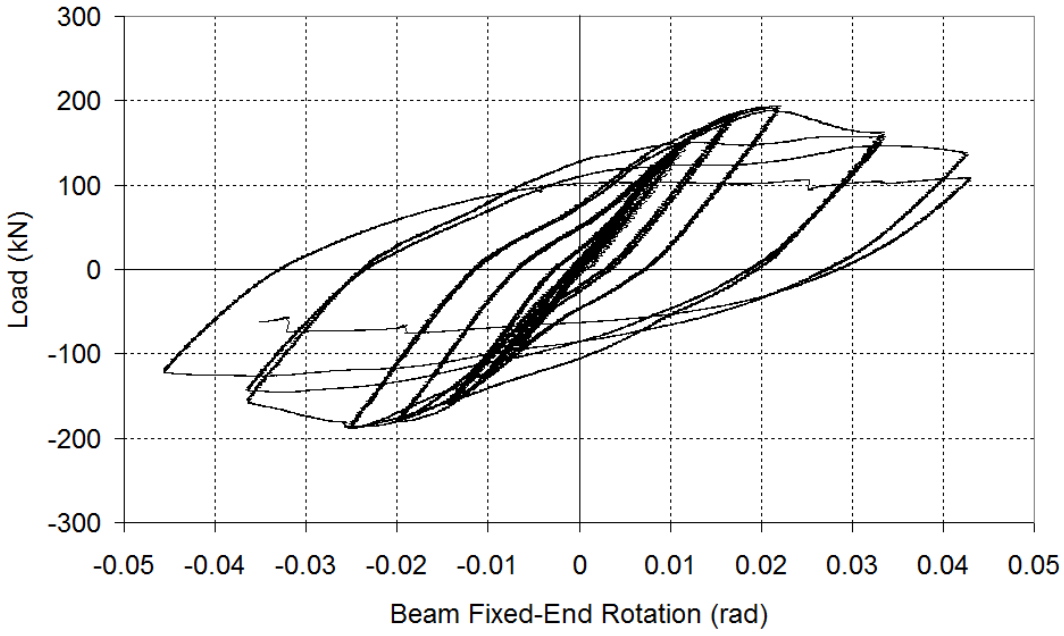

Figure 4.27. HE500AA GFRP1 Beam Load versus Beam Fixed-End Rotation

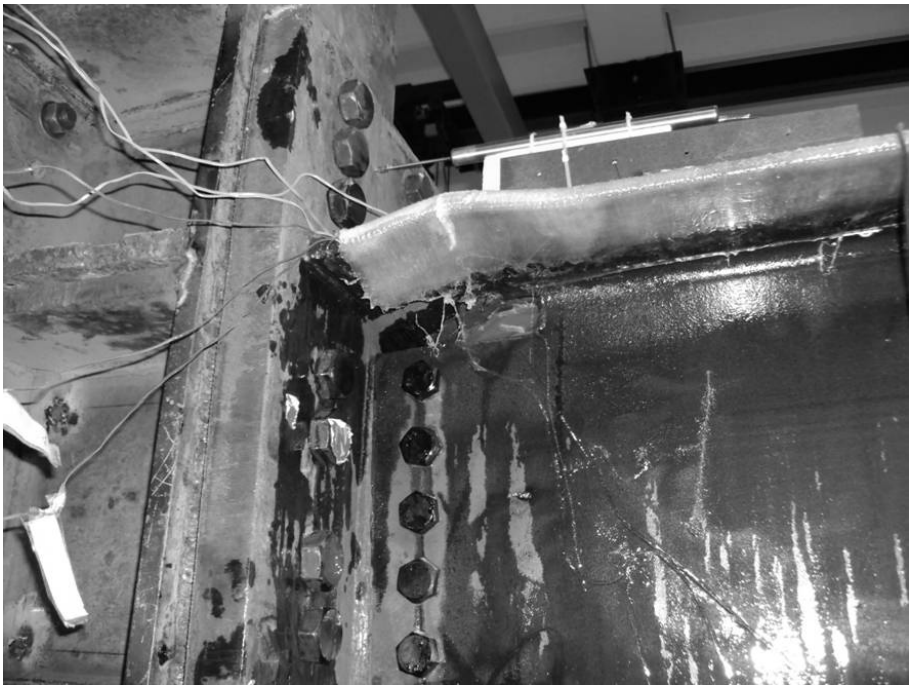

Figure 4.28. HE500AA GFRP1 Beam Top Flange at 0.033 rad of Rotation

Figure 4.29. HE500AA GFRP1 Beam GFRP Debonding at 0.036 rad of Rotation

Figure 4.30. HE500AA GFRP1 Beam Top Flange at 0.043 rad of Rotation

Figure 4.31. HE500AA GFRP1 Beam Bottom Flange at 0.045 rad of Rotation

4.1.7. HE500AA GFRP2 Beam

The HE500AA GFRP2 beam was loaded following the loading protocol in Figure 4.32. Due to the rigid body rotation at the beam support frame connection mentioned in the previous chapter, the load cycles applied to the GFRP2 beam specimen is not totally compatible with AISC (2005b) loading protocol. Load versus beam fixed-end rotation is shown in Figure 4.33. Positive rotation implies the top flange is in compression and negative rotation implies bottom flange is in compression. The moment is calculated at the face of the column as required by AISC (2005b).

As can be seen from the figure the rotations of 0.00375, 0.006, 0.009 and 0.012 radians were elastic. Local buckling was not observed in rotations of 0.012 and 0.017 radians. A minor local buckling at the top flange was observed in the first cycle of 0.023 rad of positive rotation and in this cycle of negative rotation, bottom flange had a minor local buckling as well, as seen in Figure 4.34. During the second cycle of 0.023 rad rotation buckling of both top and bottom flange increased slightly. In the first cycle of 0.034 rad rotation, the local buckles became more pronounced both for

the top and bottom flanges. In the second cycle of 0.034 rad rotation top flange buckled severely and the anchorage plates twisted (see Figure 4.35). Bottom flange buckled in a severe manner as well and weld of an anchorage plate on bottom flange fractured due to the great amount of twist. In the first cycle of 0.044 rad rotation, the top flange local buckling became very severe and GFRP fractured at the side of the top flange (see Figure 4.35). Bottom flange also buckled very severely in this cycle and GFRP fractures occurred at the side of bottom flange as well (see Figure 4.36). In the second cycle, the severity of buckles of both top and bottom flanges increased and GFRP fractures deepened. The web local buckling was on a minor level. Finally, this cycle was completed without any steel fractures.

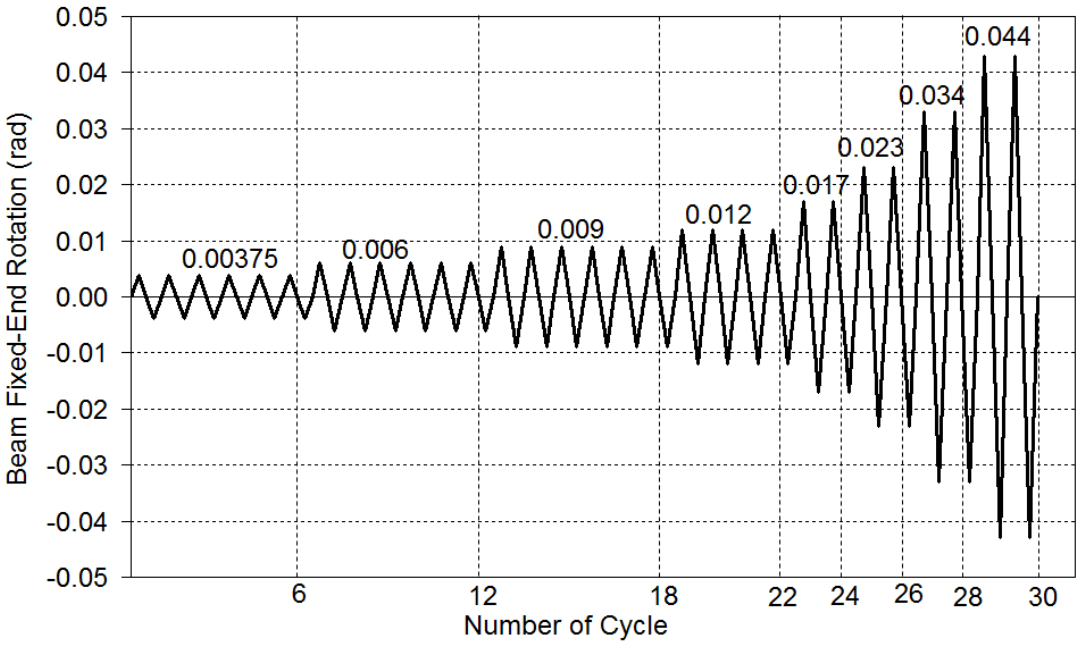

Figure 4.32. HE500AA GFRP2 Beam Loading Protocol

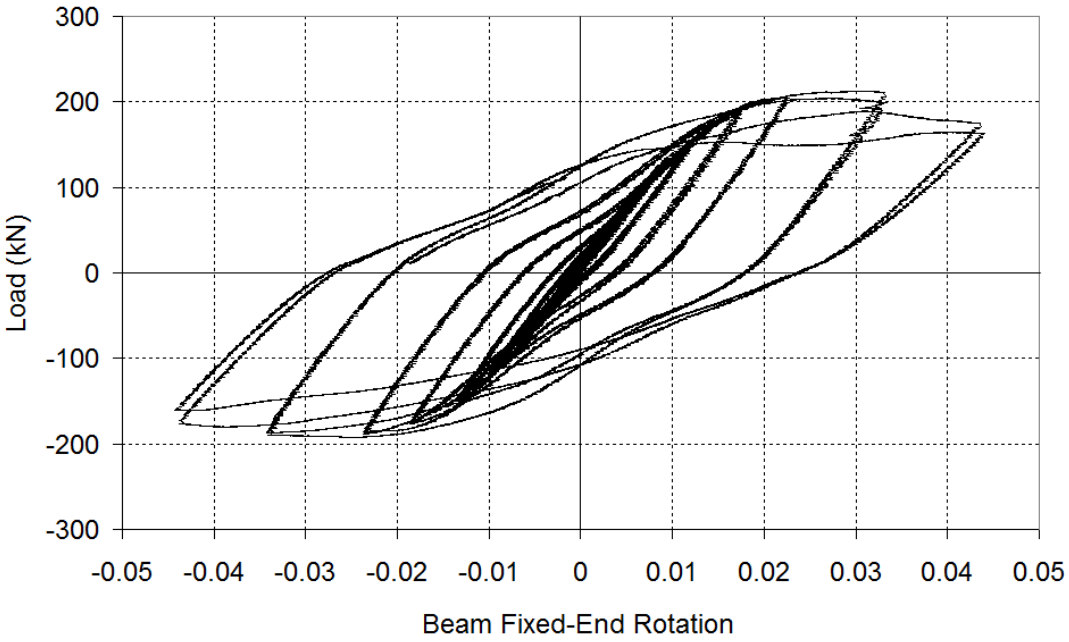

Figure 4.33. HE500AA GFRP2 Beam Load versus Beam Fixed-End Rotation

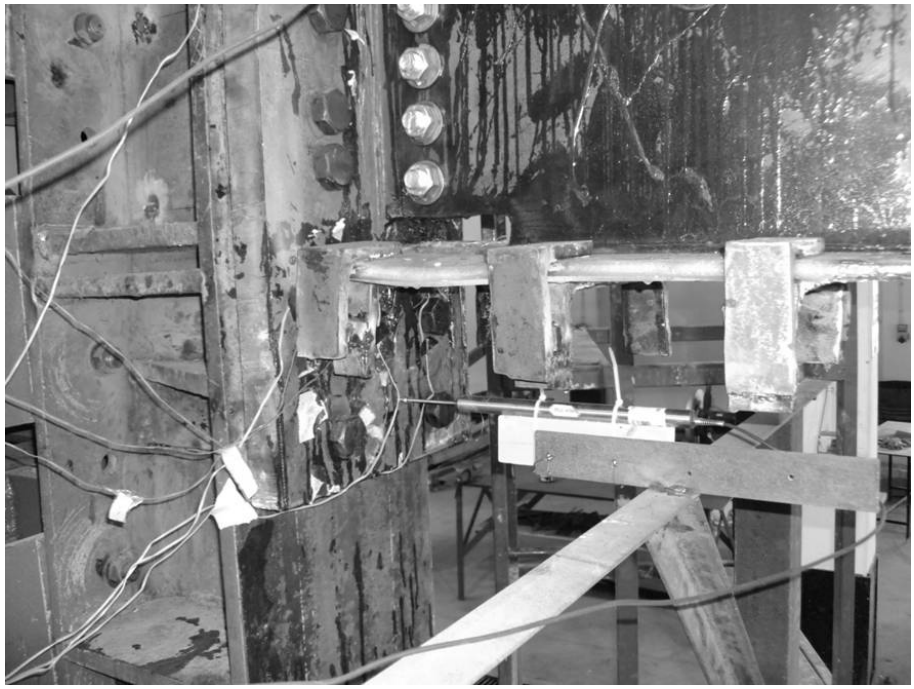

Figure 4.34. HE500AA GFRP2 Beam Bottom Flange at 0.023 rad of Rotation

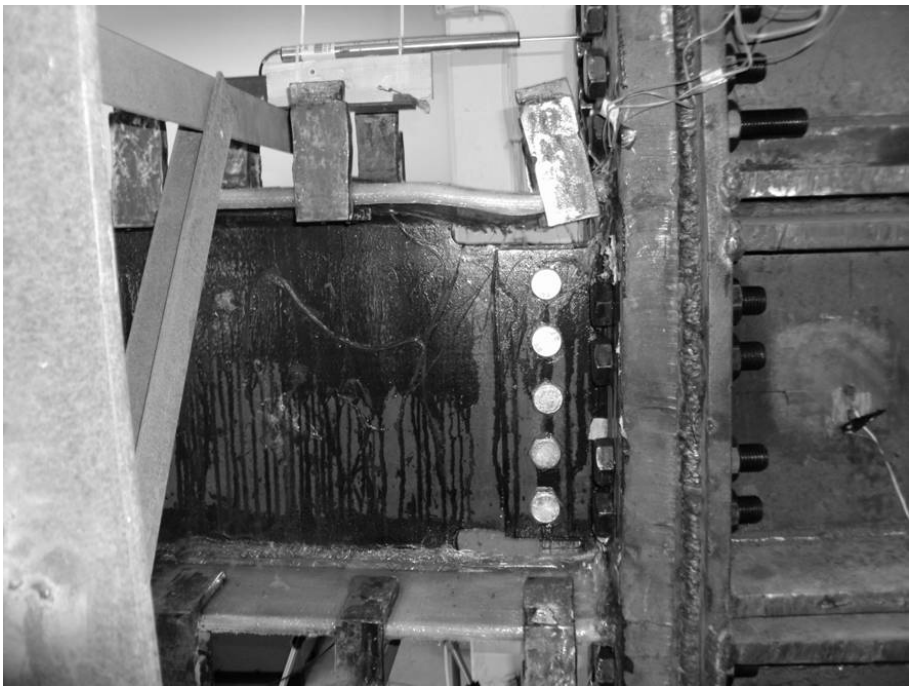

Figure 4.35. HE500AA GFRP2 Beam Top Flange at 0.034 rad of Rotation

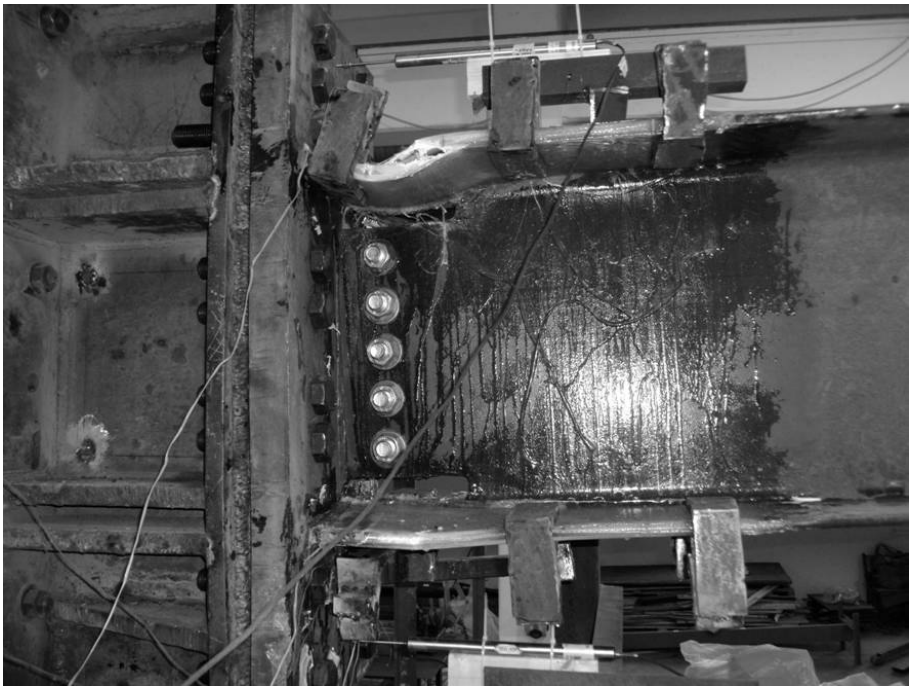

Figure 4.36. HE500AA GFRP2 Beam Top Flange at 0.044 rad of Rotation

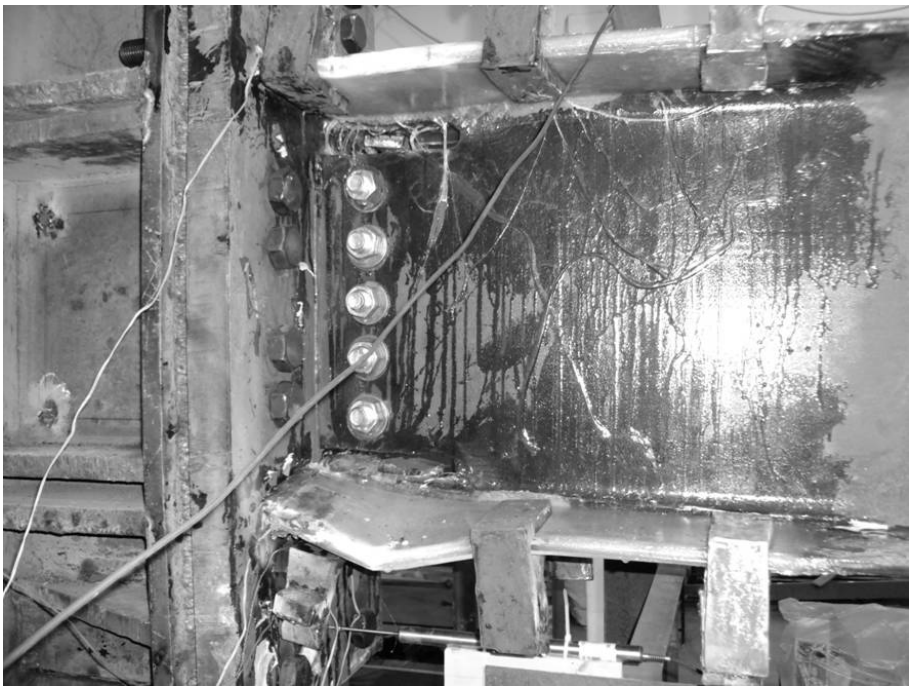

Figure 4.37. HE500AA GFRP2 Beam Bottom Flange at 0.044 rad of Rotation

4.2. Cyclic Behavior of Test Beams

4.2.1. Total Beam Rotations

HE400AA beams were tested with welded haunch (WH) modification while HE500AA beams with no modification. Total beam rotations at welded haunch tip for HE400AA specimens and total fixed-end beam rotations for the HE500AA specimens were calculated. Moment values obtained from experiments were calculated at the haunch tip and fixed-end for the HE400AA and HE500AA, respectively and divided by plastic moment of the sections (M_p) which was calculated according to the actual section properties considering the flange and web yield stress values separately. Due to the rigid body rotation at the beam support frame connection mentioned in the previous chapter, the load cycles applied to the bare beam specimen is not totally compatible with AISC (2005b) loading protocol. In addition, some differences between positive and negative load cycles of loading protocol have occurred in these experiments because of the same problem. Therefore, it should be taken into account for the M/M_p value comparisons of the specimens.

4.2.1.1. HE400AA Beams

HE400AA bare beam is the first specimen for HE400AA beams that have welded haunch modification. Total beam rotation versus M/M_p at welded haunch tip for HE400AA bare beam is shown in Figure 4.38. As seen in Figure 4.38 moment at welded haunch (WH) tip is above $0.8M_p$ in the second cycle of 0.034 rad rotation. This value is the required moment capacity for special moment frames (SMF) at 0.04 radian of rotation.

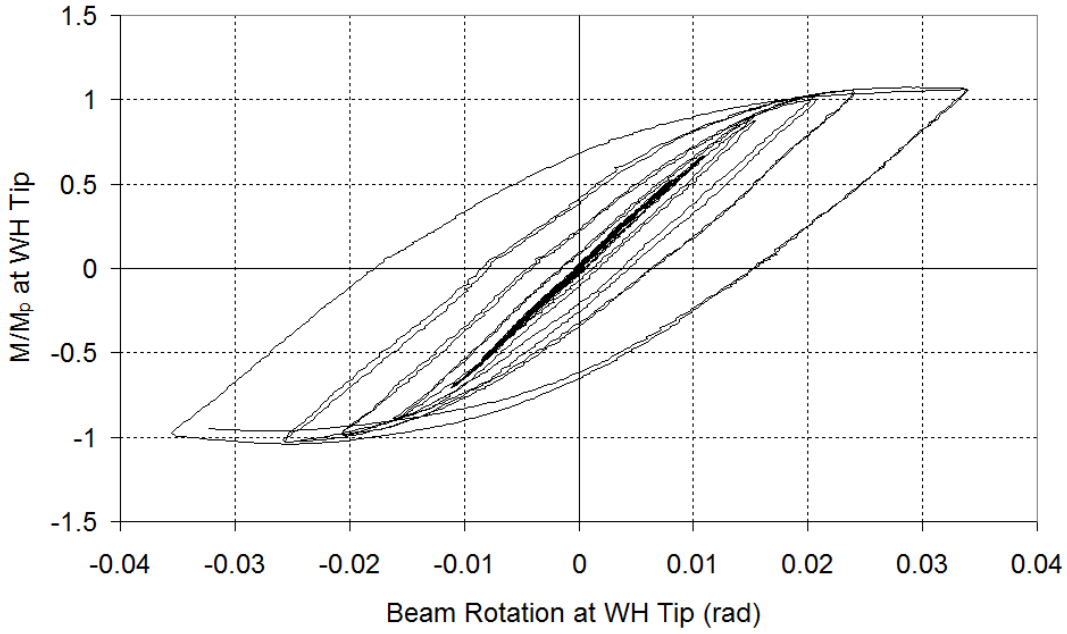

Figure 4.38. HE400AA Bare Beam Rotation at WH Tip vs. M/M_p

HE400AA GFRP1 beam has welded haunch modification and GFRP application. As mentioned in Chapter 3, GFRP materials were wrapped continuously around the plastic hinge region as three layers. Total beam rotation versus M/M_p at welded haunch tip for HE400AA GFRP1 beam is shown in Figure 4.39. In this experiment, positive and negative rotation values are in a pronounced manner different due to the fixed-end conditions, which explained previously. Moment value at the WH tip for HE400AA GFRP1 beam is above $0.8M_p$ when beam has 0.033 rad positive and 0.028 rad negative rotation. This value is the required moment capacity

for special moment frames (SMF) at 0.04 radian of rotation. However, the cycle that has 0.044 rad rotation at the WH tip could not be completed due to the stoppage of the test.

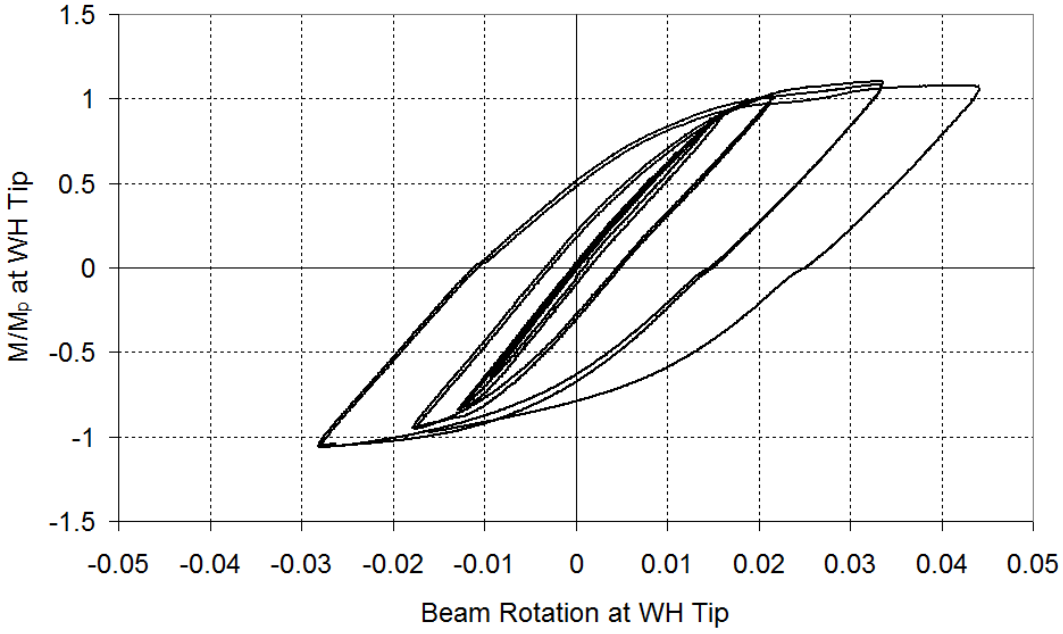

Figure 4.39. HE400AA GFRP1 Beam Rotation at WH Tip vs. M/M_p

HE400AA GFRP2 beam has welded haunch modification and five layers of GFRP application. GFRP materials were bonded only to flanges in a separate manner. Total beam rotation versus M/M_p at welded haunch tip for HE400AA GFRP2 beam is shown in Figure 4.40. As seen in Figure 4.40 moment at WH tip is above $0.8M_p$ value in the of 0.034 rad rotation at the WH tip. This value is the required moment capacity for special moment frames (SMF) at 0.04 radian of rotation. Because GFRP2 beam had failure in the 0.046 rad rotation at the WH tip, it did not manage to complete the last cycle.

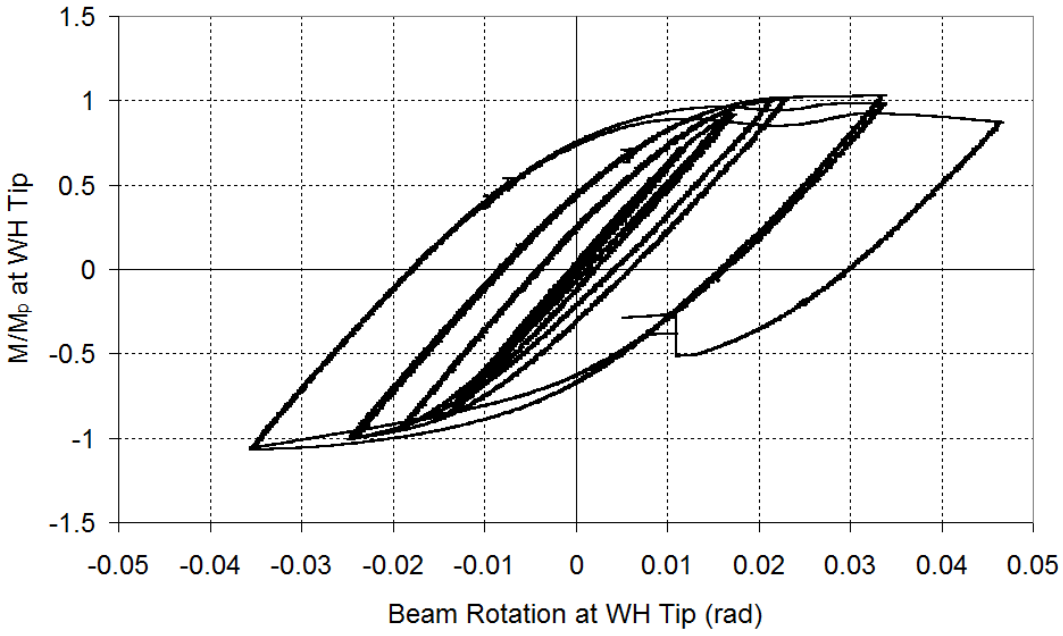

Figure 4.40. HE400AA GFRP2 Beam Rotation at WH Tip vs. M/M_p

HE400AA GFRP3 beam has welded haunch modification and three layers of GFRP application. GFRP layers were bonded to the flanges in a bending manner from outer parts of the flanges to the inner parts of them. Total beam rotation versus M/M_p at welded haunch tip for HE400AA GFRP3 beam is shown in Figure 4.41. GFRP3 beam completed all cycles and did not experience any failure. As seen in Figure 4.41 moment at WH tip is above $0.8M_p$ value after 0.043 rad rotation. This value is the required moment capacity for special moment frames (SMF) at 0.04 radian of rotation.

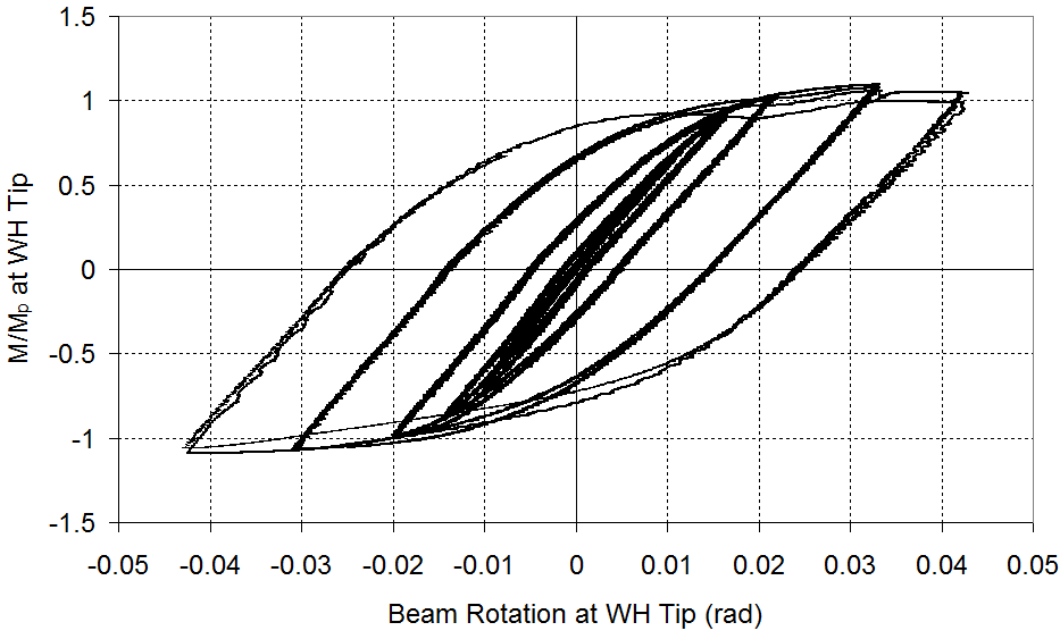

Figure 4.41. HE400AA GFRP3 Beam Rotation at WH Tip vs. M/M_p

4.2.1.2. HE500AA Beams

HE500AA bare beam is the first specimen for HE500AA beams with no modification. Total beam rotation versus M/M_p at the fixed-end for HE500AA bare beam is shown in Figure 4.42. $0.8M_p$ value in the abovementioned figure represents the required moment capacity for special moment frames (SMF) at 0.04 radian of rotation. Moment at the fixed-end is above $0.8M_p$ value in the cycle of 0.033 rad rotation as seen in Figure 4.42. Fixed-end moment in the first cycle of positive 0.042 rad rotation is above $0.8M_p$ value. However, strength degradation occurred due to the severity of local buckles in the flanges from the first negative cycle of 0.042 rad rotation on and the test was stopped in the second positive cycle of 0.042 rad rotation.

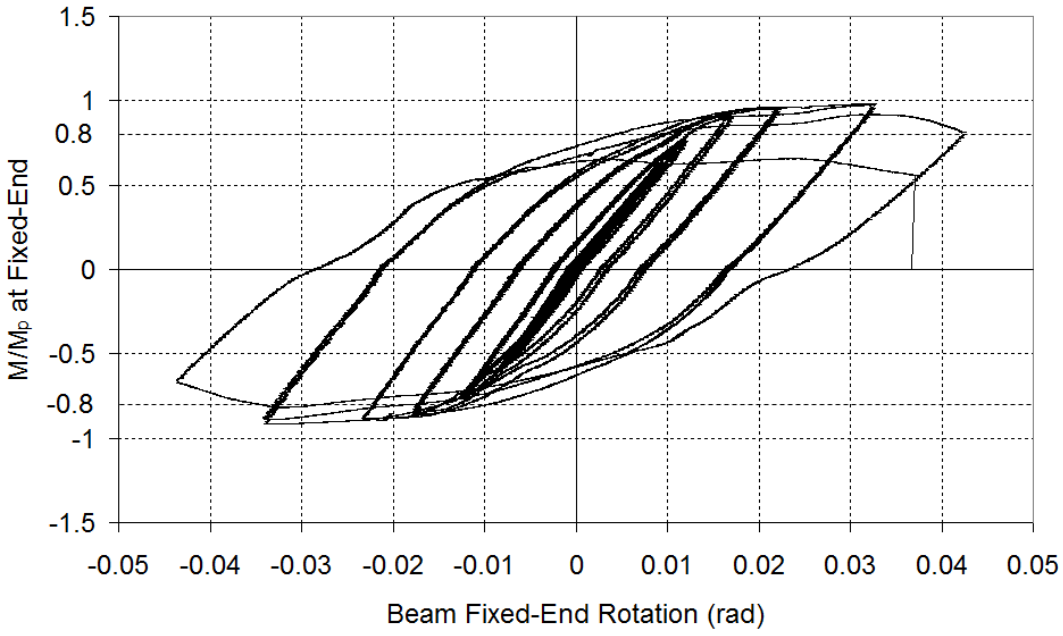

Figure 4.42. HE500AA Bare Beam Fixed-End Rotation vs. M/M_p

HE500AA GFRP1 beam has no modification and three layers of GFRP application. GFRP layers were bonded to the flanges in a bending manner from outer parts of the flanges to the inner parts of them. Total beam rotation versus M/M_p at the fixed-end for HE500AA GFRP1 beam is shown in Figure 4.43. $0.8M_p$ value in the abovementioned figure represents the required moment capacity for special moment frames (SMF) at 0.04 radian of rotation. HE500AA GFRP1 beam exhibited worse performance than HE500AA bare beam and strength degradation began so much earlier than expected. As mentioned previously this different situation should be taken into account for the GFRP beams comparisons. Moment at the fixed-end is above $0.8M_p$ value in the positive cycle of 0.022 rad rotation and in the negative cycle of 0.025 rad rotation as seen in Figure 4.43. However, fixed-end moment started to decrease rapidly from the first positive cycle of 0.033 rad rotation on and HE500AA GFRP1 beam failed in the second negative cycle of 0.045 rad rotation due to the severe strength degradation.

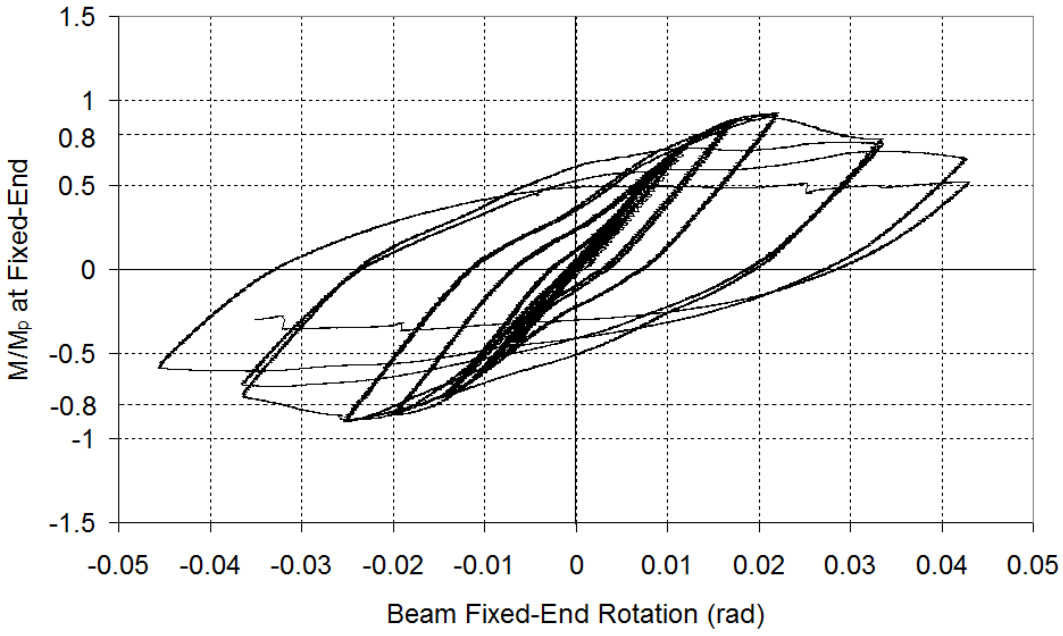

Figure 4.43. HE500AA GFRP1 Beam Fixed-End Rotation vs. M/M_p

HE500AA GFRP2 beam has no modification and three layers of GFRP application with anchorage plates, which applied to maintain delay in debonding of GFRP material. GFRP layers were bonded to the flanges in a bending manner from outer parts of the flanges to the inner parts of them. Total beam rotation versus M/M_p at the fixed-end for HE500AA GFRP2 beam is shown in Figure 4.44. $0.8M_p$ value in the abovementioned figure represents the required moment capacity for special moment frames (SMF) at 0.04 radian of rotation. Moment at the fixed-end is above $0.8M_p$ value in the cycle of 0.044 rad rotation as seen in Figure 4.44. HE500AA GFRP2 beam completed all cycles in loading protocol and GFRP application with the anchorage plates was very effective for providing larger inelastic response than HE500AA bare beam.

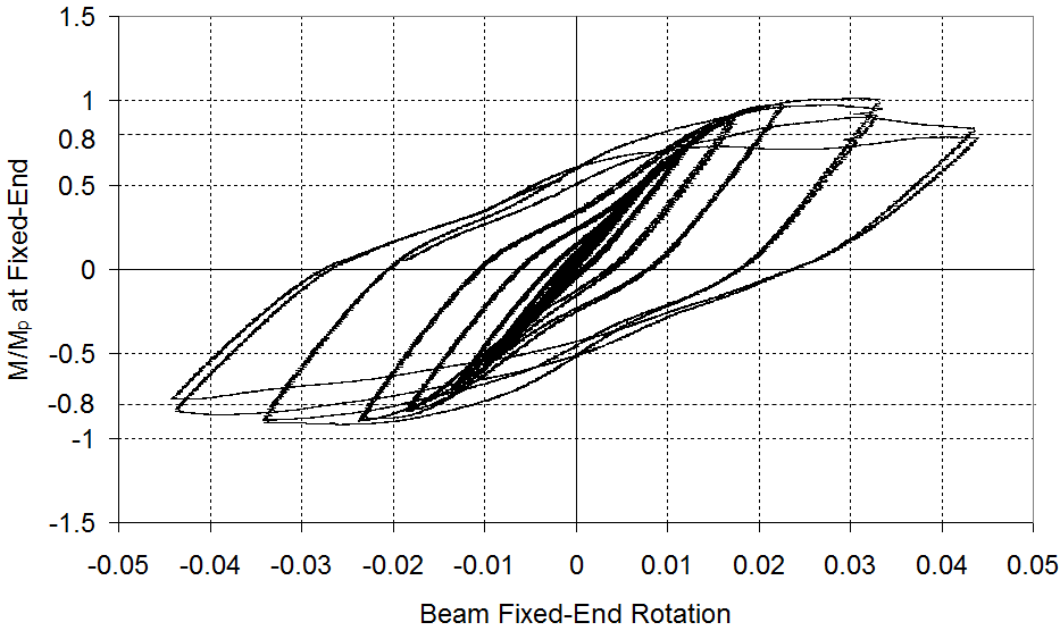

Figure 4.44. HE500AA GFRP2 Beam Fixed-End Rotation vs. M/M_p

4.2.2. Beam Strain Gage Data

HE400AA beams were tested with welded haunch (WH) modification while HE500AA beams without WH modification and therefore strain gage (SG) readings from these experiments were evaluated in two parts: HE400AA Beams and HE500AA Beams.

4.2.2.1. HE400AA Beams

As discussed in chapter 3, HE400AA beams were mounted with post-yield steel strain gages and composite strain gages. In this section significant evaluations related to the strain gage readings were discussed. The strain gage layout for the top and bottom flanges is shown in Figure 3.9.

Figure 4.45 demonstrates the strain distribution through top flange width of HE400AA bare beam for both positive and negative rotations and the results shown are related to the first cycle of the beam WH tip rotations of 1%, 1.5%, 2%, 2.4% and 3.4%. Strain gauges (SG-401, SG-402 and SG-403) were mounted on the top of the

top flange, at 75 mm from the endplate as shown in Figure 3.9. As seen in Figure 4.45 strains on top flange began to lose their uniformity in higher cycles and particularly after 2.4% rotation strain distribution was deteriorated due to the local buckling. Top flange strains in positive rotation increased while those in negative rotations began to decrease after the so-called cycle.

Figure 4.46 shows top flange longitudinal strain distribution of HE400AA bare beam while Figure 4.47 shows bottom flange longitudinal strain distribution of it for both positive and negative rotations and their results are related to the WH tip rotations, which are from 1% to 3.4%. Top flange strain gages (SG-402 and SG-407) were mounted on the top of the top flange, at 75 mm from endplate and 75 mm from the center of the stiffener (295 mm from endplate), respectively and bottom flange strain gages (SG-404 and SG-409) were mounted on the top of the bottom flange, at 75 mm from endplate and 75 mm from the center of the stiffener (295 mm from endplate), respectively as shown in Figure 3.9. As seen in Figure 4.46 top flange strains at 75 mm from endplate were more than those at 295 mm from endplate and this condition was consistent with the test observation where local flange buckling occurred in the welded haunch region. On the other hand, bottom flange strains at 75 mm from endplate (in the WH region) were much smaller than those at 295 mm from endplate. It is the result of the change of force flow path by means of welded haunch and strain demand reduces in this region (Yu et al. 2000). Therefore, local flange buckling occurred beyond the welded haunch as applied load increased.

HE400AA GFRP3 beam SG-C403 composite strain gage reading is shown in Figure 4.48. This gage was located 75 mm from stiffener (295 mm from endplate) as shown in Figure 3.9. Strain values remained on the order of 0.002-0.003 as seen in Figure 4.48 because adhesive layer between steel and GFRP failed due to the larger shear stresses.

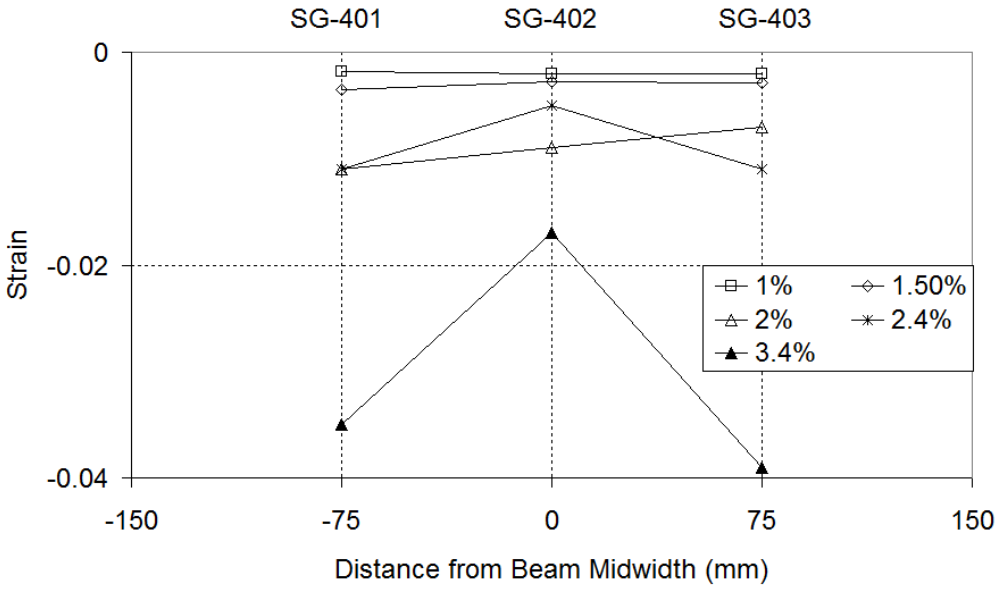

a) Positive Rotation

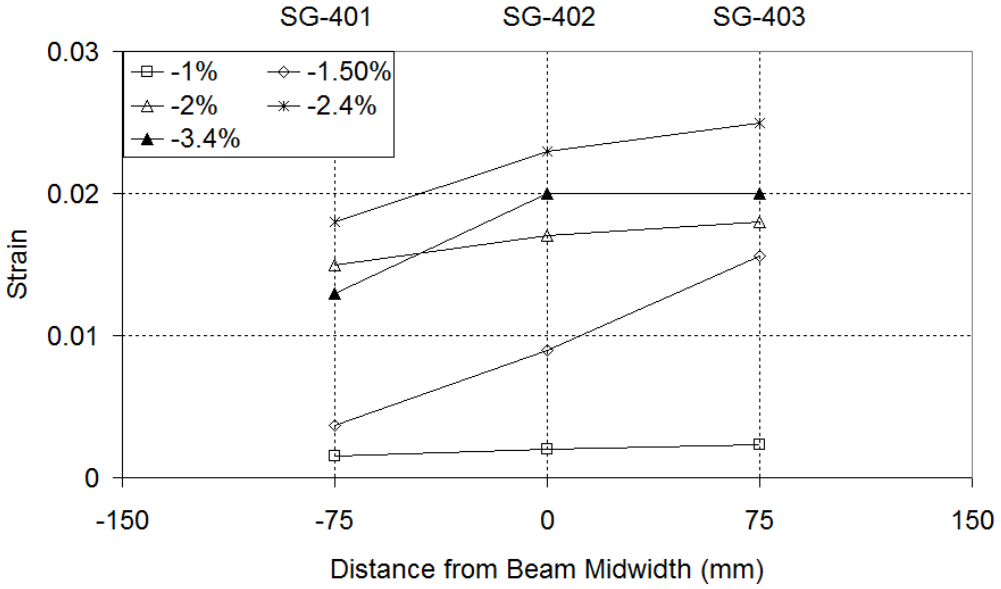

b) Negative Rotation

Figure 4.45. HE400AA Bare Beam Top Flange Width Strain Distribution

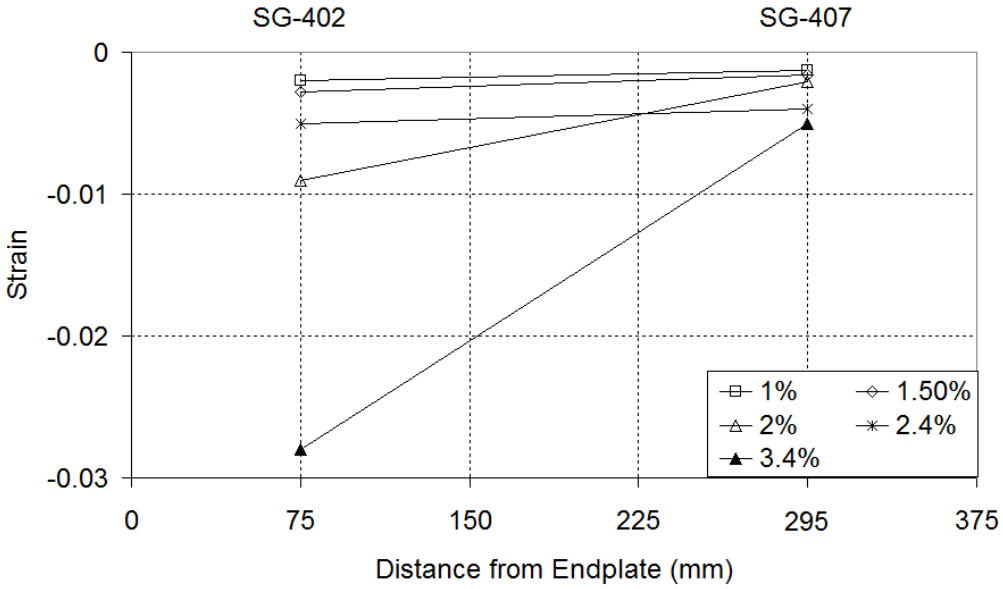

a) Positive Rotation

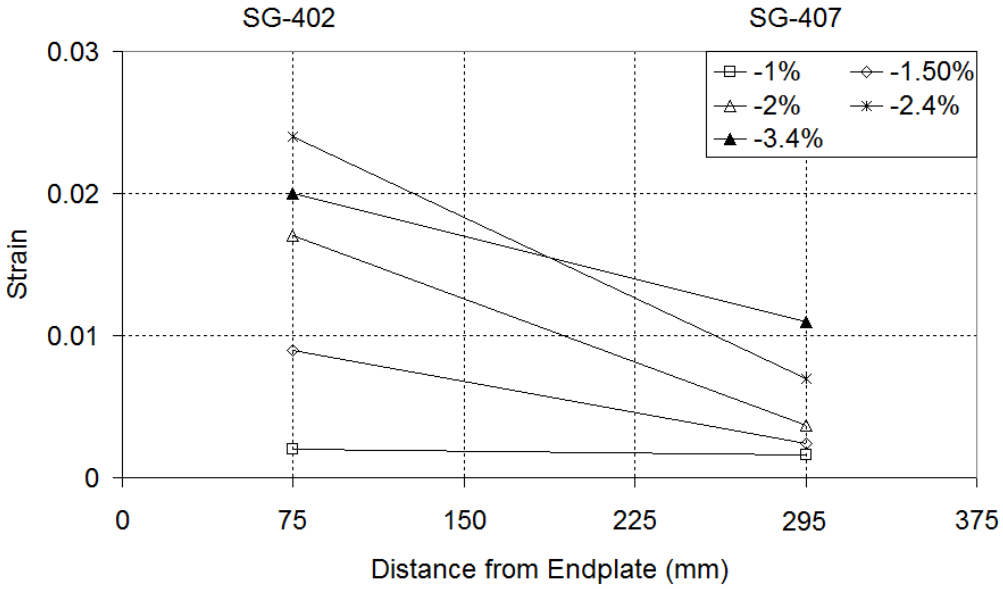

b) Negative Rotation

Figure 4.46. HE400AA Bare Beam Top Flange Longitudinal Strain Distribution

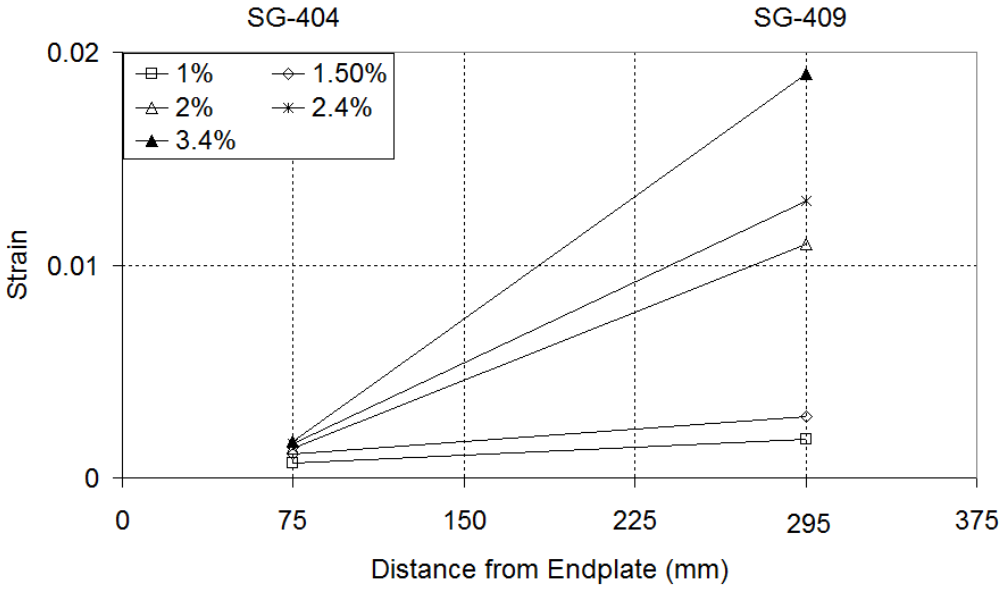

a) Positive Rotation

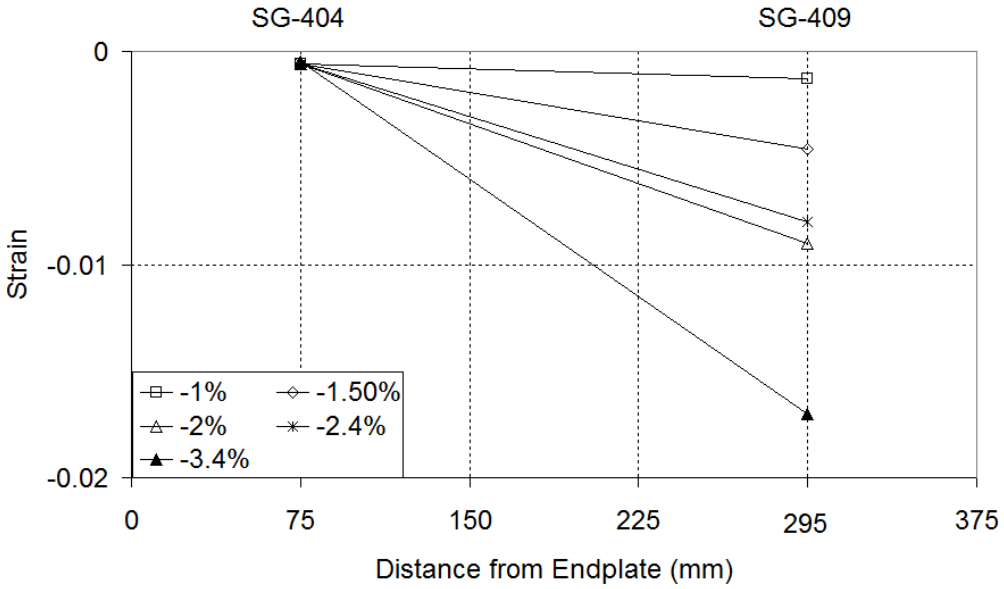

b) Negative Rotation

Figure 4.47. HE400AA Bare Beam Bottom Flange Longitudinal Strain Distribution

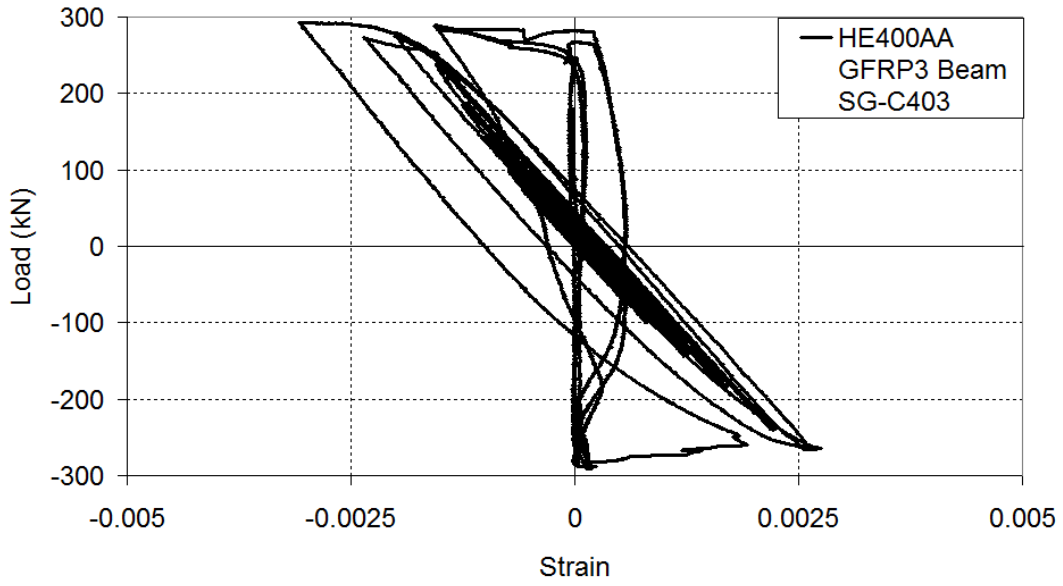

Figure 4.48. HE400AA GFRP3 Beam SG-C403 Reading

4.2.2.2. HE500AA Beams

As discussed in Chapter 3 HE500AA beams were mounted with post-yield steel strain gages and composite strain gages. In this section significant evaluations related to the strain gage readings were discussed. The strain gage layout for the top and bottom flanges is shown in Figure 3.11.

Figure 4.49 demonstrates the strain distribution through top flange width of HE500AA bare beam for both positive and negative rotations and the results shown are related to the first cycle of the beam fixed-end rotations of 1.2%, 1.7%, 2.2%, 3.3% and 4.2%. Strain gauges (SG-501, SG-502 and SG-503) were mounted on the top of the top flange, at 75 mm from the endplate as shown in Figure 3.11. As seen in Figure 4.49 strain values were on increase up to the 3.3% positive beam fixed-end rotation and they were also in a uniform behavior. However, after 3.3% rotation strain values began to lose their uniformity through top flange width due to the local flange buckling occurred and began to decrease gradually as the applied load decreased because of the fact that plastic moment capacity was exceeded. The similar behavior

happened for negative rotations from 2.2% rotation on and as the load-carrying capacity of the section decreased the top flange strain profile was on the decrease.

Figure 4.50 demonstrates the strain distribution through bottom flange width of HE500AA bare beam for both positive and negative rotations and the results shown are related to the first cycle of the beam fixed-end rotations from 1.2% to 4.2%. Strain gauges (SG-504, SG-505 and SG-506) were mounted on the bottom of the bottom flange, at 75 mm from the endplate as shown in Figure 4.50. Bottom flange strains were on increase up to the 3.3% rotation for negative rotations and decreased after this rotation value because of flange local buckling. On the other hand, bottom flange strains for the positive rotations were nearly uniform in early cycles and then the strain distribution changed through the formation of local flange buckles.

HE500AA GFRP2 beam SG-C402 composite strain gage reading is shown in Figure 4.51. This gage was located 75 mm from endplate as shown in Figure 3.11. Strain values remained elastic on the order of 0.0015 as seen in Figure 4.51 and then GFRP material were subjected to inelastic deformation resulting higher strain values. Anchorage plates used in HE500AA GFRP2 beam experiment provided that GFRP interface layer remained intact in higher cycles and strain values were on increase as load were constant and also it also prevented early debonding.

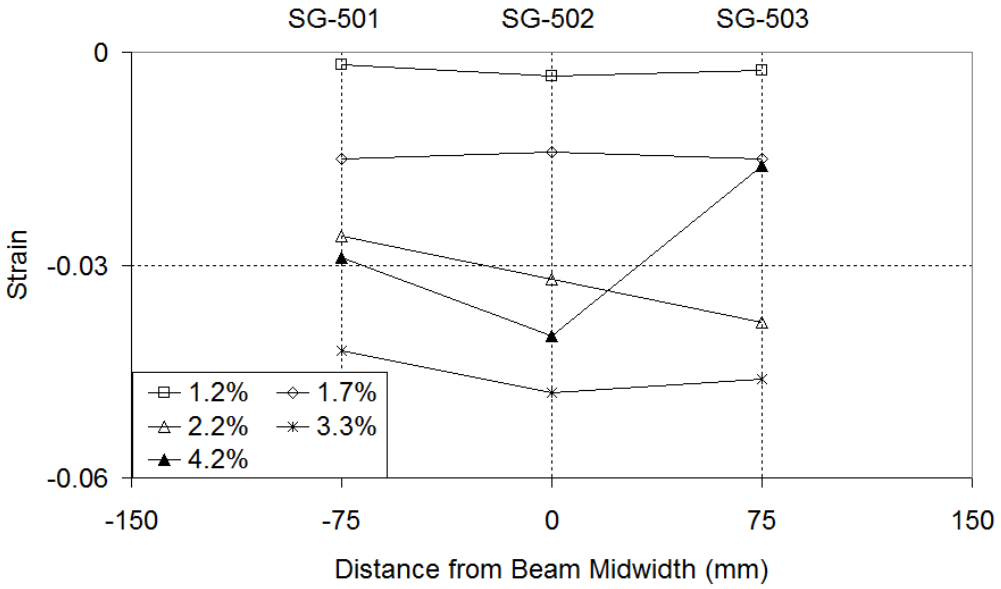

a) Positive Rotation

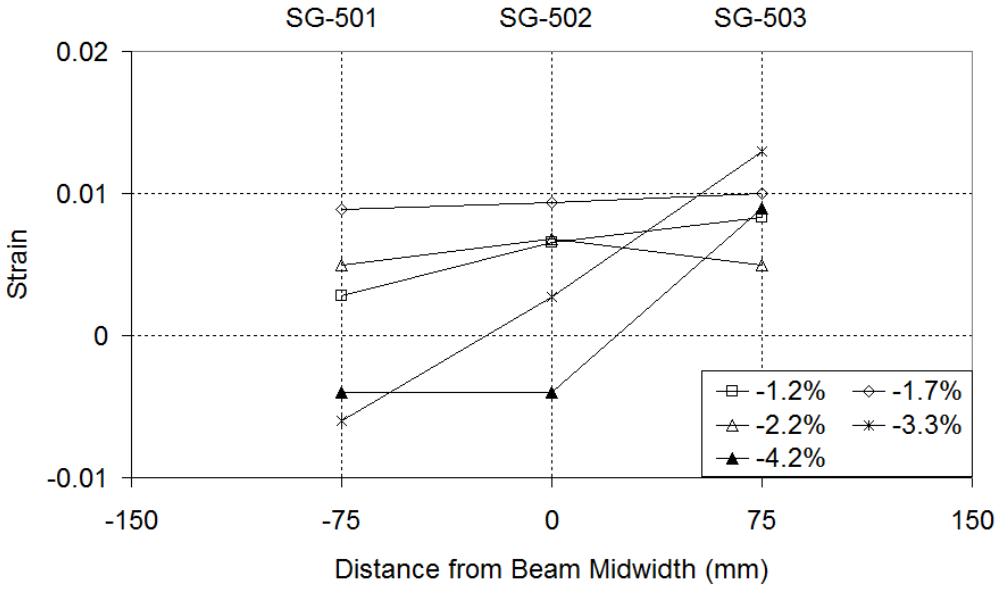

b) Negative Rotation

Figure 4.49. HE500AA Bare Beam Top Flange Width Strain Distribution

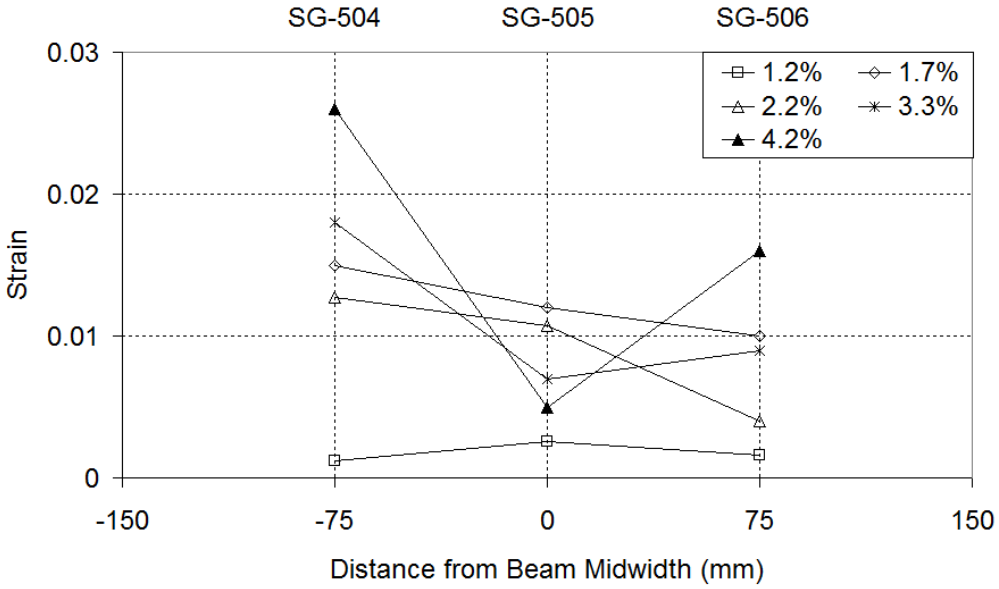

a) Positive Rotation

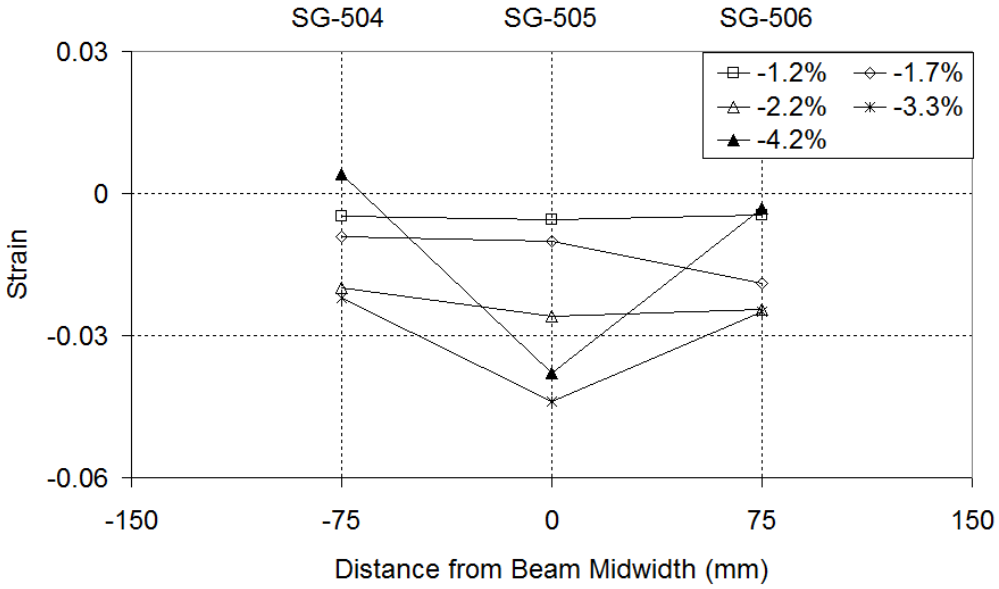

b) Negative Rotation

Figure 4.50. HE500AA Bare Beam Bottom Flange Width Strain Distribution

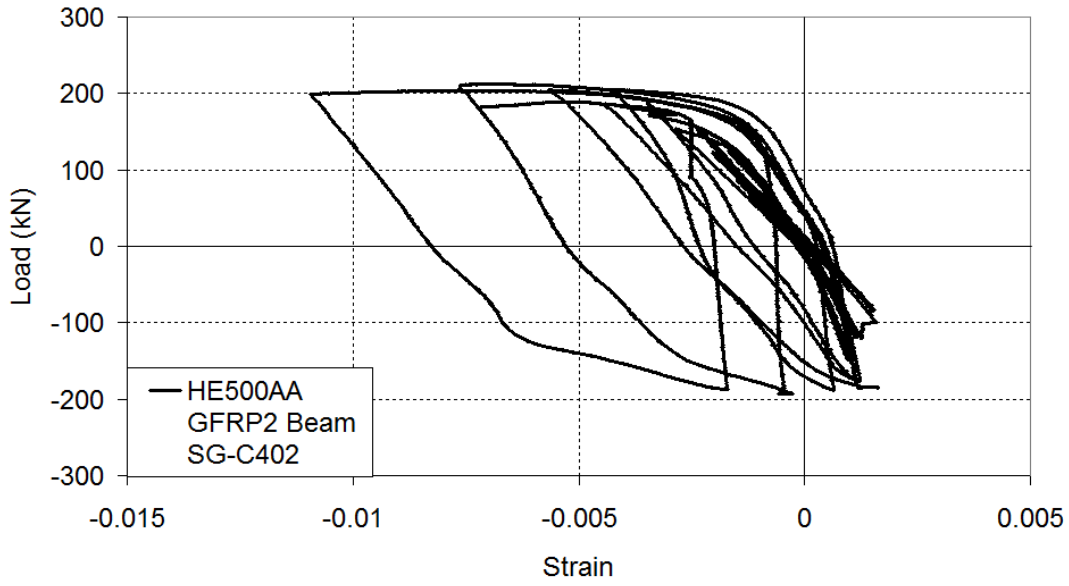

Figure 4.51. HE500AA GFRP3 Beam SG-C402 Reading

CHAPTER 5

PERFORMANCE COMPARISONS

5.1. Comparisons of HE400AA Beams

The cyclic behavior of HE400AA bare beam was compared with that of HE400AA GFRP1, GFRP2 and GFRP3, respectively and comparisons were performed between each of HE400AA GFRP beams. Due to the rigid body rotation at the beam support frame connection mentioned in Chapter 3, the load cycles applied to the HE400AA beams are not totally compatible with AISC (2005b) loading protocol. Positive rotation implies the top flange is in compression and negative rotation implies bottom flange is in compression.

Furthermore, the buckling behaviors of HE400AA beams are summarized in this section in order to obtain a clear comparison.

5.1.1. HE400AA Bare Beam versus HE400AA GFRP1 Beam

The cyclic behavior of HE400AA bare beam was compared with the cyclic behavior of HE400AA GFRP1 beam, which has three layers GFRP wrapping at the plastic hinge and WH regions. In Figure 4.1 load versus beam rotation at welded haunch tip for HE400AA bare and GFRP1 beams is shown. HE400AA bare beam and GFRP1 beam tests were stopped in the second cycle of 0.034 and in the first cycle of 0.045 rad rotations, respectively. The cyclic behavior of HE400AA bare and GFRP1 beams up to the around 0.03 rad rotations are similar for positive rotations and GFRP1 beam at the 0.033 rad WH tip rotation has slightly more load than bare beam at the 0.034 rad WH tip rotation. The WH tip rotations for negative rotations of HE400AA bare and GFRP1 beams are different and therefore comparing the beams are quite difficult in the negative rotations. Nevertheless, it is seen that the load is on decrease after 0.024 rad negative WH tip rotation for bare beam.

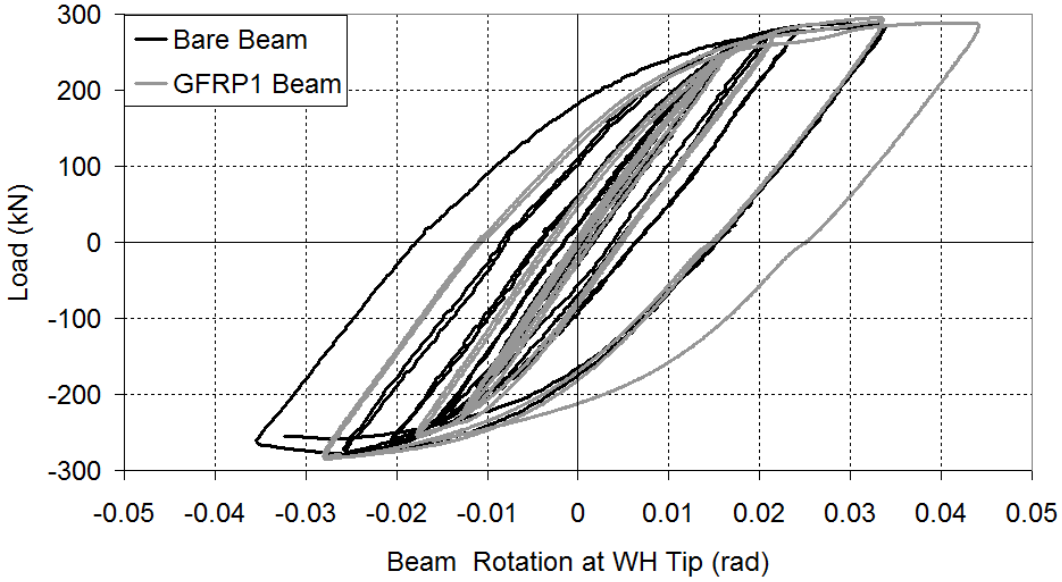

Figure 5.1. HE400AA Bare Beam vs. HE400AA GFRP1 Beam

5.1.2. HE400AA Bare Beam versus HE400AA GFRP2 Beam

The cyclic behavior of HE400AA bare beam was compared with the cyclic behavior of HE400AA GFRP2 beam that has five layers separate GFRP application. In Figure 5.2 load versus beam rotation at WH tip for HE400AA bare and GFRP2 beams is shown. HE400AA bare beam experiment was stopped in the second cycle of 0.034 rad rotation while HE400AA GFRP2 beam experienced top flange fracture in the first cycle of 0.046 rad negative rotation. The cyclic behavior of HE400AA bare and GFRP2 beams up to the 0.023 rad rotation are similar for positive rotations. GFRP2 beam even experienced more load decrease than bare beam at the 0.034 rad positive WH tip rotation. Load carrying capacity of HE400AA GFRP2 beam continued to decrease during the first cycle of 0.046 rad positive WH tip rotation and top flange fracture occurred. As looking into the negative rotation comparisons, a similarity can be seen between cyclic behaviors of bare and GFRP2 beams up to the 0.023 rad negative WH tip rotation. However, GFRP2 beam carries more load than bare beam at the 0.034 rad negative WH tip rotation and this is due to the mitigation

effect of the GFRP on the bottom flange local buckling (FLB). Consequently, GFRP reinforcement postponed bottom FLB as one cycle.

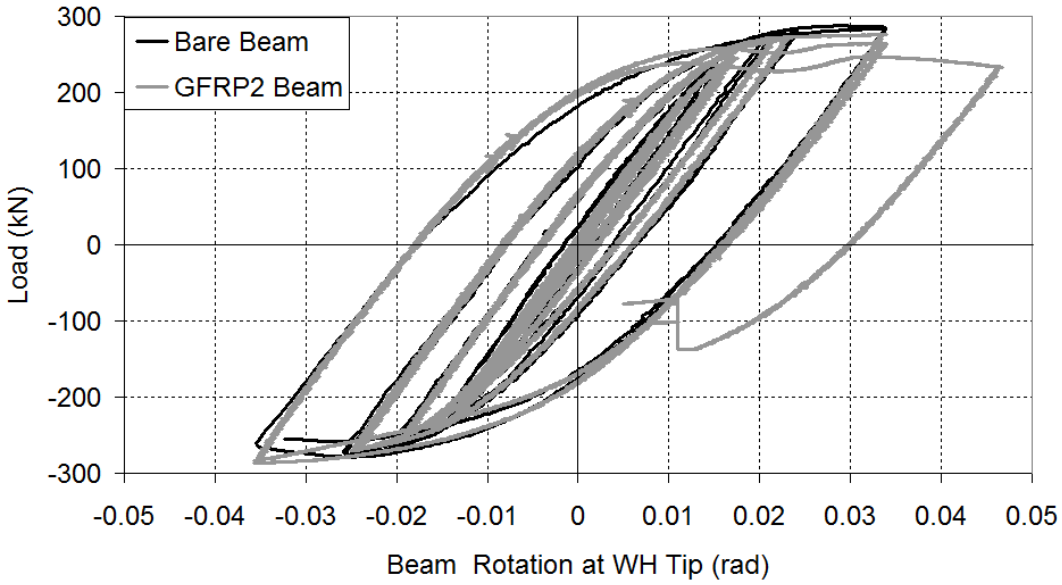

Figure 5.2. HE400AA Bare Beam vs. HE400AA GFRP2 Beam

5.1.3. HE400AA Bare Beam versus HE400AA GFRP3 Beam

The cyclic behavior of HE400AA bare beam was compared with the cyclic behavior of HE400AA GFRP3 beam, which has three layers continuous GFRP application. Load versus beam rotation at WH tip plot for HE400AA bare and GFRP3 beams is shown in Figure 5.3. Both HE400AA GFRP1 and GFRP2 beams experienced problems in the last rotation cycle. However, GFRP3 beam completed all the cycles and did not experience any failure. The cyclic behavior of bare beam at the 0.034 rad WH tip rotation and the cyclic behavior of GFRP2 beam at the 0.033 rad WH tip rotation are similar for positive rotations. As for the negative rotations, it is seen that the cyclic performance of GFRP3 beam is better than that of bare beam due to the mitigation effect of GFRP material on the bottom flange buckling. HE400AA bare beam experienced decrease on load carrying capacity in the 0.034 rad negative WH tip rotation while such a situation for GFRP3 beam did not occur because of the abovementioned condition. As a result, bottom flange local buckles were postponed

one cycle and load carrying capacity of the beam increased due to the GFRP rehabilitation.

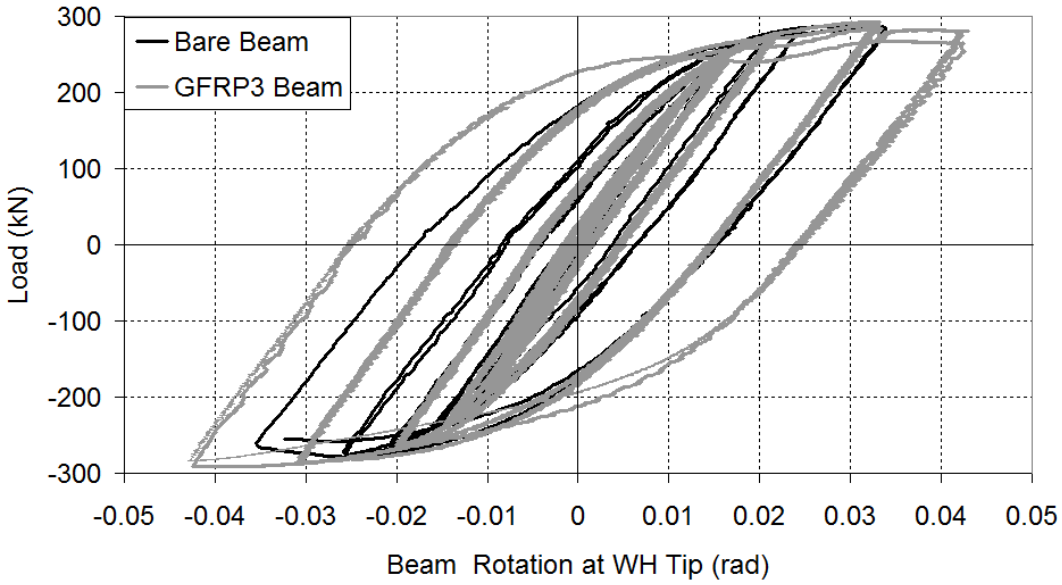

Figure 5.3. HE400AA Bare Beam vs. HE400AA GFRP3 Beam

5.1.4. HE400AA GFRP1 Beam versus HE400AA GFRP2 Beam

For the HE400AA GFRP1 beam, GFRP layers were wrapped continuously around the plastic hinge region and also placed at the top and bottom of the top flange inside the WH region as three layers while GFRP layers were bonded to the top and bottom flanges separately as five layers for the HE400AA GFRP2 beam.

The cyclic behavior of HE400AA GFRP1 beam was compared with the cyclic behavior of HE400AA GFRP2 beam. Load versus beam fixed-end rotation plot for GFRP1 and GFRP2 beam is shown in Figure 5.4. Even though both beams have different negative WH tip rotations, it can be concluded that they have similar behaviors for negative rotations. As for the positive rotations, it is seen that GFRP1 beam demonstrates better cyclic performance than GFRP2 beam. During and after 0.034 rad positive rotation, GFRP2 beam experienced much more decrease on load carrying capacity than GFRP1 beam. This poor performance of GFRP2 beam arose from that GFRP layers did not apply continuously on the flanges. As a consequence,

it is appreciated that bonding GFRP layers in a separate manner is not a proper alternative for such applications.

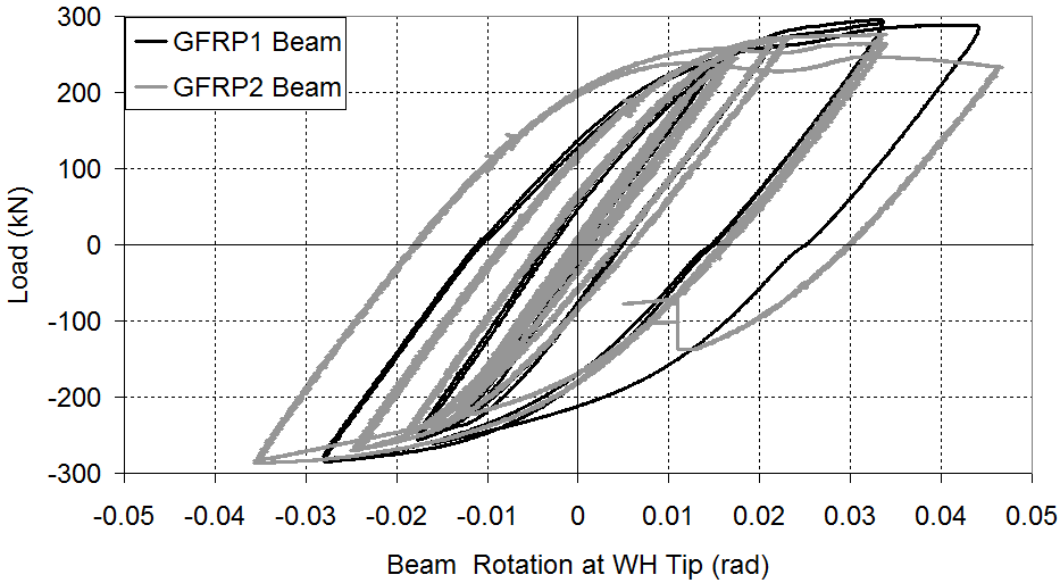

Figure 5.4. HE400AA GFRP1 Beam vs. HE400AA GFRP2 Beam

5.1.5. HE400AA GFRP1 Beam versus HE400AA GFRP3 Beam

For the HE400AA GFRP1 beam, GFRP materials were wrapped continuously around the plastic hinge region and also placed at the top and bottom of the top flange inside the WH region as three layers while they were applied to the top flange in the WH region and to the top and bottom flanges in the plastic hinge region as three layers for the HE400AA GFRP3 beam. Also in the GFRP3 experiment, GFRP layers were bonded to the flanges in a bending manner from outer parts of the flanges to the inner parts of them.

The cyclic behavior of HE400AA GFRP1 beam was compared with the cyclic behavior of HE400AA GFRP3 beam. Load versus beam fixed-end rotation plot for GFRP1 and GFRP3 beam is shown in Figure 5.5 and as seen in this figure cyclic behavior of GFRP1 and GFRP3 beams up to the 0.033 rad rotation are similar for both positive and negative rotations. On the account of the fact that GFRP1 beam test was stopped in the first cycle of 0.044 rad rotation there is no possibility to compare

beams for further cycles. Nevertheless, the similarity between cyclic behaviors of these two beams demonstrates the fact that web wrapping is not necessary for such applications.

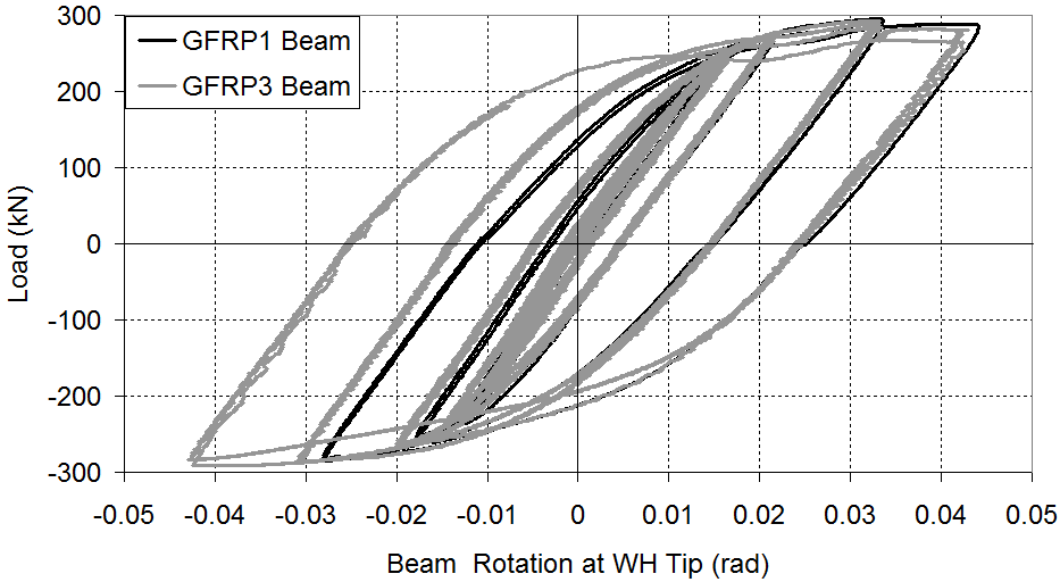

Figure 5.5. HE400AA GFRP1 Beam vs. HE400AA GFRP3 Beam

5.1.6. HE400AA GFRP2 Beam versus HE400AA GFRP3 Beam

For the HE400AA GFRP2 beam, GFRP materials were bonded to the top flange in WH region and to the top and bottom flanges in the plastic hinge region separately as five layers while they were applied to the top flange in the WH region and to the top and bottom flanges in the plastic hinge region as three layers in a bending manner from outer parts of the flanges to the inner parts of them for the HE400AA GFRP3 beam in order to maintain continuity in GFRP application.

The cyclic behavior of HE400AA GFRP2 beam was compared with the cyclic behavior of HE400AA GFRP3 beam. Load versus beam fixed-end rotation plot for GFRP2 and GFRP3 beam is shown in Figure 5.6 and as seen in this figure cyclic behavior of GFRP2 and GFRP3 beams in the low rad rotations are similar for positive rotations. However, the superiority of GFRP3 beam for cyclic performance is seen from the 0.022 rad positive rotation on and GFRP2 beam has much more load

decrease than GFRP3 beam. As for the negative rotations, the fact that GFRP3 beam in the 0.043 rad rotation carries more load than GFRP2 beam in the 0.034 rad rotation is a clear indication for the better cyclic performance of GFRP3 beam.

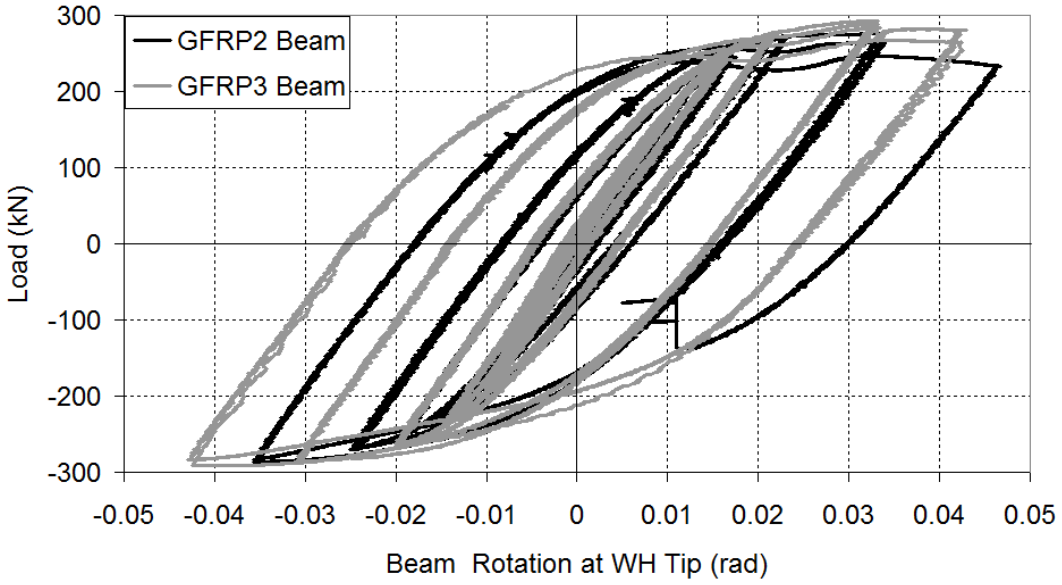

Figure 5.6. HE400AA GFRP2 Beam vs. HE400AA GFRP3 Beam

5.1.7. Local Flange Buckling Comparison of HE400AA Beams

HE400AA beams that have welded haunch (WH) modification were tested with various GFRP configurations in order to obtain most suitable GFRP reinforcement application aiming at improving seismic behavior and structural ductility. However, local buckles are significant phenomenon, which prevent to exhibit highly ductile behavior of sections under earthquake-induced forces and therefore it is aimed to mitigate these inelastic instabilities using GFRP. In Figure 5.7 and Figure 5.8, top and bottom flange local buckling (FLB) comparisons of HE400AA beams are presented respectively and the values in these plots indicate that the beam rotation values where prominent FLB occurred.

Beam rotation values in loading protocols are somewhat different from each other because of the previously stated fixed-end problem and therefore this condition has been taken into account for the beam FLB comparisons. As it is seen in Figure

5.7, rotation cycles where prominent top flange buckling happened are almost similar for all of the HE400AA beams. This condition represents that GFRP reinforcement is not effective in postponing the top flange local buckling under cyclic loading. As for the bottom FLB, the efficiency of GFRP reinforcement can be seen in Figure 5.8. The prominent bottom FLB has been postponed as one cycle by means of using GFRP in HE400AA GFRP2 and GFRP3 beams tests. Because GFRP1 beam did not experience prominent FLB, the comparison of it did not take place in Figure 5.8. The difference between top and bottom flange local buckles arise from that GFRP reinforcement can be more effective by means of the welded haunch at the bottom flange.

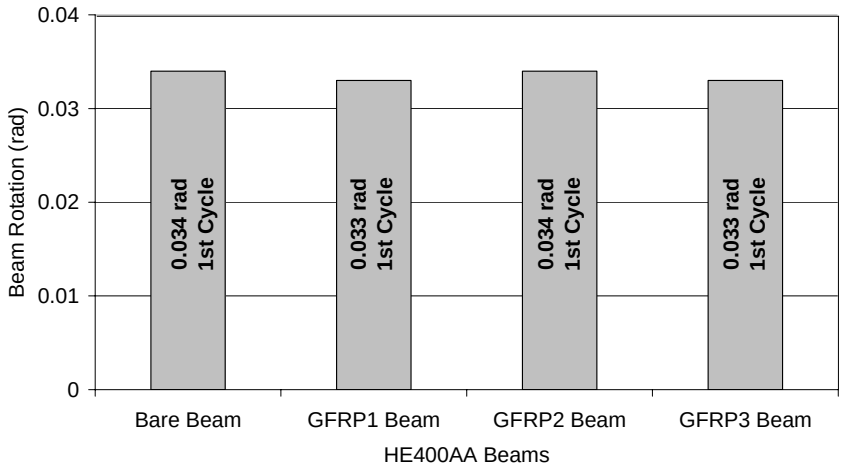

Figure 5.7. HE400AA Beams Top Flange Local Buckling Comparison

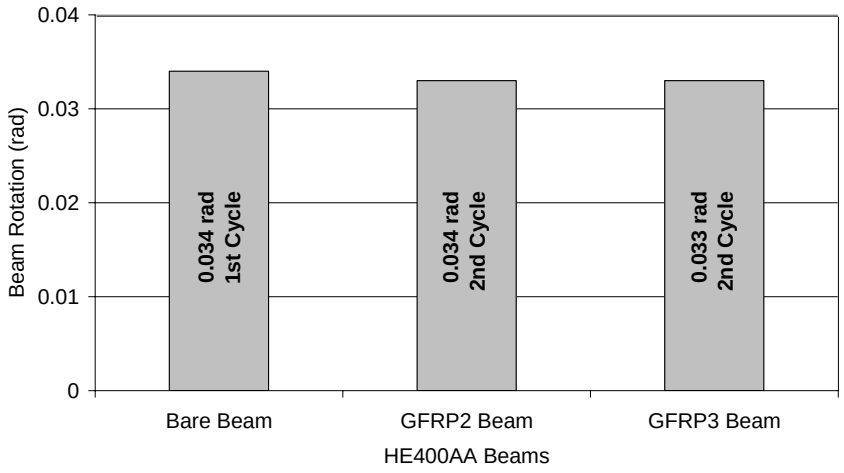

Figure 5.8. HE400AA Beams Bottom Flange Local Buckling Comparison

5.2. Comparison of HE500AA Beams

The cyclic behavior of HE500AA bare beam was compared with that of HE500AA GFRP1 and GFRP2, respectively and also comparisons were carried out between HE500AA GFRP1 and GFRP2 beams. As mentioned in the previous chapter HE500AA GFRP1 beam experienced sudden load decrease and behavior discrepancy and therefore it was believed that the comparisons with GFRP1 beam was not meaningful. Nevertheless, the related comparisons are shown in figures. Fixed-end rotations seen in figures have differences from SAC loading protocol due to the previously stated fixed-end problem of connection. Positive rotation implies the top flange is in compression and negative rotation implies bottom flange is in compression.

5.2.1. HE500AA Bare Beam versus HE500AA GFRP1 Beam

The cyclic behavior of HE500AA bare beam was compared with the cyclic behavior of HE500AA GFRP1 beam, which has three layers continuous GFRP application. Load versus beam fixed-end rotation plot for HE500AA bare and GFRP1 beam is shown in Figure 5.9.

HE500AA GFRP1 beam experienced sudden load decrease and behavior discrepancy in the aftermath of the 0.022 rad positive rotation and this situation were not observed in any other beam experiment through research project. Thus, it was decided on that comparing the bare beam with GFRP1 beam would not be meaningful.

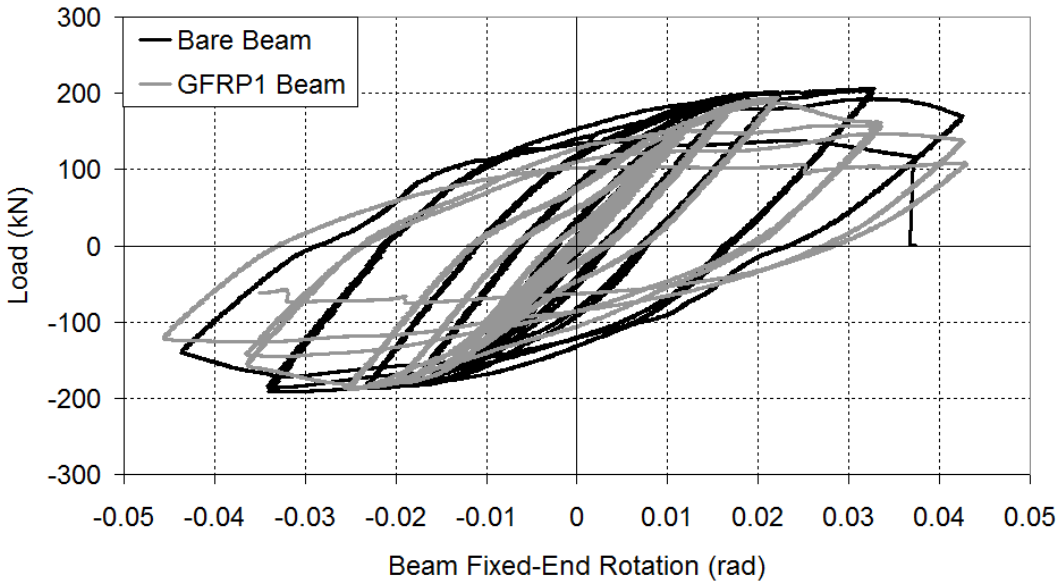

Figure 5.9. HE500AA Bare Beam vs. HE500AA GFRP1 Beam

5.2.2. HE500AA Bare Beam versus HE500AA GFRP2 Beam

The cyclic behavior of HE500AA bare beam was compared with the cyclic behavior of HE500AA GFRP2 beam, which has three layers continuous GFRP application. In addition, GFRP2 beam has anchorage plates in order to postpone debonding in higher cycles and increase beam inelastic performance. Load versus beam fixed-end rotation plot for HE500AA bare and GFRP2 beam is shown in Figure 5.10.

HE500AA GFRP2 beam completed all cycles including 0.044 rad rotation while HE500AA bare beam failed in the second cycle of 0.042 rad rotation. The cyclic behaviors of HE400AA bare and GFRP2 beams up to the 0.023 rad rotation are similar for both positive rotations. GFRP2 beam in the 0.034 rad positive rotation demonstrates better cyclic performance than bare beam in the 0.033 rad positive rotation as well as in the 0.044 and 0.042 rad positive rotations for GFRP2 and bare beams, respectively. Particularly, GFRP2 beam in 0.044 rad positive rotation has more load carrying capacity than bare beam, which could not complete this rotation due to failure in the 0.042 rad positive rotation. As for the negative rotations, it is

seen that the cyclic behavior of GFRP2 beam in the 0.034 rad negative rotation and bare beam in the 0.033 rad negative rotation are similar. However, bare beam especially after first cycle of 0.042 rad rotation experienced much more decrease on load carrying capacity and it is seen in Figure 5.10 that GFRP2 beam showed better inelastic performance than bare beam. The reason of this situation in the negative rotation was that bare beam demonstrated poor inelastic performance after it experienced the first high displacement in the 0.042 rad positive rotation. Whereas GFRP2 beam having anchorage plates along the plastic hinge region did not show such a poor inelastic performance and completed this cycle with relatively low decrease on load carrying capacity. Consequently, beam load carrying and inelastic capacities were improved by means of GFRP reinforcement and anchorage plates, and local flange and web buckling were postponed and mitigated.

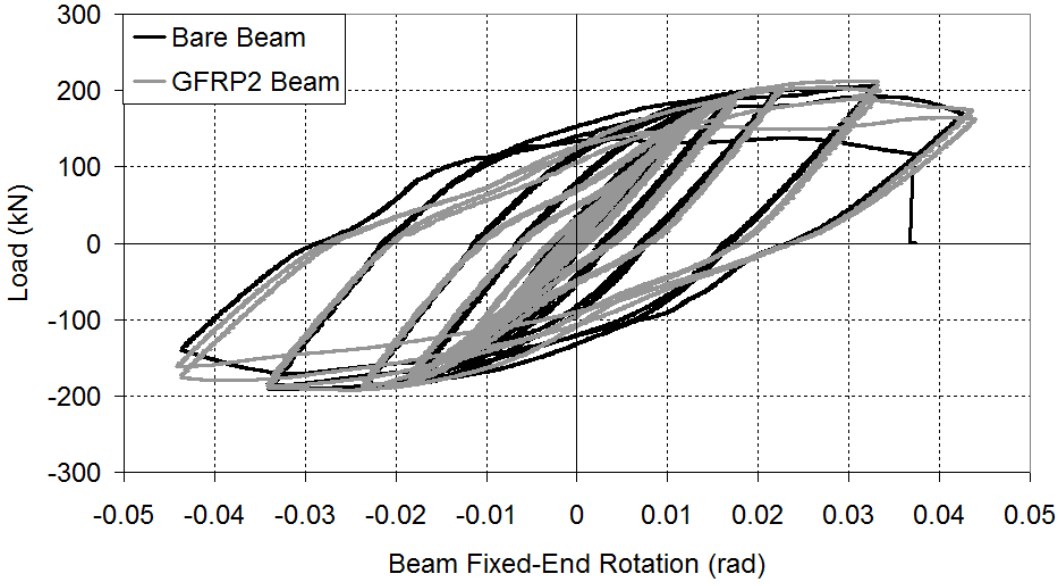

Figure 5.10. HE500AA Bare Beam vs. HE500AA GFRP2 Beam

5.2.3. HE500AA GFRP1 Beam versus HE500AA GFRP2 Beam

For the HE500AA GFRP1 beam, GFRP layers were applied continuously to the top and bottom flanges along the plastic hinge region as three layers. HE500AA

GFRP2 beam has the same GFRP applications with the GFRP1 beam and it also has anchorage plates along the GFRP application region.

The cyclic behavior of HE500AA GFRP1 beam was compared with the cyclic behavior of HE500AA GFRP2 beam. Load versus beam fixed-end rotation plot for GFRP1 and GFRP2 beam is shown in Figure 5.11. As mentioned previously HE500AA GFRP1 beam experienced sudden load decrease and behavior discrepancy and therefore it was believed that the comparison between GFRP1 and GFRP2 beams was not meaningful. Besides, GFRP1 beam experienced much more load decrease in the 0.043 rad rotation because of this behavior instability and could not complete the last cycles. On the other hand, GFRP2 beam showed great inelastic performance and could complete all the cycles without any failure.

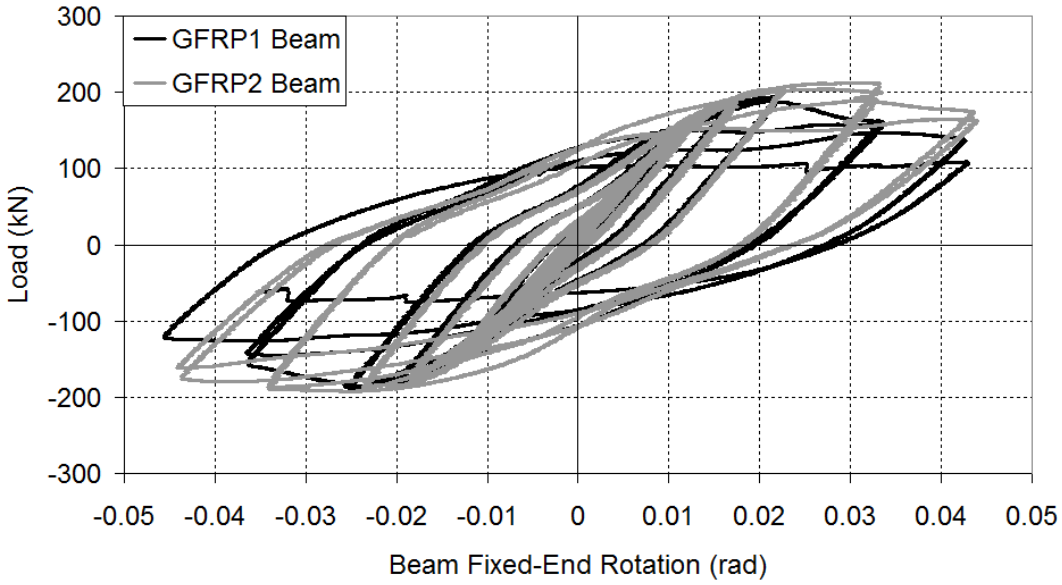

Figure 5.11. HE400AA GFRP1 Beam vs. HE400AA GFRP3 Beam

5.2.4. Local Flange Buckling Comparison of HE500AA Beams

HE500AA beams that have no modification were tested as two GFRP reinforcement beams and one bare beam. Both GFRP1 and GFRP2 beams have three layers GFRP reinforcement while GFRP2 beam has also anchorage plates. In Figure 5.12 and Figure 5.13, top and bottom flange local buckling (FLB) comparisons of

HE500AA beams are presented respectively and the values in these plots indicate that the beam rotation values where prominent FLB occurred.

As seen in both Figure 5.12 and Figure 5.13, GFRP2 beam, which has both GFRP and anchorage plate reinforcement demonstrates much more efficient performance in terms of flange local buckling. Particularly, the application of anchorage plates on GFRP has contributed to the postponing of FLB to the later cycles (as two cycles). GFRP2 beam has experienced prominent FLB in the first cycle of 0.034 rad rotation while bare beam in the first cycle of 0.022 rad rotation, for both top and bottom flanges. In addition, GFRP1 beam did not take place in the FLB comparisons due to unexpected poor cyclic performance.

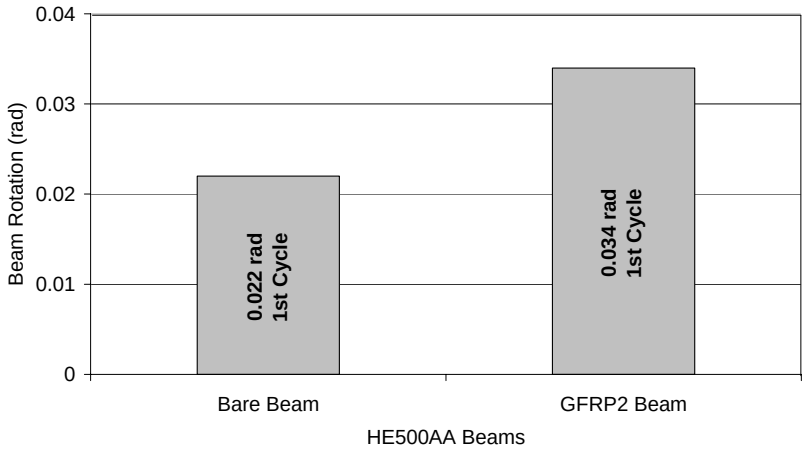

Figure 5.12. HE500AA Beams Top Flange Local Buckling Comparison

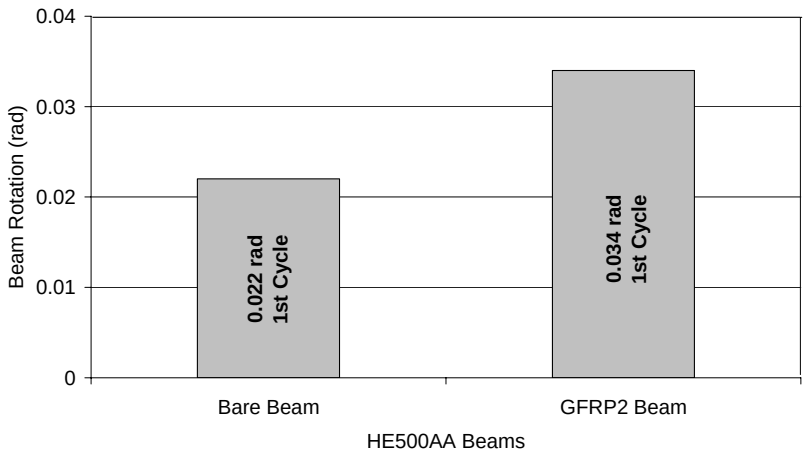

Figure 5.13. HE500AA Beams Bottom Flange Local Buckling Comparison

The cyclic performance of HE500AA GFRP2 beam demonstrates that utilizing anchorage plates with GFRP reinforcement are more successful in terms of local buckling and debonding problems. By means of the anchorage plates, GFRP materials can be much more effective on the account of the fact that interface layer between steel and GFRP remains intact in higher cycles and this condition mitigates and postpones the local flange buckling. Therefore, it is seen that GFRP application with anchorage plates are prone to increase inelastic performance of the system and improves structural ductility and stability by mitigating structural instabilities.

CHAPTER 6

CONCLUSIONS

6.1. Introduction

In this experimental study behavior of steel I-beams that have larger flange slenderness ratios than those specified in the last earthquake codes (AISC 2005c, Eurocode-8 2003, DBYBHY 2007), under cyclic loading is investigated. The experimental program involved seven large-scale beam-column connection tests some of which are modified by glass fiber reinforced polymer (GFRP). In the first phase, HE400AA beams with welded haunch (WH) modification were tested. Second phase involved HE500AA regular beams. Originally, HE500AA beams were planned to have reduced beam section (RBS) modification. Conducted analytical study showed that GFRP modification was not effective on RBS modified beams. Therefore, experimental study was performed with unmodified regular HE500AA beams. Through the tests, the contribution of GFRP reinforcement to the mitigation of local flange and web buckling on the plastic hinge region of steel I-beams is investigated. In this chapter first, results obtained from experiments and then recommendations on the use of GFRP are presented.

6.2. Experimental Study

In this experimental study a total of seven beam-column connection tests were conducted under cyclic loading and two types of I-beam sections were used: HE400AA and HE500AA. Four HE400AA beam having WH modification and three HE500AA beam with no modification were tested with various GFRP applications in order to determine the most suitable GFRP application, which mitigates local buckling, as presented in Table 6.1 in a detailed way. Important characteristics of pre-experiment stage such as surface preparation, epoxy application and surface primer

selection were based on the results and determinations obtained from small-scale GFRP tests, which took part in the research program.

The depth/width ratio of HE400AA beam is 1.26 while the depth/width ratio of HE500AA beam is 1.57 and both of the sections are shallow sections. The flange slenderness ratios of HE400AA and HE500AA beams are 11.53 and 10.71, respectively while the web slenderness ratios of HE400AA and HE500AA beams are 31.36 and 37.14, respectively and as it is seen the flange slenderness ratios for both beam sections as well are larger than 7.2, which specified in AISC 2005c.

6.3. Conclusions

Obtained results based on the test results and data evaluations are presented as follows:

1- It was observed that both HE400AA and HE500AA beams had elastic behavior up to the 0.010-0.012 rad rotations.
2- GFRP reinforcement postponed bottom flange local buckling as one cycle for HE400AA beams.
3- Top flange local buckling of HE400AA beams occurred mostly in the WH region and GFRP reinforcement could not performed well due to the debonding phenomenon.
4- The cyclic behaviors are similar up to the 0.03 rad rotations for HE500AA beams (HE500AA bare and GFRP2 beams). HE500AA bare beam experienced prominent plastic moment capacity degradation due to the severe local buckling (particularly in the second cycle of 0.042 rad rotation). However, HE500AA GFRP2 beam was subjected to much less capacity degradation even though it buckled as well.
5- GFRP reinforcement with anchorage plates application postponed both top and bottom flange local buckling as two cycles.
6- Interfacial shear strength, which limited the efficiency of GFRP reinforcement significantly during analytical study, became an important factor in large-scale steel experiments and the interface between steel and GFRP experienced significant amount of debonding in the 0.03-0.04 rad rotations.

7- In order to overcome the interfacial shear strength problem and postpone debonding in the small rotations, the anchorage plates were used on the GFRP material along the plastic hinge region for the HE500AA GFRP2 beam. Thanks to this application, GFRP efficiency and load carrying capacity of the GFRP2 beam increased in the 0.044 rad rotation. GFRP reinforcement supported with the anchorage plates increased the beam inelastic performance by means of mitigation of local flange and web buckling.

8- It was observed that bonding GFRP materials to both faces of top and bottom flanges separately did not result well in terms of load carrying capacity.

9- Bonding of GFRP materials to the top and bottom flanges continuously (in a bending manner from outer parts of the flanges to the inner parts of them) in the plastic hinge region showed more efficient performance by means of postponing debonding particularly for higher cycles of rotations and providing increases on the beam load carrying capacity.

10- Wrapping GFRP along the beam web did not improve the cyclic performance of the beam when compared with the GFRP application, which was only at both faces of top and bottom flanges.

11- Experimental study also indicates that it does not seem possible to rely on GFRP reinforcement to increase the flexural resistance of modified beam-column connections at a rotation of 0.04 radians, which is the target rotation for special moment frames (SMF) on account of the fact that the adhesive layer between steel and GFRP fails in rotations much lower than 0.04 radians. Nevertheless, decrease on the flexural resistance can be restrained to the acceptable value ($0.8M/M_p$) with GFRP materials, which applied continuously.

Table 6.1. HE400AA and HE500AA Beams GFRP Applications

Test Beams	Layout	Application method	Layer
HE400AA Bare Beam	None	None	-
HE400AA GFRP1 Beam	Top and Bottom Flanges + Web	Wrapping as one Fragment	3
HE400AA GFRP2 Beam	Top and Bottom Flanges	Separate Fragments	5
HE400AA GFRP3 Beam	Top and Bottom Flanges	One Fragment to both Faces of the Flanges	3
HE500AA Bare Beam	None	None	-
HE500AA GFRP1 Beam	Top and Bottom Flanges	One Fragment to both Faces of the Flanges	3
HE500AA GFRP2 Beam	Top and Bottom Flanges	One Fragment to both Faces of the Flanges + Anchorage Plates	3

6.4. Recommendations

Based on the results from this experimental study, a number of recommendations related to the GFRP reinforcement for the beams, which are subjected to cyclic loading under earthquake-induced forces are presented as follows:

1- GFRP reinforcement can be applied for deep beam sections, which was investigated in analytical study in research program. The experimental study demonstrated that GFRP reinforcement was not significantly effective in improving seismic behavior of steel I-beams. However, a further experimental study with deep beams should be performed in order to verify analytical results. In addition, dynamic tests can be performed to investigate debonding behavior of steel-GFRP sytems.

2- Epoxy application can be improved with the new materials and techniques in order to obtain higher interfacial shear strength. Particularly, surface preparation is very significant task to accomplish adequate chemical bond formation between steel and FRP. Therefore, it can be improved in accordance with practical in-situ applications.

3- GFRP reinforcement does not contribute to stabilize local buckling in reduced beam sections (RBS). This conclusion based on the analytical results in the research program and beams, which were planned to be conducted with RBS reinforcement, experimented with no modification.

4- GFRP reinforcement is not effective in improving the flexural resistance of modified beam-column connections for the rotation demand of SMF, which is 0.04 radians. However, the seismic performance of the structure can be moderately improved with the bottom flange welded haunch and GFRP reinforcement in order to maintain rotations in accordance with the rotation demand of intermediate moment frames (IMF), which is 0.02 radians.

REFERENCES

Accord, N.B. and Earls, C.J. 2006. Use of fiber reinforced polymer composite elements to enhance structural steel member ductility. *Journal of Composites for Construction*, ASCE, 10(4):337-344.

AISC. 2003a. *Modification of Existing Weld Steel Moment Frame connections for Seismic Resistance. Steel Design Guide Series12.* American Institute of Steel Construction (AISC), Chicago, IL.

AISC. 2003b. *Stiffenening of Wide-Flange Columns at Moment Connections: Wind and Seismic Applications. Steel Design Guide Series13.* American Institute of Steel Construction (AISC), Chicago, IL.

AISC. 2005a. *Pre-qualified Connections for Special and Intermediate Steel Moment Frames for Seismic Applications, American Institute of Steel Construction* (AISC), AISC 358-05, Chicago, IL.

AISC. 2005b. *Seismic provisions for structural steel buildings, American Institute of Steel Construction* (AISC), AISC 341-05, Chicago, IL.

AISC. 2005c. *Specification for structural steel buildings, American Institute of Steel Construction* (AISC), AISC 360-05, Chicago, IL.

Alkan, D. 2008. *Numerical Study of Enhancement of Plastic Rotation Capacity of Seismic Steel Moment Connections by Fiber Reinforced Polymer Materials*. Master of Science Thesis, Izmir Institute of Technology (IYTE), October.

Al-Saidy, A.H., Klaiber, F.W. and Wipf, T.J. 2004. Repair of Steel Composite Beams with Carbon Fiber-Reinforced Polymer Plates. *Journal of Composites for Construction (ASCE)* 8(2): 163-172.

ASTM. 2003. *Standard Test Method for Tension Testing of Metallic Materials (Metric), American Society for Testing and Materials* (ASTM), Designation: E 8M, Vol.03.01 West Conshohocken, PA, USA.

Buyukozturk, O., Gunes, O. and Karaca, E. 2004. Progress on Understanding Deponding Problems in Reinforced Concrete and Steel Members Strengthened Using FRP Composites. *Construction and Building Materials* 18(1): 9-19.

Cadei, J.M., Stanford, T.J. and Hollaway, T.C., eds. 2004. *Strengthening Metallic Structures Using Externally Bonded Fiber-Reinforced Polymers. Publication C595, Construction Industry Research and Information Association* (CIRIA), London, UK: 233.

Chi, B., Uang, C.M. and Chen, A. 2006. Seismic Rehabilitation of Pre-Northridge Steel Moment Connections: A Case Study. *Journal of Constructional Steel Research* 62: 783-792.

Civjan, S.A., Engelhardt, M.D., and Gross, J.L. 2000. Retrofit of Pre-Northridge Moment-Resisting Connections. *Journal of Structural Engineering (ASCE)* 126(4): 445-452.

Civjan, S.A. 1998. *Investigation of Retrofit Techniques for Seismic Resistant Steel Moment Conncetions*. Ph.D. Thesis. The University of Texas at Austin, August, Austin, TX, USA.

Dawood, M. 2005. *Fundamental Behavior of Steel-Concrete Composite Beams Strengthened with High Modulus Carbon Fiber Reinforced Polymer (CFRP) Materials*. Master of Science Thesis, North Carolina State University, Raleigh, NC, USA.

DBYBHY. 2007. *Specification for Structures to be Built in Disaster Areas*. Ankara, Turkey.

DIN. 1989. Testing of resins, hardeners and accelerators, and catalyzed resins, *Deutsches Institut für Normung (DIN)*, Designation: DIN 16945, Berlin, Germany.

DIN. 1994. Testing of rubber - determination of tensile strength at break, tensile stress at yield, elongation at break and stress values in a tensile test, *Deutsches Institut für Normung (DIN)*, Designation: DIN 53504, Berlin, Germany.

DIN. 2001. Paints and varnishes - Determination of density - Part 1: Pyknometer method, *Deutsches Institut für Normung (DIN)*, Designation: DIN EN ISO 2811-1, Berlin, Germany.

Egilmez, O.O. 2010. *Final report, TUBITAK*, Project No: 106Y309.

Egilmez, O.O., Alkan D. and Ozdemir, T. 2009. Cyclic Behavior of Steel I-beams by a Welded Haunch and Reinforced with GFRP. *Steel and Composite Structures* 9(5): 419-444.

Egilmez, O.O., Guven, C.A., Ozdemir, T. and Yormaz, D. 2009. Plastic Rotation Capacity of Beam-Column Connections in Existing Steel Moment Frames by Glass Fiber Reinforced Polymers. , European Commission Research Report Number 046442, April.

Ekiz, E., El-Tawil, S., Parra-Montesinos, G., and Goel, S. 2004. Enhancing Plastic Hinge Behavior in Steel Flexural Members Using CFRP Wraps, *Proceedings of the 13rd World Conference on Earthquake Engineering*: 2496.

Ekiz, E. and El-Tawil, S. 2006. Inhibiting Steel Brace Buckling Using CFRP Wraps, *Proceedings of the 8th U.S. National Conference on Earthquake Engineering*: 2496, San Francisco, California, USA.

Ekiz, E. and El-Tawil, S. 2008. Restraining Steel Brace Buckling Using a Carbon Fiber-Reinforced Polymer Composite System: Experiments and Computational Simulation. *Journal of Composites for Construction (ASCE)* 12(5): 562-569.

El Damatty, A.A., and Abushagur, M. 2003. Testing and Modeling of Shear and Peel Behavior for Bonded Steel/FRP Connections. *Journal of Thin Walled Structures* 41(11): 987-1003.

El Damatty, A.A., Abushagur, M., and Youssef, M.A. 2005. Rehabilitation of composite steel bridges using GFRP plates. *Applied Composite Materials.* 12: 309-325.

El-Tawil, S. and Ekiz, E. 2009. Inhibiting Steel Brace Buckling Using Carbon Fiber-Reinforced Polymers: Large-Scale Tests. *Journal of Structural Engineering (ASCE)* 135(5): 530-538.

Engelhardt, M.D., Husain, A.S. (1992). "Cyclic tests on large scale steel moment connections," Phil M. Ferguson Structural Engineering Laboratory Report (PMFSEL), Report No. 92-2, Austin, TX.

Eurocode-8. 2003. *Design of Structures for Earthquake Resistance – Part-1: General Rules, Seismic Actions, and Rules for Buildings*. Brussels, Belgium: *European Committee for Standardization* (CEN).

FEMA (Federal Emergency Management Agency) 2000a. *Recommended Seismic Design Criteria for New Steel Moment-Frame Buildings*. Washington, D.C: Federal Emergency Management Agency (FEMA) Publication No. - FEMA-350.

FEMA (Federal Emergency Management Agency) 2000b. *Recommended Seismic Evaluation and Upgrade Criteria for Existing Welded Steel Moment-Frame Buildings.* Washington, D.C: Federal Emergency Management Agency (FEMA) Publication No. FEMA-351.

Guven, C.A. 2009. *Experimental Study on Improving Local Buckling Behavior of Steel Plates Strengthened with Glass Fiber Reinforced Polymers*. Master of Science Thesis, Izmir Institute of Technology (IYTE), April.

Harries, K.A. Peck, A.J. and Abraham, E.J. 2009. Enhancing Stability of Structural Steel Sections Using FRP. *Thin Walled Structures* 47: 1092-1101.

Jones, S.C. and Civjan, S.A. 2003. Application of Fiber Reinforced Polymer Overlays to Extend Steel Fatigue Life. *Journal of Composites for Construction (ASCE)* 7(4): 331-338.

Labview. (2007). Version 8.0, National Instruments, Austin, TX, USA.

Lenwari, A., Thepchatri, T., and Albrecht, P. 2005. Flextural Response of Steel Beams Strengthened with Partial-Length CFRP Plates. *Journal of Composites for Construction* 9(4): 296-303

LRFD. 1998. *Load and Resistance Factor (LRFD) Manual, 2nd Edition*, *American Institute of Steel Construction* (AISC), Chicago, IL.

Nakashima, M., Suita, K., Morisako, K. 1998. Tests of Welded Beam-Column Subassemblies I: Global Behavior. *Journal of Structural Engineering*, ASCE 124(11):1236-1244.

Okazaki, T., Liu, D., Nakashima, M., and Engelhardt, M.D. 2006. Stability Requirements for Beams in Seismic Steel Moment Frames. *Journal of Structural Engineering*, ASCE 132(9):1331-1342.

Ozdemir, T. 2009. *Seismic Behavior of Steel I-Beams Modified by a Welded Haunch and Reinforced with Glass Fiber Reinforced Polymers*. Master of Science Thesis, Izmir Institute of Technology (IYTE), October.

Nozaka, K., Shield, C.K., and Hajjar, J.F. 2005. Effective Bond Length of Carbon-Fiber-Reinforced Polymer Strips Bonded to Fatigued Steel Bridge I-Girders. *Journal of Bridge Engineering (ASCE)* 10(2): 195-205.

Peck, A.J. 2007. *Investigation of FRP stabilization of plastic buckling behavior of slender steel sections*. Master of Science Thesis. University of Pittsburgh, December, Pittsburgh, PA, USA.

Photiou, N.K., Hollaway, L.C., and Chryssanthopoulos, M.K. 2006. Strengthening of an Artificial Degraded Steel Beam Utilizing a Carbon/Glass Composite System. *Construction and Building Materials* 20:11-21.

Rizkalla, S. and Dawood, M. 2006. High Modulus Carbon Fiber Materials for Retrofit Steel Structures and Bridges. *Proceedings of Developments in Composites: Advanced, Infrastructural, Natural and Nano-composites*, Sydney, Ausralia.

SAC. (1996). *Experimental investigation of beam-column subassemblages. Technical Report* SAC-96-01, Parts 1 and 2, Sacramento, CA:SAC Joint Venture.

Sayed-Ahmet, E.Y. 2006. Numerical Investigation into Strengthening Steel I-Section Beams Using CFRP Strips. *Proceedings of the 2006 Structures Congress*, St. Louis, Missouri, USA

Schnerch, D. Stanford,K. Sumner,E. Rizkalla,S. 2005. *Bond Behavior of CFRP strenghtened Steel Bridges and Structures*. Proceedings of International Symposium on Bond Behaviour of FRP in Structures (BBFS 2005)

Schnerch, D., Dawood, M., Rizkalla, S., and Sumner, E. 2006. Proposed Design Guidelines for Strengthening of Steel Bridges with FRP Materials. *Construction and Building Materials* 21:1001-1010.

Sen, R., Liby, L. and Mullins, G. 2001. Strengthening Steel Bridge Sections Using CFRP Laminates. *Composites Part B.* 32:309-322.

Shaat, A. and Fam, A. 2007. Finite Element Analysis of Slender HSS columns strengthened with High Modulus Composites. *Steel and Composite Structures* 7(1): 19-34.

Shaat, A. and Fam, A. 2009. Slender Steel Columns Strengthened Using High-Modulus CFRP Plates for Buckling Control. *Journal of Composites for Construction (ASCE)* 13(1): 2-12.

Tavakkolizadeh, M. and Saadatmanesh, H. 2003a. Strengthening of Steel-Concrete Composite Girders Using Corbon Fiber Reinforced Polymers Sheets. *Journal of Structural Engineering (ASCE)* 129(1): 30-40.

Tavakkolizadeh, M. and Saadatmanesh, H. 2003b. Repair of Damaged Steel-Concrete Composite Girders Using Carbon Fiber-Reinforced Polymer Sheets. *Journal of Composites for Construction (ASCE)* 7(4): 311-322.

Tavakkolizadeh, M. and Saadatmanesh, H. 2003c. Fatigue Strength of Steel Girders Strengthened with Carbon Fiber Reinforced Polymer Patch. *Journal of Structural Engineering (ASCE)* 129(2): 186-196.

Uang, C.M., Yu, Q.S., Noel, S., and Gross, J. 2000. Cyclic Testing of Steel Moment Connections Rehabilitated with RBS or Welded Haunch. *Journal of Structural Engineering* 126(1):57-68.

UBC (Uniform Building Code) 1994. *International Conference of Building Officials*. Whittier, CA.

Yu, Q.S., Uang, C.M., and Gross, J. 2000. Seismic Rehabilitation Design of Steel Moment Connection with Welded Haunch. *Journal of Structural Engineering (ASCE)* 126(1): 69-78.

Yu, Q.S. 1999. *Experimental and Analytical Studies of Conventional and Modified Steel Moment Connections under Simulating Seismic Loading*. Ph.D. Thesis. University of California, San Diego, CA, USA.

APPENDIX A

BEAM-COLUMN CONNECTION DESIGN

A.1. Column Panel Zone Design

Column panel zone on the beam-column connection is designed to be elastic, so it is predicted that the same column can be used for several tests. HD 400x187 (present at laboratory) used as a column is chosen for the beam-column connection. It is designed for HE 500 AA and HE 400 AA beams, which will generate highest moment. In first sight, it can be seen that HE 500 AA is more critical but yielding and fracture points of the HE 400 AA are 25% and 15% higher than HE 500 AA values, respectively. Moreover, depths of the beams are not same.

● **Properties of the Sections**

Column HD400×187:

Depth (d_b) = 368 mm

Thickness of Web (t_w) = 15 mm

Thickness of Flange (t_f) = 24 mm

Width of Flange (b_f) = 391 mm

Area = 23760 mm^2

Moment of Inertia (I_x) = 601.8 × 10^6 mm^4

Plastic Moment (Z_x) = 3642000 mm^3

Section Modulus (S_x) = 3271000 mm^3

Distance between fillets on the web (T) = 290 mm

Beam HE 400 AA:

Depth (d) = 378 mm

Thickness of Web (t_w) = 9.5 mm

Thickness of Flange (t_f) = 13 mm

Width of Flange (b_f) = 300 mm

Area = 11770 mm^2

Moment of Inertia (I_x) = 312.52 × 10^6 mm^4

Section Modulus (S_x) = 1620900 mm^3

Flange Plastic Modulus (Z_f) = 1574000 mm^3

Web Plastic Modulus (Z_w) = 309000 mm^3

Plastic Modulus (Z_x) = 1883000 mm^3

Flange Yield Stress (F_{yf}) = 413.1 MPa

Web Yield Stress (F_{yw}) = 436.1 MPa

Flange Rupture Stress (F_{uf}) = 487.1 MPa

Web Rupture Stress (F_{uw}) = 520.7 MPa

Plastic Moment (M_p) = $F_{yf} \times Z_x + F_{yw} \times Z_w$ = 785 kN-m

Distance between Fillets on the Web (T) = 390 mm

Moment of Inertia (I_y) = 58.61 × 10^6 mm^4

Radius of gyration (r_x) = 163 mm

Radius of gyration (r_y) = 70.6 mm

Beam HE 500 AA:

Depth (d) = 472 mm

Thickness of Web (t_w) = 10.5 mm

Thickness of Flange (t_f) = 14 mm

Width of Flange (b_f) = 300 mm

Area = 13690 mm^2

Moment of Inertia (I_x) = 546.43× 10^6 mm^4

Section Modulus (S_x) = 2315000 mm^3

Flange Plastic Modulus (Z_f) = 2080000 mm^3

Web Plastic Modulus (Z_w) = 562000 mm^3

Plastic Modulus (Z_x) = 2642000 mm^3

Flange Yield Stress (F_{yf}) = 329.4 MPa

Web Yield Stress (F_{yw}) = 379.5 MPa

Flange Rupture Stress (F_{uf}) = 427.9 MPa

Web Yield Stress (F_{uw}) = 465.9 MPa

Plastic Moment (M_p) = $F_{yf} \times Z_x + F_{yw} \times Z_w$ = 898.4 kN-m

Distance between Fillets on the Web (T) = 390 mm

Moment of Inertia (I_y) = 63.14 × 10^6 mm^4

Radius of gyration (r_x) = 199.8 mm

Radius of gyration (r_y) = 67.9 mm

● **The highest Moment Predicted on Plastic Hinge Region (M_{max})**

(AISC 2005a Equation 2.4.3-1):

$$M_{pr} = C_{pr} R_y F_y Z_e, \tag{A.1}$$

where:

M_{pr} = maximum moment expected in the plastic hinge region (N-mm)

R_y = ratio of the expected yield stress to the specified minimum yield stress (ANSI/AISC 341-05 (AISC 2005b) Table I-6-1)

Z_e = effective plastic modulus of the section at the location of the plastic hinge (mm^3)

C_{pr} = factor to account for peak connection strength, including strain hardening, local restraint, other connection conditions:

$$C_{pr} = \frac{F_y + F_u}{2F_y} \le 1.2 \,(AISC\,2005a\ Equation\ 2.4.3-2), \tag{A.2}$$

F_y = specified minimum yield stress of steel (MPa)

F_u = specified minimum tensile strength of steel (MPa)

C_{pr} is determined as mentioned in the AISC (2005a) because yield stress and rupture stress of the sections get from the standard tests. C_{pr} was taken 1.1 according to Equation A.2 while R_y taken 1.0 due to the consideration of standard coupon test results in calculations. However, the maximum expected moment calculated using Equation A.1 will still be exceeded for beams with GFRP strips. Accord and Earls (2006) have shown that the addition of GFRP strips can increase the plastic moment by 25%. Therefore, the maximum moment (M_{max}) expected in the plastic hinge region

of HE400AA with GFRP was taken as 1.3 times the value calculated by Equation A.1:

$$M_{\max} = 1.30 M_{pr}, \tag{A.3}$$

The maximum moment expected in the experiments have been calculated for the HE400AA and HE500AA beams by using Equation A.3 as follows:

M_{max} = 1.3 × 1.1 × 1.0 × 785 = 1123 kN-m (HE400AA)
M_{max} = 1.3 × 1.1 × 1.0 × 869.2 = 1243 kN-m (HE500AA)

● Length of the test Beams (L)

Capacities of Actuator (P) = 445 kN
Moment on the Fixed End of the Cantilever Beam = PL = M_{max}
$L_{HE400AA}$ = 2.52 m required
$L_{HE500AA}$ = 2.88 m required

Chosen Beam Length for Safety:
$L_{HE400AA}$ = 2.9 m
$L_{HE500AA}$ = 3.94 m

● Lateral Support for Beam (L_b)

Laterally unbraced length (L_b) is calculated by using AISC 341-05 (AISC 2005b)

$$L_b = 0.086 r_y \frac{E}{Fy} \text{ (AISC 2005b, page 6.1-35),} \tag{A.4}$$

$$L_{b(HE400AA)} = 0.086x70.6x\frac{200000}{413.1} = 2.94m$$

$$L_{b(HE500AA)} = 0.086x67.9x\frac{200000}{329.4} = 3.55m$$

Beams must be supported laterally in order not to be subjected to lateral buckling during the experiment.

● **Expected Shear Force on the Column Surface (V_u)**

Beam-column connection and shear forces on the column are shown on Figure A.1. Shear Forces occurred six points through the column are reduced to two points in order to simplify (Top and bottom of the column at a distance from $L_c/4$).

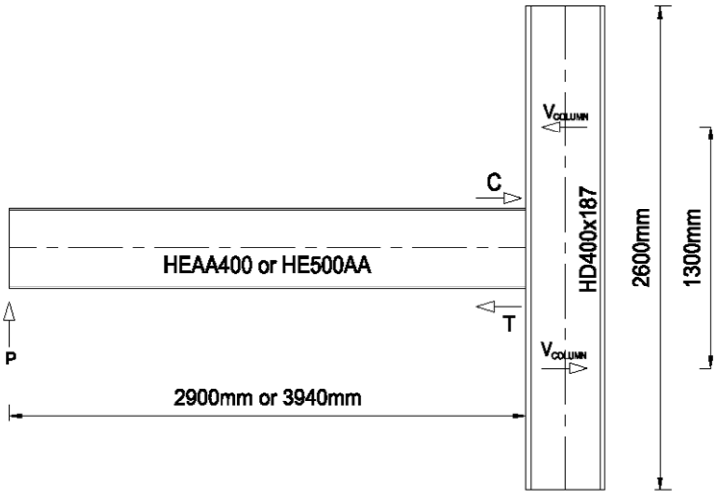

Figure A.1. Beam-Column Connection

For the HE 400 AA Beam;

$$T{=}C{=}\frac{M_{\max}}{\left(d-t_f\right)} = \frac{1123000^{N-mm}}{\left(378^{mm}-13^{mm}\right)} = 3076\ kN,$$

$$V_c = \frac{2}{2600^{mm}} 1123000^{N-mm} = 864\ kN,$$

$$V_{req} = C - V_c = 3076^{kN} - 864^{kN} = 2212\ kN,$$

For the HE 500 AA Beam;

$$T=C=\frac{M_{maks}}{\left(d-t_f\right)}=\frac{1283000}{\left(472-14\right)}=2801\,kN\,,$$

$$V_c=\frac{2}{2600}1283000=986\;kN\,,$$

$$V_{req}=C-V_c=2801^{kN}-986^{kN}=1815\;kN\,,$$

Shear force of HE 400 AA is higher. As a result:

V_u = 2212 kN is adopted

● **Determination of Shear Strength of Doubler Plates on the Panel Zone and Determination of Strength of the Continuity Plates ($V_{u\,dp}$, $R_{u\,st}$)**

Determination of the ultimate shear force on the doubler plate ($V_{u\,dp}$) is given below:

$$V_{u\,dp}=V_u-\phi R_{v\,cw},\ AISC\ (2003b)\ Equation\ 4.2\text{-}2$$

$\emptyset R_{v\,cw}$ = Column web design shear strength (kN) (A.5)

V_u = Factored panel-zone shear force (kN)

$$\phi R_n=0.9x0.6F_y d_c t_w,\ AISC\ (2005c)\ Equation\ J10\text{-}9 \qquad (A.6)$$

$$\phi R_n=0.9x0.6x235^{N/mm^2}368^{mm}15^{mm}=700\;kN$$

$$V_{u\,dp}=2212^{kN}-700^{kN}=1512\;kN$$

Determination of the ultimate force on the continuity plates ($R_{u\,st}$) is given below:

$$R_{u\,st}=P_{uf}-\phi R_{n\,\min},\ AISC\ (2003b)\ Equation\ 4.2\text{-}1 \qquad (A.7)$$

P_{uf} = Factored beam flange force, tensile or compressive (kN) = 2801 kN

$\varnothing R_{n\ min}$ = The lesser of design strengths in flange bending and web yielding at locations of tensile flange forces, or te lesser of the design strengths in local web yielding, web crippling, and compression buckling (if applicable) at locations of compressive flange forces (kN)

Determination of $\varnothing R_{n\ min}$:

a) Local Flange Buckling

$$\phi R_n = 0.9x6.25t_f{}^2 F_{yf}\text{, AISC (2005c) Equation J10-1} \quad \text{(A.8)}$$

$$\phi R_n = 0.9x6.25\left(24^{mm}\right)^2 235^{N/mm^2} = 760\ kN$$

b) Local Web Yielding

$$\phi R_n = 1.0x\left(2.5k + N\right)t_w F_{yw}\text{, AISC (2005c) Equation J10-3} \quad \text{(A.9)}$$

k = Distance from outer face of the flange to the web toe of the fillet = 39 mm

N = Length of bearing (not less than k for end beam reactions) = 13 mm

$$\phi R_n = 1.0x\left(2.5x39^{mm} + 13^{mm}\right)15^{mm}235^{N/mm^2} = 390\ kN$$

c) Web Crippling

$$\phi R_n = 0.75x0.4xt_w{}^2\left[1 + 3\left(\frac{N}{d}\right)\left(\frac{t_w}{t_f}\right)^{1,5}\right]\sqrt{\frac{EF_{yw}t_f}{t_f}} \quad \text{(A.10)}$$

, AISC (2005c) Equation J10-5a

$$\phi R_n = 0.75x0.4x(15^{mm})^2\left[1+3\left(\frac{13^{mm}}{368^{mm}}\right)\left(\frac{15^{mm}}{24^{mm}}\right)^{1,5}\right]$$
$$x\sqrt{\frac{200000^{N/mm^2}\,235^{N/mm^2}\,24^{mm}}{15^{mm}}} = 616kN$$

d) Web Compression Buckling

$$\phi R_n = 0.90\frac{24t_w{}^3\sqrt{EF_{yw}}}{h}0.5, \text{ AISC (2005c) Equation J10-8} \qquad \text{(A.11)}$$

h = Clear distance between flanges less the fillet or corner radius for rolled shapes

$$\phi R_n = 0.90\frac{(24^{mm})^3\sqrt{200000^{N/mm^2}\,235^{N/mm^2}}}{290^{mm}}0.5 = 860\ kN$$

When the values above are compared, it is clear that $\emptyset R_{n\,min}$ is 390kN.

$$R_{u\ st} = P_{uf} - \phi R_{n\,\min} = 3076^{kN} - 390^{kN} = 2686\ kN$$

● Design of Web Doubler Plates on the Column Panel Zone

$V_{u\,dp}$ = 1512 kN

Thickness of web doubler plates:

$$t_p \geq \frac{V_{u\,dp}}{0.9x0.6F_y d_c}, \text{ AISC (2003b) Equation 4.4-1} \qquad \text{(A.12)}$$

$V_{u\ dp}$ = That portion of the total panel-zone shear that is carried by the web doubler plate (kN)

d_c = column depth (mm)

$$t_p \geq \frac{V_{u\,dp}}{0.9x0.6F_y d_c} \geq \frac{1512000^{N}}{0.9x0.6x235^{N/mm^2}\,x368^{mm}} = 32.4\ mm$$

The minimum thickness to prevent shear buckling of the web doubler plate:

$$t_{p\min} \geq \frac{h^{in}\sqrt{F_y^{\,ksi}}}{418},\ AISC\ (2003b)\ Equation\ 4.4\text{-}5 \qquad (A.13)$$

$$t_{p\min} \geq \frac{368^{mm}\,x1^{in}/25.4^{mm}\sqrt{36^{ksi}}}{418} = 0.21\ in = 5.3\ mm$$

In high-seismic applications the minimum thickness to prevent shear buckling of the web doubler plate:

$$t_{\min} \geq \frac{d_m - t_s + d_c - 2t_f}{90} \geq \frac{h^{in}\sqrt{F_y^{\,ksi}}}{418},\ AISC\ (2003b)\ Equation\ 4.4\text{-}6 \qquad (A.13)$$

d_m = Moment arm between concentrated flange forces (mm)

t_s = transverse stiffener thickness (mm)

$$t_{\min} \geq \frac{458^{mm} - 25^{mm} + 368 - 224^{mm}}{90} = 8.36\ mm \geq \frac{h^{in}\sqrt{F_y^{\,ksi}}}{418}$$

When the doubler plate extends past the transverse stiffener, it must be of sufficient thickness to resist the shear force that is transmitted to the column panel-zone through the transverse stiffener:

$$t_{p\min} \geq \frac{(R_{u\,st})_1 + (R_{u\,st})_2}{0.9x0.6xF_y(l - 2\ x\ clip)} \geq \frac{(R_{u\,st})_1 + (R_{u\,st})_2}{0.9x0.6xF_y d_c\ x\ 2} \qquad (A.15)$$

$$,\ AISC(2003b)\ Equation\ 4.4\text{-}3$$

$R_{u\,st}$ = Required strength of the transverse stiffeners

Clip = Transverse stiffener corner clip dimension

$$t_{p\min} \geq \frac{2686000^{N} + 0}{90x0.6x235^{N/mm2}(320^{mm} - 2\ x\ 20^{mm})x4} = 18.9\ mm$$

$$\geq \frac{2686000^{N} + 0}{0.9x0.6x235^{N/mm2}368^{mm}\ x\ 2} = 28.8\,mm$$

Considering the abovementioned values, t_{pmin} should be $28.8^{mm}/2$ =14.4 mm. Because in the laboratory 25 mm plates are present, t_p was choosen 25 mm.

The height and width of the continuity plates can be determined considering the dimensions of the column panel zone. The width of the stiffener shall be determined as the sum of the column T length from LRFD Manual (1998) Table 9.1 and 2 times of encroachment length.

w = The width of stiffener = T + 2×encroachment length = 290^{mm} + 2×6^{mm} = 300 mm

The length of doubler plate shall be determined as the sum of beam depth and 5 times of distance from the beam flange to the fillet.

L = The length of doubler plate = 472^{mm} + 5×39^{mm} = 665 mm

2 doubler plates shall be $25^{mm} \times 300^{mm} \times 665^{mm}$.

<u>Stiffener – Column Flange Weld:</u>

Weld in this region shall be TC-U4a weld described LRFD (1999) (see Figure A.2).

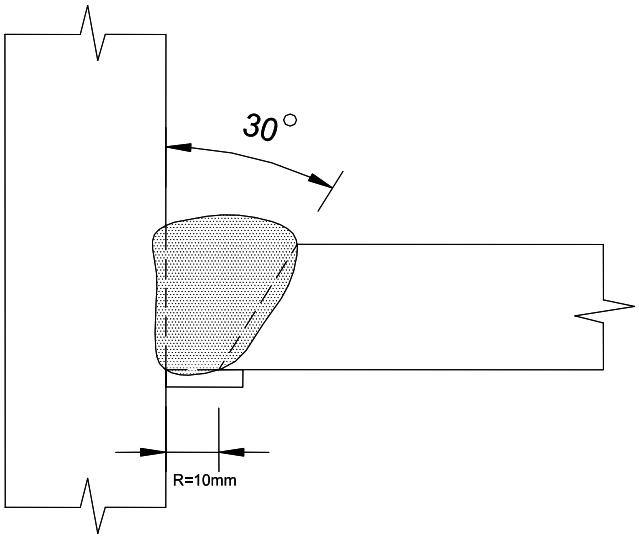

Figure A.2. TC-U4a Groove Weld (LRFD, 1999)

Top and Bottom Edge of Doubler Plate – Column Web Weld:

The dimensions and welds of doubler plates are on the Figure A.3.

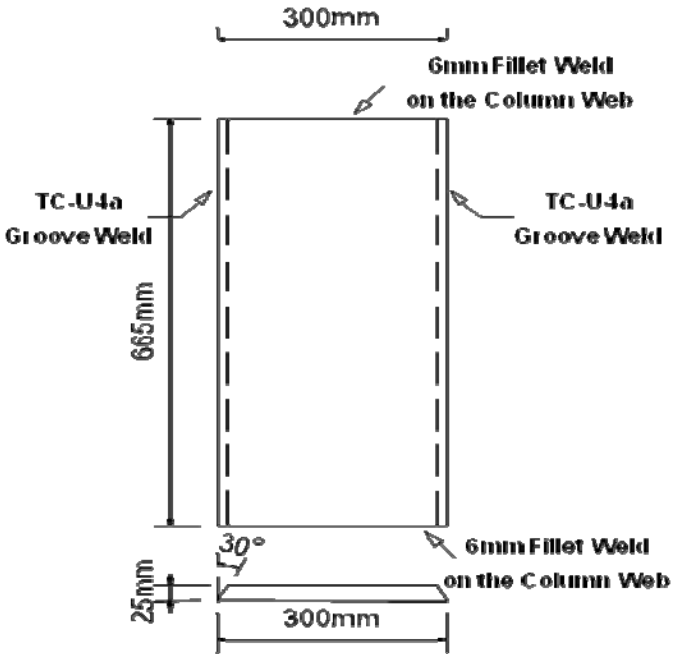

Figure A.3. Dimensions of Doubler Plate and Welds

In this zone, the thinnest fillet weld will be used. The thinnest fillet weld is specified in AISC (2005c) Table J2.4. According to this, the thinnest filet weld is 6mm for a 15 mm column web thickness and 25 mm plate thickness.

● **Design of Continuity Plates on the Column Panel Zone and Weld Design of Continuity Plates**

$$R_{u\ sl} = 2686\ kN\ ,$$

The smallest area of the continuity plates:

The smallest area of the continuity plates shall be determined by using AISC (2003b) Equation 4.3-1:

$$A_{sl\,\min} = \frac{R_{u\ st}}{\phi F_{y\,st}}\ ,\ AISC\ (2003b)\ Equation\ 4.3\text{-}1 \qquad (A.16)$$

$$A_{sl\,\min} = \frac{2686000^{N}}{0.9x235^{N/mm2}} = 13522\ mm^{2}$$

The width of the continuity plates:

Continuity plates shall be through the flange in high-seismic applications (AISC, 2003b). (see Figure A.4)

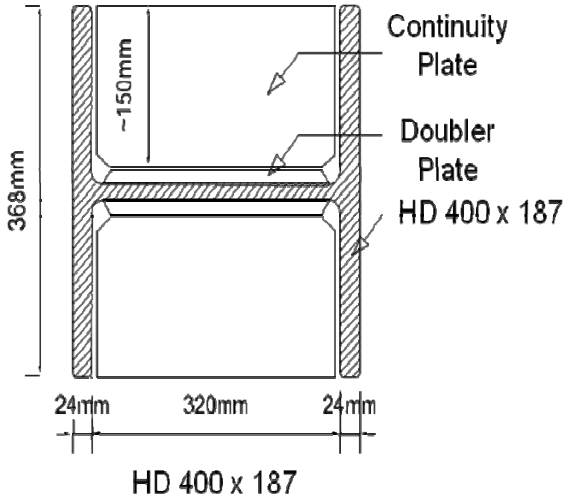

Figure A.4. Continuity and Doubler Plates

Continuity plates with width=150 mm and $20^{mm} \times 20^{mm}$ grooves:

AISC (2003b) Equation 4.3-3 shall be used for thickness determination.

$$t_{s\min} = \frac{t_b}{2} \geq \frac{b_s^{in}\sqrt{F_{yst}^{ksi}}}{95} = \frac{14}{2} \geq \frac{150^{mm}\, x(1^{in}/25.4^{mm})\sqrt{36^{ksi}}}{95} = 0.4\ in = 9.5\ mm \quad \text{(A.17)}$$

Determination the thickness also considering the length:

l = the length of continuity plates = 368^{mm}-24^{mm}×2 = 320 mm

$$k_{sl} \geq \frac{(R_{u\,sl})_1}{0.9x0.6xF_{a\,sl}(l-2xnotch)x2},\ AISC\ (2003b)\ Equation\ 4.3\text{-}5 \quad \text{(A.18)}$$

$$k_{sl} \geq \frac{2686000^{N}}{0.9x0.6x235^{N/mm^2}\, x(320^{mm} - 2x20^{mm})x2} = 37.8\ mm$$

Thickness that will used = 40 mm. This thickness also compensates area requirements.

Details of continuity plates are on Figure A.5. Because HE 400 AA and HE 500 AA have different depths, continuity plates are located adapted with those.

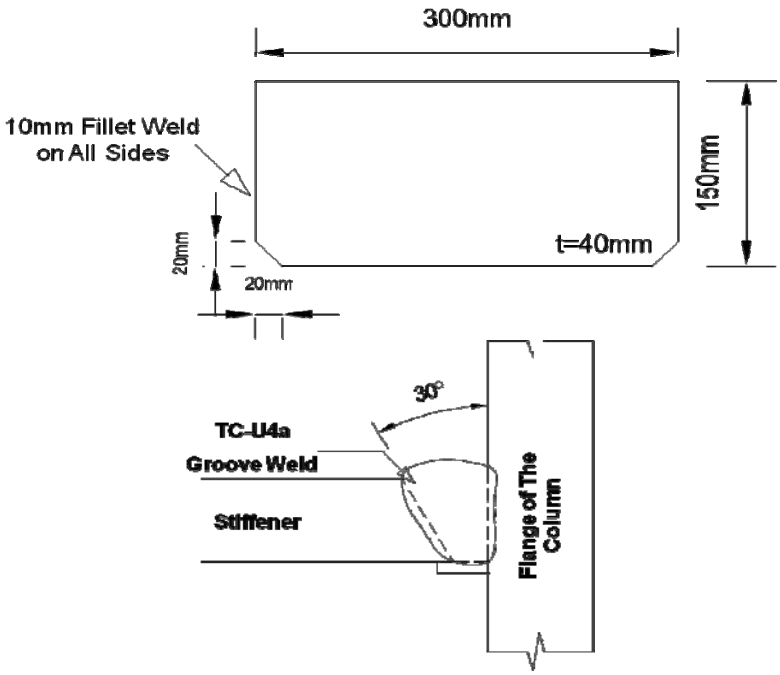

Figure A.5. Details of Continuity Plates

A.2 Weld Design Beam Flange–Column Flange

Beam-column connections shall be groove weld and typical TC-U4a weld was chosen. Weld access hole and weld details are in association with AISC (2005b) and they are shown in Figure A.6.

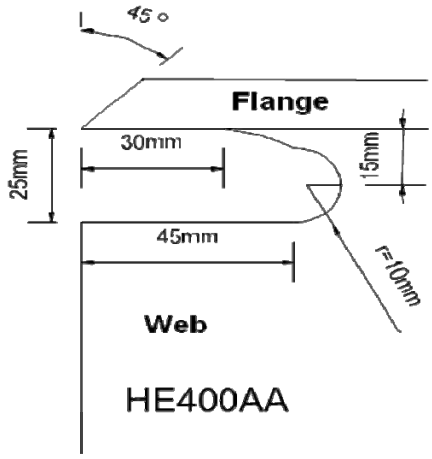

Figure A.6. Weld Access Hole Detail

A.3 Beam Web-Column Flange Shear Connection Design

The shear zone for HE400AA section will be designed without considering the welded haunch and GFRP strengthening. This project simulates structures, which built previously. It is assumed that any strengthening options are not considered during construction phase. Also, it is expected that, the first design would not be slender after strengthening. In the sections with welded haunch, the most of the shear forces will be supported by welded haunch. The connection view and dimensions are specified in Figure A.7.

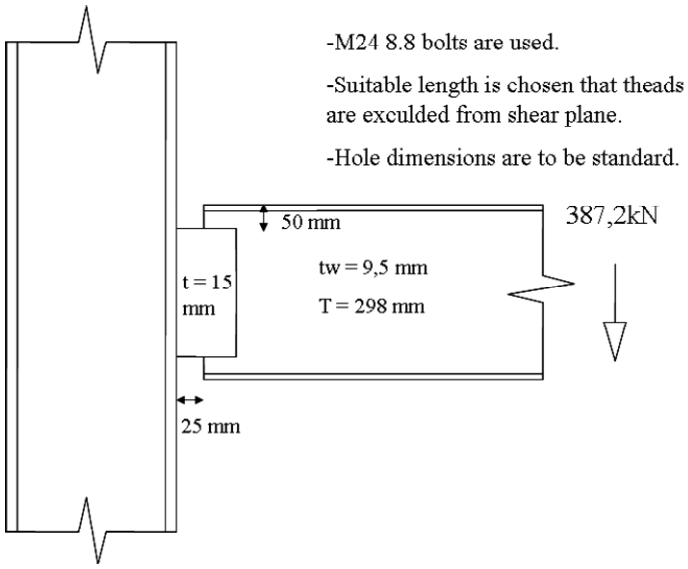

Figure A.7. Beam-Column Shear Connection

Maximum force at actuator will be for M_{pr}

$P_{maks} = M_{pr} / L = 1123000^{N-m} / 2.9^{m} = 387.2$ kN

.Bolt distances , L_c ve L_e:

See Figure A.8

-Edge distance for the full capacity, L_e:

$L_e = 2.5d + c/2$ (AISC, 2005c)

d = bolt diameter

c = space at bolt hole

$L_e = 2.5 \times 24^{mm} + 2^{mm}/2 = 61$ mm

- The smallest distance between bolts: L_c distance = $2.66d = 2.66 \times 24^{mm} = 64$ mm (AISC, 2005c).

Bearing Strength:

- For edge bolts:

L_c distance = $42-(24+2)/2=29^{mm}$

$$\phi R_n = \phi x 1.2 x L_c x t x F_u \leq 2.4 x d x t x F_u \text{, AISC (2005c) Equation (J3-6)} \quad \text{(A.19)}$$

$$\phi R_n = \phi x 1.2 x 29^{mm} x 9.5^{mm} x 520^{N/mm^2} \leq 2.4 x 24^{mm} x 9.5^{mm} x 520^{N/mm^2}$$

$$\phi R_n = 128.9^{KN} \leq 284^{KN}$$

- For center bolts:

L_c distance = $68-(24+2) = 42^{mm}$

$$\phi R_n = \phi x 1.2 x L_c x t x F_u \leq 2.4 x d x t x F_u \text{, AISC (2005c) Equation (J3-6a)} \quad \text{(A.20)}$$

$$\phi R_n = \phi x 1.2 x 42^{mm} x 9.5^{mm} x 520^{N/mm^2} \leq 2.4 x 24^{mm} x 9.5^{mm} x 520^{N/mm^2}$$

$$\phi R_n = 186.7^{KN} \leq 284^{KN}$$

-Total bearing strength = $\sum \phi R_n = 2x128.9^{kN} + 2x186.7^{kN} = 631.2^{kN} >$ 387.2 kN

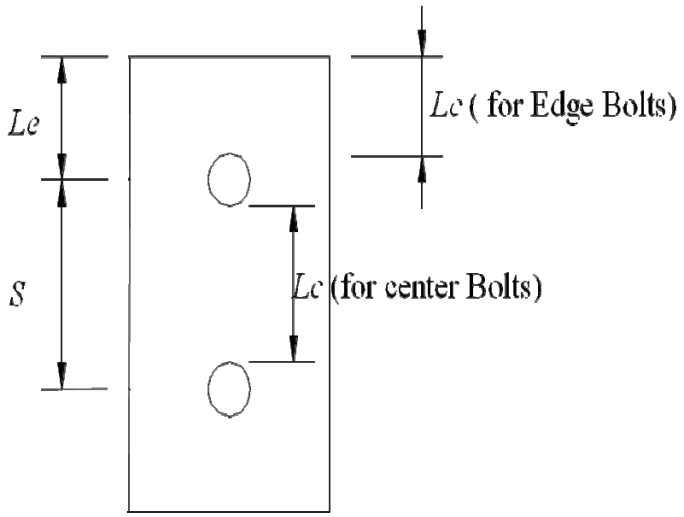

Figure A.8. Bolt Distances

Block Shear Strength (Plate) :

- Net area subject to shear, A_{nv}:

$A_{nv} = (248^{mm} - 3.5\times26^{mm})\times9.5^{mm}=1491.5^{mm2}$ (AISC, 2005c)

- Gross area subject to shear, A_{gv}:

$A_{gv} = 248^{mm}\times9.5^{mm} = 2356^{mm2}$ (AISC, 2005c)

-Net area subject to tension, A_{nt}:

$A_{nt} = (45^{mm} - 0.5\times26^{mm})\times9.5^{mm}=304^{mm2}$ (AISC, 2005c)

U_{bs}=1.0 (AISC, 2005c)

$$R_n = 0.6xF_u xA_{nv} + U_{bs}xF_u xA_{nt} \le 0.6xF_y xA_{gv} + U_{bs}xF_u xA_{nt} \quad \text{(A.21)}$$

, AISC (2005c) Denklem (J4-5)

$$R_n = 0.6x520^{N/mm2}x1491.5^{mm2} + 1x520^{N/mm2}x304^{mm2}$$
$$\le 0.6x350^{N/mm2}x2356^{mm2} + 1x520^{N/mm2}x304$$

$$R_n = 623.4^{kN} \le 652.8^{kN}$$

$$\phi R_n = 0.75x623.4^{kN} = 467.6^{kN} \ge 387.2^{kN}$$

Shear fracture for beam (Type II, Figure A.9) :

- Net area subject to shear, A_{nv} (AISC, 2005c)

$$\phi R_n = \phi x 0.6 x F_y x A_{nv}\text{ , AISC (2005c) Equation (J4-4)} \quad \text{(A.22)}$$

$$\phi R_n = 0.75 x 0.6 x ((206^{mm} + 42^{mm} x 2) - 4 x 26^{mm}) x 9.5^{mm} x 520^{N/mm2}$$

$$\phi R_n = 413.5^{kN} \geq 387.2^{kN}$$

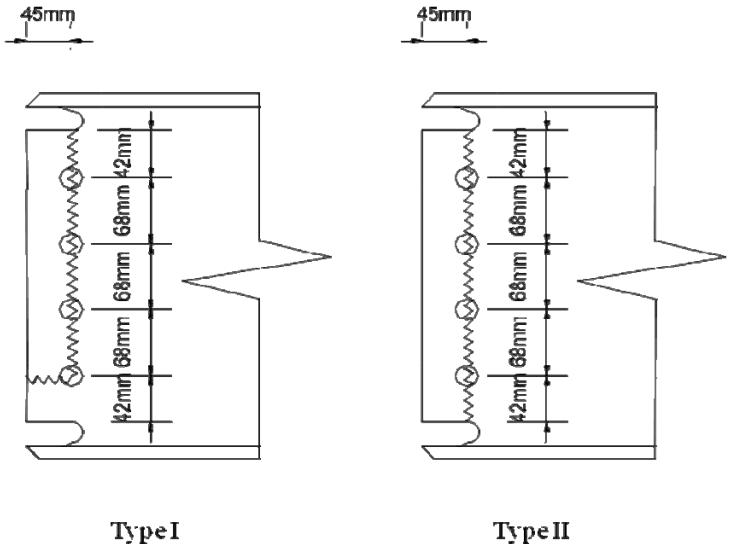

Figure A.9. Beam Web Shear Fracture Surfaces

Bolt shear design :

-Threads are excluded, A_b:

$$\phi R_n = \phi x F_n x A_b\text{ , AISC (2005c) Equation (J3-1)} \quad \text{(A.23)}$$

$$\phi R_n = 0.75 x \pi x (12^{mm})^2 x 0.4 x 785^{N/mm2}$$

$$\phi R_n = 106^{kN}$$

$$V_u = 387.2^{kN}$$

Total Bolts = $325^{kN} / 106^{kN} = 3.65 \sim 4$ Bolts (see Figure A.9 Type II)

Weld design of plate to column flange :

$$\phi R_n = \phi x F_w x A_w \text{ , AISC (2005c) Equation (J2-3)} \quad \text{(A.24)}$$

$$\frac{387200^{N}}{axL} = 0.707x0.75x0.6x600^{N/mm2}$$

a = weld size

L = weld length

$$L = 290^{mm} - 20^{mm}\, x2 = 250^{mm}$$

$$a = \frac{387200^{N}}{0.707x0.75x0.6x600x250^{mm}} = 8.11^{mm}$$

10^{mm} fillet weld shall be used on both sides.

APPENDIX B

WELDED HAUNCH DESIGN

B.1 HE400AA Welded Haunch Design

The design of the welded moment connections is based on the American Institute of Steel Construction (ANSI/AISC 358-05) Seismic Provisions (2005a), AISC Design Guide Series 12 Modification of Existing Welded Steel Moment Frame Connections for Seismic Resistance (AISC 2003a), FEMA 2000a, FEMA 2000b, Yu et al. (2000).

Step-by-step design calculation of HE400AA beam with triangular haunch at the bottom side is presented as follows:

● **Properties of the HE400AA Beam**

Depth (d) = 378 mm
Distance between fillets on the web (h) = 298 mm
Width of Flange (b_f) = 300 mm
Thickness of Flange (t_f) = 13 mm
Thickness of Web (t_w) = 9.5 mm
Distance from Outer Place of the Flange to Web Toe of Fillet (k) = 390 mm
Thickness of Beam Flange Delivering the Concentrated Force (N) = 13 mm
Area = 11770 mm^2
Moment of Inertia (I_x) = 312.52 × 10^6 mm^4
Section Modulus (S_x) = 1654000 mm^3
Plastic Modulus (Z_b) = 1824000 mm^3
Yield Stress (F_y) = 345 MPa
Elastic Modulus (E) = 200000 MPa
Beam Length (L) = 2900 mm

● **Step 1: Determination of a, θ and b values**

Design of the haunch is started with the suggestions of the length of the haunch, a, and the angle of the haunch, θ, as follows (AISC 2003a; Yu, et al. 2000):

$$a \approx (0.5 - 0.6)d\,, \tag{B.1}$$

$$\theta \approx 30^0 \pm 5^0\,, \tag{B.2}$$

$a \approx (0.5 - 0.6)d$: Choose a = 220 mm

$\theta \approx 30^0 \pm 5^0$: Choose $\theta = 35^0$

The b value that is the vertical component o the haunch length may be checked as follows (AISC 2003a; Yu, et al. 2000):

$$b = a\ tan\theta, \tag{B.3}$$

$b = a\ tan\theta$: Choose b = 155 mm

● **Step 2: Calculation of maximum moment (M_{pr}) expected in the plastic hinge region of beam:**

The expected plastic moment, containing the strain hardening and other factors, is calculated as follows:

$$M_{pr} = 1.2F_yZ_b, \tag{B.4}$$

where:

M_{pr} = maximum moment expected in the plastic hinge region (N-mm)

$$M_{pr} = 1.2F_yZ_b = 1.2x345x1824000 = 755136000\ N\text{-}mm$$

● **Step 3: Calculation of shear force, V_{pr}, in the plastic hinge region of beam:**

(Consider a uniform gravity load, w = 1 N/mm)

After the expected plastic moment, M_{pr}, is calculated, the corresponding beam shear, V_{pr}, at the plastic hinge region is determined as follows:

$$L' = L - 2a = 2900 - 2x220 = 2460\,mm$$

$$V_{pr} = \frac{M_{pr}}{(L'/2)} + \frac{wL'}{2} = \frac{755136000}{(2460/2)} + \frac{1x2460}{2} = 615162\,N$$

● **Step 4: Calculation of required minimum β value:**

(Consider strength of weld metal, F_{EXX} = 600 MPa)

In order to limit the top flange groove weld stress to an allowable stress value, F_w, the minimum value of β can be calculated as follows (AISC 2003a; Yu, et al. 2000):

$$\beta_{\min} = \frac{(M_{pr} + V_{pr}a)/S_x - F_w}{\frac{V_{pr}a}{S_x} + \frac{V_{pr}}{I_b \tan\theta}\left(\frac{d^2}{4} - \frac{I_b}{A_b}\right)}, \tag{B.5}$$

$F_w = 0.8F_{EXX} = 0.8x600 = 480\,MPa$

$$\beta_{\min} = \frac{(755136000 + 615162x220)/1654000 - 480}{\frac{615162x220}{1654000} + \frac{615162}{31.25x10^7\ x\tan 35^0}\left(\frac{378^2}{4} - \frac{31.25x10^7}{11770}\right)} = 0.54$$

● **Step 5: Sizing of haunch flange:**

For the design requirement, the haunch is sized as follows (AISC 2003a; Yu, et al. 2000):

$$A_{hf} = \frac{P_{hf}}{\phi F_{y,hf}} = \frac{\beta V_{pr}}{\phi F_{y,hf} \sin\theta}, \tag{B.6}$$

$$A_{hf} = \frac{P_{hf}}{\phi F_{y,hf}} = \frac{\beta V_{pr}}{\phi F_{y,hf} \sin\theta} = \frac{0.54x615162}{0.9x345x\sin 35} = 1865\,mm^2$$

For satisfying the stability requirement, the haunch flange area of 7500 mm^2 is selected. The corresponding cross-section dimensions of haunch are 25x300 mm (= t_{hf} x b_{hf}) are selected

Checking of the compact section requirement as follows (AISC 2003a; Yu, et al. 2000):

$$\frac{b_{hf}}{2t_{hf}} = \frac{300}{2x25} = 6 \le \frac{137}{\sqrt{345}} = 7.38 \quad OK$$

Selected dimensions of haunch are suitable for compactness requirements

● **Step 6: Evaluation of β value for stiffness requirement:**

For stiffness requirement, the axial stiffness of the haunch flange should satisfy that the actual β value is not less than the minimum β value. In order to compute the actual β value for the haunch flange stiffness requirement, the minimum vertical component of the reaction, $\beta_{min}V_{pr}$, is computed by considering the deformation compatibility between beam and haunch. The resulting β value is defined as follows (AISC 2003a; Yu, et al. 2000):

$$\beta = \left(\frac{b}{a}\right)\left(\frac{3L'd + 3ad + 3bL' + 4ab}{3d^2 + 6bd + 4b^2 + \frac{12I_b}{A_b} + \frac{12I_b}{A_{hf}\cos^3\theta}}\right) > \beta_{\min}, \qquad \text{(B.7)}$$

$$\beta = \left(\frac{155}{220}\right)\left(\frac{3x2460x378 + 3x220x378 + 3x155x2460 + 4x220x155}{3x378^2 + 6x155x378 + 4x155^2 + \frac{12x31.25x10^7}{11770} + \frac{12x31.25x10^7}{7500x\cos^3 35}}\right)$$

$$\beta = 1.45 > \beta_{\min} = 0.54 \quad OK$$

β is larger than the β_{min}. This means that the haunch flange with selected geometry would provide an adequate stiffness requirement. In other words the allowable stress, F_w, is an upper limit for the tensile stress in the flange groove weld at the column face.

After the actual β value is checked for the haunch flange stiffness requirement, the tensile stress in the top flange groove weld is computed and checked for the allowable stress, F_w, as follows:

$$f_{wt} = \frac{M_{pr} + V_{pr}(1-\beta)a}{I_b}\left(\frac{d}{2}\right) - \frac{\beta V_{pr} / \tan\theta}{I_b}\left(\frac{d^2}{4} - \frac{I_b}{A_b}\right) < F_w = 0.8F_{EXX}\,, \qquad \text{(B.8)}$$

$$f_{wt} = \frac{755136000 + 615162x(1-1.45)x220}{31.25x10^7}\left(\frac{378}{2}\right)$$
$$-\frac{1.45x615162/\tan 35}{31.25x10^7}\left(\frac{378^2}{4} - \frac{31.25x10^7}{11770}\right) = 382.5\ MPa < F_w = 0.8x600 = 480\ MPa$$

The haunch flange axial stress is checked as follows:

$$\frac{\beta V_{pr}}{A_{hf}\sin\theta} \le \phi F_{y,hf}\,, \qquad \text{(B.9)}$$

$$\frac{1.45x615162}{7500x\sin 35} = 207\ MPa \le \phi F_{y,hf} = 0.9x345 = 310.5\ MPa \quad OK$$

The tensile stress in the top flange groove weld and the axial stress in the haunch flange would satisfy the strength requirements.

Under the situation that the beam is subjected to positive bending, the maximum tensile stress in the bottom flange groove weld is checked for the allowable stress, F_w, as follows:

$$f_{wb} = \frac{V_{pr}(L'/2+a)}{I_b}\left(\frac{d}{2}\right) - \frac{\beta V_{pr} a}{I_b}\left(\frac{d}{2}\right) - \frac{(\beta V_{pr}/\tan\theta)(d/2)}{I_b}\left(\frac{d}{2}\right) -$$

$$\frac{\beta V_{pr}/\tan\theta}{A_b} = \frac{V_{pr}L'/2 + V_{pr}(1-\beta)a}{I_b}\left(\frac{d}{2}\right) - \frac{(\beta V_{pr}/\tan\theta)}{I_b}\left(\frac{d^2}{4} + \frac{I_b}{A_b}\right), \qquad \text{(B.10)}$$

$$< F_w = 0.8F_{EXX}$$

$$f_{wb} = \frac{615162x(2460/2) + 615162x(1-1.45)x220}{31.25x10^7}\left(\frac{378}{2}\right)$$

$$-\frac{(1.45x615162/\tan 35)}{31.25x10^7}\left(\frac{378^2}{4} + \frac{31.25x10^7}{11770}\right) = 167\ MPa < F_w = 0.8x600 = 480\ MPa$$

● **Step 7: Checking of shear capacity of both haunch web and beam web:**

For the haunch web width-thickness ratio, compactness requirements can be calculated as follows:

$$\frac{a\sin\theta}{t_{hw}} \le \frac{683}{\sqrt{F_{y,hw}}}, \qquad \text{(B.11)}$$

$$\frac{220x\sin 35}{25} = 5 \le \frac{683}{\sqrt{345}} = 36.8 \quad OK$$

Thickness of the haunch web, t_{hw}(=12mm) is within the accebtable limit for the compactness requirement.

Shear stress, τ_{hw}, in the haunch web is computed as follows:

$$\tau_{hw} = \frac{aV_{pr}}{2(1+\upsilon)I_b}\left(\frac{L'}{2} - \frac{\beta}{\tan\theta}\left(\frac{d}{2}\right) + \frac{(1-\beta)a}{3}\right) < \phi_v(0.6F_{y,hw}), \qquad \text{(B.12)}$$

$$\tau_{hw} = \frac{220x615162}{2x(1+0.3)x31.25x10^7}\left(\frac{2460}{2} - \frac{1.45}{\tan 35}\left(\frac{378}{2}\right) + \frac{(1-1.45)x220}{3}\right)$$

$$\tau_{hw} = 134.2\ MPa < 0.9x(0.6x345) = 186.3\ MPa \quad OK$$

The shear in the web, V_{bw}, is calculated as follows:

$$V_{bw} = (1-\beta)V_{pr}, \tag{B.13}$$

$$V_{bw} = (1-\beta)V_{pr} = (1-1.45)x615162 = -276823\,N < V_{pr} = 615162\,N$$

The value of V_{bw} is negative. It means that the direction of the beam shear in the haunch region is reversed. In other words, β is larger than 1. The result of Equation A.13 shows that the critical beam shear force is significantly larger than the shear force in the beam web. Results clearly show that the designed haunch is very suitable for the purpose that the welded haunch reduces the beam shear at the column face.

● Step 8: Designing of the beam web stiffeners depended on the actual β value:

The situation of without beam web stiffeners for the design strength, R_n, is checked for the local web yielding using the following equation as follows:

The design strength R_n, is less than the concentrated force of βV_{pr}. Therefore, a pair of beam web stiffeners consisted of 140x25 mm plates (A572 Gr. 50 steel) are provided at the end of the haunch.

The width-thickness ratio of the stiffeners is checked for a compactness section as follows:

$$\frac{b_s}{t_s} \le \frac{250}{\sqrt{F_{y,s}}}, \tag{B.14}$$

$$\frac{b_s}{t_s} = \frac{140}{25} = 5.6 \le \frac{250}{\sqrt{F_{y,s}}} = \frac{250}{\sqrt{345}} = 13.4 \quad OK$$

For strength requirement of an axially compressed member, including two stiffeners together with a strip of the beam web having a width of 12 t_w with an effective length of 0.75h.

$$A_{eff} = 2x140x25 + 12x9.5^2 = 6683mm^2$$

$$I_{eff} = 140x\frac{(25x2+9.5)^3}{12} = 2457524\ mm^4$$

$$r = \sqrt{\frac{I_{eff}}{A_{eff}}} = \sqrt{\frac{2457524}{6683}} = 19.2\ mm$$

$$\lambda_c = \frac{kL}{r\pi}\sqrt{\frac{F_y}{E}} = \frac{0.75x298}{19.2x3.14}\sqrt{\frac{345}{200000}} = 0.15 < 1.5$$

$$\phi_c F_{cr} = \phi_c(0.678^{\lambda_c^2})F_y = 0.85x(0.678^{0.15^2})x345 = 291\ MPa$$

$$\phi_c P_n = \phi_c F_{cr} A_{eff} > \beta V_{pr}$$

$$\phi_c P_n = 0.85x291x6683 = 1653040\ N > 891985\ N \quad OK$$

The stiffeners are ensured to the strength requirement.